

# PCCP

Accepted Manuscript



This is an *Accepted Manuscript*, which has been through the Royal Society of Chemistry peer review process and has been accepted for publication.

*Accepted Manuscripts* are published online shortly after acceptance, before technical editing, formatting and proof reading. Using this free service, authors can make their results available to the community, in citable form, before we publish the edited article. We will replace this *Accepted Manuscript* with the edited and formatted *Advance Article* as soon as it is available.

You can find more information about *Accepted Manuscripts* in the [Information for Authors](#).

Please note that technical editing may introduce minor changes to the text and/or graphics, which may alter content. The journal's standard [Terms & Conditions](#) and the [Ethical guidelines](#) still apply. In no event shall the Royal Society of Chemistry be held responsible for any errors or omissions in this *Accepted Manuscript* or any consequences arising from the use of any information it contains.

Insights into the physical chemistry of materials from advances in HAADF-STEM

Karl Sohlberg<sup>1</sup>, Timothy J. Pennycook<sup>2,3</sup>, Wu Zhou<sup>4</sup> and Stephen J. Pennycook<sup>5</sup>

1) Department of Chemistry, Drexel University, Philadelphia, PA 19104

2) Timothy J. Pennycook, SuperSTEM Laboratory, Daresbury, UK

3) Department of Materials, University of Oxford, Parks Road, Oxford OX1 3PH, UK

4) Materials Science & Technology Division, Oak Ridge National Laboratory, Oak Ridge, TN 3783

5) Department of Materials Science and Engineering, University of Tennessee, Knoxville, Tennessee 37996

**Abstract:**

The observation that, "New tools lead to new science"[Weiss, P.S., *ACS Nano.*, **6**(3), 1877-1879 (2012)], is perhaps nowhere more evident than in scanning transmission electron microscopy (STEM). Advances in STEM have endowed this technique with several powerful and complimentary capabilities. For example, the application of high-angle annular dark-field imaging has made possible real-space imaging at sub-angstrom resolution with Z-contrast ( $Z =$  atomic number). Further advances have wrought: simultaneous real-space imaging and elemental identification by using electron energy loss spectroscopy (EELS); 3-dimensional (3D) mapping by depth sectioning; monitoring of surface diffusion by time-sequencing of images; reduced electron energy imaging for probing graphenes; etc. In this paper we review how these advances, often coupled with first-principles theory, have led to interesting and important new insights into the physical chemistry of materials. We then review in detail a few specific applications that highlight some of these STEM capabilities.

## Introduction:

### HAADF-STEM basics:

The work to be discussed herein is based on high resolution scanning transmission electron microscopy, principally centered on the technique of high angle annular dark field imaging, termed HAADF-STEM. The general concepts of the technique are captured schematically in Figure 1. Electrons from a high brightness source are accelerated through a potential difference of many kV and focused to a small spot by a set of electron lenses (the most important one being the objective or probe-forming lens). A cold field emission source uses an accelerating potential to extract electrons from a metal tip. This produces a very intense beam current, without the spread in kinetic energies produced by a thermal electron source. High electron beam current is necessary to achieve good signal/noise. Near-monochromaticity of the electron kinetic energies is needed to achieve high image and spectral resolution.

Figure 1 near here.

The objective lens focuses the electron beam to a small spot on a thin slab of material to be imaged. In recent years there has been great progress in the design of the illumination system. Correction of the principal aberrations in electron lensing has been achieved through the application of multipole lenses, *vide infra*. This has led not only to substantial improvements in spatial resolution, but also to improved signal to noise (S/N) ratio because the same beam current may be focused onto a spot of smaller cross-sectional area, resulting in higher current density.

Once focusing is achieved, the spot is scanned over the sample in a raster pattern. The transmitted electrons are then collected with an annular detector and the collected intensity (electron current) is recorded as a function of position, resulting in an image incoherent in real-space. The annular detector collects the electrons that are deflected by large angles. Such wide-angle scattering results from the interaction of the electrons with the atomic nuclei<sup>1</sup>. Wide-angle scattering is therefore predominantly Rutherford scattering, in which the differential cross section is proportional to the square of the nuclear charge. This is a straightforward result from introductory classical scattering theory.

For two particles charged ( $Q_1$ ) and ( $Q_2$ ), the radial dependence of the Coulomb interaction potential (in atomic units) is given by,

$$V(r) = Q_1 Q_2 / r. \quad (\text{X})$$

It can be shown, (See for example Ref.<sup>2</sup>) that for this interaction potential, the intensity of scattering by a given deflection angle ( $\chi$ ) is,

$$I(\chi) = \left( \frac{Q_1 Q_2}{4E} \right)^2 \text{cosec}^4 \left( \frac{\chi}{2} \right), \quad (\text{X})$$

where ( $E$ ) is the collision energy. In STEM, the colliding partners are electrons ( $Q_1 = -1$ ) and atomic nuclei ( $Q_2 = Z$ ). Since the latter are much heavier than the former, the collision center of mass (com) is effectively coincident with the atomic nucleus and deflection angle seen in the laboratory frame is effectively the same as deflection angle in the collision frame of reference. For this reason, in theory, the intensity of scattering is proportional to the square of the nuclear charge. The conclusion holds up under a more rigorous quantum mechanical scattering analysis.

In actual practice, ( $I(\chi) \propto Z^{(1.6..1.7)}$ ) depending on the actual inner angle of the detector because the incident electrons don't see the full nuclear charge owing to screening by the atomic electrons. There are other sources of contrast as well. An example is shown in Fig. 2, where the contrast from thermal vibrations can be seen to be stronger in the image taken with a medium-angle detector than in the image taken in the high-angle detector. Additionally, strain

fields can give quite strong contrast. For this reason, although HAADF-STEM is often colloquially referred to as "Z-contrast STEM" or "Z-STEM," the latter term is imprecise since contrast is not exclusively due to Z. This is especially true at lower angles, so ADF-STEM, which is nominally the same technique as HAADF-STEM but doesn't explicitly call for a high angle detector, can have more contributions to contrast from non-Z sources.

This review focuses on applications in materials science, particularly emphasizing crystalline materials where atomic resolution is important. Applications to non-crystalline materials are also possible, but because the atoms are not arranged in regular columns they cannot be individually resolved. Useful applications have been made in polymer materials<sup>3,4</sup> and even in biological samples<sup>5</sup>. Beam damage becomes a serious issue in biological samples, however, and it is not feasible to examine live cells. Z-contrast imaging has better resolution than even super-resolved fluorescence microscopy,<sup>6,7</sup> but the latter technique uses light to excite the cell which can be tolerated much better by living systems.

Figure 2 near here.

#### The evolution of resolution:

An ideal application for HAADF-STEM is the analysis of samples that consist of heavy atoms such as lanthanides, actinides or 2<sup>nd</sup> & 3<sup>rd</sup> row transition metal elements dispersed on a lighter support (such as alumina, silica or titania). It's therefore not surprising that the first hints of imaging single atoms were for the heaviest naturally occurring element, uranium, on a thin carbon substrate<sup>8</sup>. This was accomplished with an instrument using a 30 kV accelerating voltage producing a beam diameter of about 2.5 Å<sup>9</sup>. Improved instrumentation with a theoretical image resolution of 2.2 Å, achieved in part by increasing the accelerating voltage to 100 kV, led to more convincing images of U/carbon<sup>10</sup>.

The dispersal of heavy atoms on a light support is a generic prescription for constructing a heterogeneous catalyst (*vide infra*) and HAADF-STEM has seen extensive use for characterizing heterogeneous catalyst samples. In turn, heterogeneous catalyst samples have been used extensively to demonstrate HAADF-STEM capabilities. Early demonstrations of HAADF-STEM on catalyst samples include work by Howie et al.<sup>11</sup> and by Pennycook et al.<sup>12</sup> wherein silica-supported Rh catalyst particles of dimension 1-2 nm were imaged with Z-STEM and EELS (discussed below). Supported clusters of Pt and Pd have also been frequent targets for HAADF-STEM<sup>13</sup>.

Further increase in the accelerating voltage improved the image resolution to 1.3Å<sup>14</sup>. This advance made it possible to provide direct evidence that ultra-dispersed transition metal (TM) catalysts can exist as isolated TM atoms on the catalytic support, as was demonstrated in an investigation by Nellist and Pennycook<sup>15</sup> that compared ultra-dispersed Rh/γ-alumina(100) to ultra-dispersed Pt/γ-alumina(110). Pt was seen to exist as isolated Pt atoms or in small clusters on the alumina surface, whereas Rh was found to form raft-like structures on the surface. Coupling the results of that investigation with first-principles theory then yielded significant new insight into the atomic-scale structure of these catalysts.

#### *Pt/alumina:*

The first atomic-resolution image of Pt/alumina<sup>15</sup> is reproduced in Fig. 3a together with a more recent and higher-resolution image<sup>16</sup> in Fig. 3b. The approximate directions of the lattice vectors, ascertained from the complementary phase-contrast image, are annotated. Striking in the image is the presence of small clusters of Pt atoms on the supporting alumina, most notably trimers. The structures aroused considerable curiosity because the Pt-Pt distances are not consistent with those in Pt metal or known Pt<sub>n</sub> clusters<sup>17,18</sup>. First-principles density-functional-theory calculations revealed that the anomalously long Pt-Pt distances arise from depletion of electron density from the Pt-Pt bonds by an -OH capping structure, the presence of which is energetically favored.

Figure 3 near here.

#### *Rh/alumina:*

Rh raft structures in the Rh/alumina catalytic system had been known since the late 1970s when Yates was able to confirm their existence through a combined experimental investigation using infrared spectroscopy to probe adsorbed CO and electron microscopy to image the structure<sup>19</sup>. The atomic-scale structure of these "rafts" did not become apparent, however, until a combination of atomic-resolution HAADF-STEM and first-principles theory was brought to bear on the matter. The first component was reported by Nellist and Pennycook<sup>15</sup> and is shown in Figure 4a. Note that the image reveals fringes of intensity that suggest rows of Rh atoms that are resolved in one direction, (being separated by about 2.8 Å) but unresolved in the orthogonal direction.

The origin of this structure was deduced through the application of first-principles density functional theory calculations<sup>20</sup>. Various attempts to construct clusters of Rh on an alumina surface in such a way as to produce a projected Rh spacing less than the 1.3 Å spatial resolution of the HAADF-STEM all failed. Such close Rh spacing was found to be energetically unstable and the features disintegrated upon structural optimization. One key to unraveling their structure was recognizing that the possibility that the Rh might be oxidized, or at least partially oxidized. The first such clue came from previous studies of Pt/alumina, which found that Pt<sub>3</sub> structures are stabilized by a capping -OH group<sup>16</sup>. The second clue came from the work of Campbell<sup>21</sup>, who showed that transition metal *oxides* can have enhanced stability as a thin film. Under some conditions a thin oxide film on a metal surface is more stable than the bulk oxide. Zhuo and Sohlberg noted that there is a sesquioxide of Rh for which the projected separation of Rh atoms is less than 1.3 Å along one axis but about 2.8 Å in the orthogonal direction, namely the high-pressure Rh<sub>2</sub>O<sub>3</sub>-II phase<sup>22</sup>. (See figure 5.) DFT calculations revealed that thin fragments of Rh<sub>2</sub>O<sub>3</sub>-II are stable when supported on  $\gamma$ -alumina (100). Figure 4b shows a close-up view of the HAADF-STEM image together with a simulated image (Figure 4c) based on the theoretically predicted Rh<sub>2</sub>O<sub>3</sub>-II/ $\gamma$ -alumina (100) structure<sup>23</sup>. The agreement is very good. That the high-pressure phase of Rh sesquioxide would prefer to grow on alumina is easily rationalized. Since alumina is also a sesquioxide, but Al atoms are smaller than Rh atoms, it is reasonable that the rhodia would need to be squeezed to achieve a lattice match to the alumina. This finding, and the finding that the raft structures are oxidized, is the kind of insight made possible by the combination of atomic-resolution HAADF-STEM and first-principles theory.

Figure 4 near here.

Figure 5 near here.

Some further improvement in spatial resolution came from recognition that, "incoherent transmission electron microscope imaging is extremely robust to the effects of chromatic aberration"<sup>24</sup>, and that by capitalizing on this robustness and employing under focusing it is possible to realize information transfer at sub-angstrom levels. This was demonstrated by partially separating Cd and Te columns in CdTe along the (112) Miller axis<sup>24</sup>. The next major advance in resolution, however, came from using multipole lensing to correct for the aberrations inherent in cylindrical lenses.

#### Aberration correction:

It has been over 60 years since the first proposals were made to overcome the primary lens aberrations of the electron microscope<sup>25,26</sup>. As early as the 1960s Crewe and others were experimenting with multipole lensing to correct for aberrations inherent in round lenses<sup>27,28</sup>. Further efforts were reported by Rose<sup>29</sup>, and Daghish and coworkers in the 1980s<sup>30-32</sup>. These

attempts confirmed proof-of-principle, but were of limited value in practical application. While some of these attempts were close to being practical, the ultimate limitation was that they were simply too difficult to adjust manually. There is a trade-off between having sufficiently many degrees of freedom to correct all the aberrations that show up (especially once rotational symmetry is broken) and having so many controls that the optimization process becomes too complex to be done by hand. In this situation an image looks “blurry” and there is no systematic procedure for sharpening it manually within a reasonable time frame. Computer control can bypass this difficulty by hiding the complexity and automating a lot of the tedious but complicated adjustments. The advent of this computer control therefore brought practical aberration correction into use. Simulations showed what was to come more than a decade ago<sup>33</sup> and the first successful application in STEM was reported by Batson<sup>34,35</sup>. Aberrations are classified by order (i.e. 1<sup>st</sup>-order, 2<sup>nd</sup>-order, 3<sup>rd</sup>-order...)<sup>36</sup>. The dramatic improvement in spatial resolution that aberration correction can provide is clearly manifest in Fig. 3. Figure 3a shows Pt<sub>3</sub>/alumina taken with the VG microscopes HB603U 300 kV STEM before aberration correction and Fig. 3b shows the same but with aberration correction through just 3<sup>rd</sup> order. In the latter image, not only do the Pt atoms show up as bright, well-resolved spots, but also there is the added benefit that fringes of contrast from the light alumina support are also visible.

The blossoming of nanoscience provided fertile ground for application of aberration corrected HAADF-STEM. In fact, one of the early uses was to probe semiconducting nanocrystals. The technique produced many lattice-resolved images of CdSe nanocrystals<sup>37</sup>. CdSe nanocrystals showcase the advantages of aberration corrected HAADF-STEM over conventional TEM because not only is high spatial resolution required to resolve the Cd and Se columns, but these elements differ in Z and the Z-contrast provides chemical information coincident with the spatial information. An excellent review of the role of aberration corrected HAADF-STEM in nanoscience has been presented by Varela et al<sup>38</sup>.

#### Aberration correction at lower electron kinetic energies

With the next generation of aberration correction, achieving correction up to 5<sup>th</sup> order, it has become possible to achieve atomic resolution at much lower accelerating voltages than the 300 keV accelerating potential that was first used to push spatial resolution in HAADF-STEM into the 1Å range. 5<sup>th</sup>-order correction makes it possible, for example, to obtain atomic-resolution images of BN and graphene at only 60 kV electron accelerating energy, which is below their damage threshold.

Using a Nion UltraSTEM, Krivanek et al. demonstrated the resolution and identification of B and N atoms 1.45Å apart in monolayer BN, and the location and identification of individual substitutional C and O atoms<sup>39</sup>. (See Figs. 6a & 6b.) In phase contrast imaging the contrast difference between B and N is extremely weak and the lattice polarity has only been distinguished by exit wave reconstruction methods<sup>40-42</sup>. Operating at only 60 kV, with an efficient medium angle annular detector, the image shown in Fig. 6a was obtained<sup>39</sup>. Even in the raw data, the individual B and N atoms are directly resolved and distinguished. Furthermore there are several sites where the intensity does not correspond to either B or N. After filtering, Fig. 6b, the image quality is improved, and the line traces show atoms with an intensity intermediate between that of B and N, presumably C, and others of higher intensity, possibly O. A histogram of intensities confirmed that the brighter atoms were O (Figure 6c).

Figure 6 near here.

#### EELS

One of the great advantages of STEM over alternative electron microscopy techniques is that it employs electron lensing *prior* to the specimen to be imaged<sup>43</sup>. Not only does this simplify

focusing the electrons, (since they are emitted essentially homogeneously from a well-defined source) but it also means that different detectors can be placed in different angular positions post-sample, giving simultaneous access to different types of information about the sample. While the high-angle annular detector collects scattered electrons that carry information about the nuclear charge ( $Z$ ), the low-angle transmitted electrons carry information about the atomic core electrons since the incident electrons can undergo inelastic scattering upon interaction with the core electrons. By filtering these low-angle transmitted electrons with an electron kinetic energy spectrometer, their energy loss upon traversing the sample can be determined. The inelastic interactions excite core-electron transitions whose energies are characteristic of the species present. This electron energy loss spectrometry (EELS) therefore allows for chemical identification of the nuclei present.

Figure 7 near here.

Figure 7 shows a schematic description of the origin of an EELS spectrum. The atoms present in the material possess electrons that can be assigned by their quantum numbers ( $n, l, m_l, s$ ). These quantum numbers may be combined into a term symbol of the form ( $nl^{l+s}$ ). By convention, these are grouped into *shells* (K, L, M, N...) by principal quantum number. Electrons from the probe beam may undergo *inelastic* scattering with the electrons in the atoms making up the material, losing kinetic energy as the electrons from the atoms within the material are ejected past the ionization threshold. If intensity is plotted versus energy loss, with increasing energy sharp onsets are seen where the energy loss exceeds the threshold for ionization from a given shell. The RHS of Fig. 7 shows a hypothetical ionization of an electron from the  $L_3$  shell and a corresponding schematic of the  $L_3$  edge in the EELS spectrum. This cartoon spectrum is zoomed in on the region of the  $L_3$  edge. Peaks at very small energy losses can appear due to excitation of plasmon resonances in the material. Fine structure can appear above the  $L_3$  edge (or other edge of interest) as electrons are excited into states buried in the continuum.

Electron energy loss spectroscopy capability extends beyond simple identification of the nuclei present in a sample. It can also be used to probe their chemical environment. For example, EELS was used to distinguish between different oxides of Sn. The oxygen K-edge energy is relatively insensitive to the chemical environment, but the Sn M-edge shifts by about 3.5 eV between the stannous ( $\text{SnO}$ ) and stannic ( $\text{SnO}_2$ ) forms<sup>44-46</sup>. Mapping each edge therefore reveals not only the presence of tin and oxygen, but also the oxidation state of the Sn.

EELS capability was demonstrated as early as 1944 by Hillier and Baker<sup>47</sup> and strongly advocated by Crewe<sup>43</sup> 22 years later. The spatial resolution in EELS is limited predominantly by two factors, the electron/atom impact cross section, (a physical limit) and the electron probe beam diameter, (instrument limitation)<sup>48</sup>. In practice, the latter limitation has been the dominant one, but decreases in the probe beam spot size eventually enabled EELS mapping of interface structures at the resolution of single atomic planes, as demonstrated for a  $\text{CoSiO}_2$ -Si interface by Browning et al. in 1993<sup>49</sup>. Figure 8, (from Ref.<sup>49</sup>) clearly shows a dramatic decrease in Co L-edge intensity between the cobalt silicide and silicon sides of a  $\text{CoSiO}_2$ -Si interface. Later *atomic column resolution* EELS was demonstrated in  $\text{SrTiO}_3$  by Allen et al.<sup>50</sup>

Figure 8 near here.

Atomic-resolution EELS has proved very powerful for probing metal oxide heterostructures and interfaces. For example, experimental studies of  $\text{Y}_2\text{O}_3$ - $\text{ZrO}_2$ / $\text{SrTiO}_3$  (YSZ/STO) heterostructures have pointed to much greater disorder in the oxygen sublattice in the  $\text{Y}_2\text{O}_3$ - $\text{ZrO}_2$  region. This effect was suggested by DFT studies<sup>51,52</sup> and directly imaged using HAADF-STEM together with atomic-resolution EELS<sup>53,46</sup>. Figure 9 shows a real-space HAADF-STEM image of the heterostructure together with EELS images taken at the Ti-L and O-K

spectral edges, along with a composite of the latter two. The image reveals direct evidence of the oxygen disorder in the  $\text{Y}_2\text{O}_3\text{-ZrO}_2$  region where the oxygen positions are not resolved due to the increased disorder.

Figure 9 near here.

The first spectroscopic analysis of a single atom was reported in 2004.<sup>54</sup> Today, atomic-resolution EELS can provide chemical identification of single-atom impurities. Figure 10a, (from Ref.<sup>55</sup>) shows a HAADF-STEM image of a  $\text{CaTiO}_3$  thin film. The highlighted columns were then probed with EELS, (Figure 10b) revealing the presence of a single La impurity.

Figure 10 near here.

One of the most stunning achievements to-date in the area is the chemical identification of point defects is shown in Figures 11(A-E). Therein is an example of imaging a Si-N point defect in graphene. Figure 11A shows a low-pass filtered ADF survey image. The whole area was used for spectrum imaging. Figure 11B shows the ADF signal collected simultaneously during spectrum imaging. Figure 11(C-E) show, respectively, the Si-L-, C-K-, and N-K- edge maps extracted from the STEM-EEL spectrum image. The positions of the substitutional Si and N atoms can be deduced from the locations of Si-L-edge and N-K-edge intensity, and are indicated by blue and green squares respectively. Images B-E are direct presentations of raw data. Note how the image collected at the carbon K-edge (Fig. 11D) is black where the impurity Si and N atoms are, verifying that they are substitutional. Follow-on experimental study<sup>56</sup> further shows that the substitutional Si atoms can take either three-fold or four-fold coordination in the graphene lattice (Fig. 11F), and this difference in atomic bonding can be directly distinguished from the experimental EELS fine structures (Fig. 11H). DFT calculations can well explain the observed fine structures, and reveal that the three-fold coordinated Si has  $\text{sp}^3$ -like bonding whereas the four-fold coordinated Si adopts  $\text{sp}^2\text{d}$ -like hybridization.

Figure 11 near here.

#### Depth profiling:

Yet another advantage of placing the electron optics prior to the specimen to be imaged is that it affords the opportunity to obtain information in the third spatial dimension (depth). Nominally, the image obtained by HAADF-STEM is a 2D projection of the full 3D of the specimen. The advent of aberration-correction in the objective lens, however, has opened the possibility of obtaining information in the third dimension. This is accomplished by varying the depth of the focus point and monitoring changes in contrast.

In the presence of aberration correcting lenses, the convergence angle of the electrons to the focus point is increased. As a consequence, the range of depths over which the probe beam is tightly focused is decreased. In general, the depth of field ( $\Delta z$ ) scales as,  $\Delta z \propto \frac{1}{\theta^2}$  where ( $\theta$ ) is the convergence angle<sup>57</sup>. Figure 12 shows in cartoon form how increasing the convergence angle results in a decrease in the total depth over which the beam is confined to a given cross sectional area. The tighter focusing of the probe in the axial direction offers the possibility of depth profiling. The intensity arising from scattering by a single atom is decreased when it is displaced from the focus point of the probe. By varying the depth of the focus point through a sample, the position of objects within the sample along the axial direction of the beam can be mapped.

Figure 12 near here.

The technique of depth-profiling was used with great success to demonstrate that La atoms in La-doped  $\gamma$ -alumina flakes segregate to the surface in work by Wang et al.<sup>58</sup>. A series of HAADF-STEM images for a sample of La/TiO<sub>2</sub> approximately 6nm thick is shown in Fig. 13. The focus depth was varied from 0, (the "top" of the specimen) to -10 nm. Note that although there is no lattice contrast from the substrate, indicating that the beam axis is not aligned with a crystallographic axis, there are two different focus depths at which the contrast is sharp. These correspond to dopant La atoms located on the top and bottom surfaces of the flake. This conclusion is given numerical support in the accompanying graph, which plots the mean image intensity (arbitrary units) versus focus depth. This technique works especially well for probing La in alumina because the high-Z La atoms show strong contrast relative to the low-Z of the alumina matrix. The depth resolution in this work was ca. 7 nm, using an instrument with aberration corrections in the objective lens through 3<sup>rd</sup> order. Higher-order aberration corrections will yield greater depth resolution.

Figure 13 near here.

A similar depth profiling technique was used to probe the 3D placement of Hf atoms within a HfO<sub>2</sub>/SiO<sub>2</sub>/Si alternative gate dielectric stack<sup>59</sup>. Borisevich et al. have carried out extensive analysis of the technique for (Pt, Au)/TiO<sub>2</sub> and (Pt, Ru)/ $\gamma$ -Al<sub>2</sub>O<sub>3</sub> catalyst samples<sup>57</sup>.

HAADF-STEM depth profiling is another area where nanoscience has provided fertile ground. In the study of nanostructures, one question that arises frequently is: What is the distribution of impurity atoms? Are they interior or exterior to the structure. An example of the use of HAADF-STEM depth profiling to answer such a question was reported by Oh et al., who imaged Au point defect configurations inside Si nanowires<sup>60,61</sup>. Figure 14 clearly shows the heavy Au atoms decorating the exterior of the Si nanostructure. Examination of the HAADF-STEM images at higher resolution then revealed Au atoms within the structure, and at several different sites. The stability of each structure was then verified with first-principles DFT calculations.

Figure 14 near here.

#### Time-sequencing with short scans:

Because STEM relies on collecting scattered electrons, which are discrete particles, the signal/noise ( $S/N$ ) ratio is governed by counting statistics. In general,  $S/N \propto n$  where  $n$  is the number of data points taken.  $S/N$  is therefore generally improved by lengthening the collecting time and long scans allow the identification of defects by differences in intensity. In recent years, however, improvements in instrumentation have yielded steady improvements in  $S/N$  so that good images may be collected with relatively shorter scans. This has provided a new opportunity because short scans allow for time resolution. Since quality images can now be collected in seconds, dynamical motions may be resolved on this same time scale. Figure 15 demonstrates this capability with a time sequence of images showing the diffusion of a Si atom along a graphene edge. The Z-contrast property of the HAADF-STEM affords easy identification of the single Si atom decorating the graphene edge. The time sequence shows its movement in time, while the graphene remains relatively unchanged over the same time scale. Such imaging is made possible by instrumentation that provides spatial resolution at the atomic level with short scans and with an electron kinetic energy below the graphene damage threshold, a combination of several significant advances in HAADF-STEM.

Figure 15 near here.

### **HAADF-STEM imaging of heterogeneous catalysts:**

#### Merits of HAADF-STEM for the study of heterogeneous catalyst materials

In heterogeneous catalysis, several key structural parameters, including particle size and shape, the precise atomic structure and chemical composition of surface layer/species, local composition and bonding, and charge transfer between surface layer/species and the support material, *etc.*, directly affect the catalytic performance. Since most catalytic reactions occurs on the surface of heterogeneous catalysts, there is a general desire to increase the exposed surface area of the active materials by reducing the particle size and/or by dispersing them onto a high surface area support material. This is especially true for noble metal catalysts, where increasing the metal dispersion to the ultimate limit that every metal atom could contribute to the catalytic performance can help to reduce the quantity of expensive metals used. Moreover, reducing the particle size can also sometimes change the catalytic properties completely, as in the case of Au catalysts<sup>62</sup>.

For advanced catalyst materials, the catalytically important feature size can range from single atoms to a few tens of nanometers. Therefore, in order to fully understand the relationship between the structure and catalytic performance of heterogeneous catalysts, characterization methods are needed that can probe structural and chemical information at the atomic level. Moreover, quite often, the structure of advanced catalysts is quite inhomogeneous, and the catalytically most active sites are not necessarily the dominant structures in the material. This predicament means that structural information about the small active sites may vanish among the averaged signals obtained from conventional optical spectroscopy and X-ray spectroscopy methods, with a sampling volume in the order of  $10^4 \text{ nm}^3$  or more. In contrast, as described in the introduction, aberration-corrected scanning transmission electron microscopy (STEM) can provide atomic-scale structural and chemical information that cannot be obtained otherwise, and is particularly suitable for the study of inhomogeneous nanocatalyst materials.

The merits of aberration-corrected HAADF-STEM lie in the following aspects: i) it is capable of directly imaging individual atoms or clusters, providing accurate measurement of size distribution and census of different species; ii) the image intensity, to a first approximation, is proportional to the square of the atomic number ( $Z$ ), providing  $Z$ -contrast; iii) the image intensity is also approximately proportional to the number of atoms imaged, provided the sample is thin, allowing feasible mass measurement of an individual particle or atomic column; iv) it can provide highly accurate atomic position measurement for the study of interactions between surface layer/species and the support material; and v) the image contrast mechanism for HAADF is very robust, making it the ideal signal for depth-sectioning and electron tomography.

The development of the aberration correction techniques has provided HAADF-STEM imaging with an unprecedented ability to provide  $Z$ -contrast information with sub-Å spatial resolution and single atom sensitivity<sup>63</sup>. For most aberration-corrected (S)TEM instruments, a 0.8-1.3Å spatial resolution can be routinely achieved for HAADF imaging with accelerating voltages of 200-60 kV, respectively, while high probe current can still be maintained in the small electron probe to provide high signal-to-noise ratio in the images. The ability to provide single atom detection with high spatial resolution and signal-to-noise ratios has made aberration corrected HAADF imaging more and more popular in the study of supported metal catalysts<sup>64-70</sup>, supported oxide catalysts<sup>71-73</sup>, bulk complex oxide catalysts<sup>74,75</sup>, and even highly electron-beam-sensitive Zeolite materials<sup>76,77</sup>. In fact, the quest to understand the catalyst structure and catalytic behavior is now considered one of the most important driving forces for the development of aberration-corrected electron microscopes<sup>78</sup>.

This section will show via case studies how HAADF-STEM imaging in an aberration-corrected STEM can be applied to understand some of the above-mentioned key structural parameters in heterogeneous catalysts. It should be mentioned, however, that most of the advantages of HAADF imaging come directly from its intrinsic image contrast mechanism. In

other words, HAADF imaging in a non-aberration-corrected STEM instrument can also deliver some aspects of the structural information that we will discuss below.

#### Direct imaging of structural features down to single atoms

It has been well documented that for structure-sensitive catalytic reactions, the specific catalytic activity depends on the size of the active particles or the domain size of the surface active species. Moreover, when the particles/clusters get smaller than 10 nm, their physical and chemical properties can be quite different from their bulk counterparts. Therefore, many catalyst characterization studies involve measurement of particle size distribution, trying to identify the optimum particle size for the best catalytic performance. Using conventional bright-field (BF) or high resolution TEM (HRTEM) imaging, particles larger than ~1nm can usually be satisfactorily imaged, which provides a feasible method for measurement of size distribution down to ~1nm scale. TEM images, however, do not usually provide single atom sensitivity. Supported surface species with only one atomic layer thickness, such as single atoms or monolayer clusters, typically generate little or no contrast in a single TEM BF or HRTEM image. Moreover, in conventional HRTEM images, the visibility of the small surface species depends sensitively on; i) the roughness of the surface of the support particle, ii) the precise imaging conditions and local sample geometry, and can be further complicated by the presence of surface amorphous layers either intrinsically associated with the support particles or from carbon contaminations. Therefore, size distribution measurements via TEM imaging tend to overlook the presence of small surface species, and, in some cases, do not represent the true population distribution of different active entities. Structure-activity relationship or “optimum particle size” deduced from such TEM characterization studies alone could therefore be questionable. This is especially true for many highly active supported metal catalysts where the active sites are believed to be single metal atoms on the support surface<sup>67,79,80</sup>.

As discussed above, direct imaging of single heavy atoms, in contrast, roots back to the early stage of the development of STEM-ADF imaging technique<sup>81</sup>. In 1970, Crewe *et al.* demonstrated the first direct imaging of single U atoms dispersed on thin carbon film via STEM-ADF imaging on a dedicated STEM without correcting the lens aberrations<sup>8</sup>. Since then, direct imaging of single surface heavy metal atoms have been reported in many supported metal catalyst systems, *e.g.* Au/FeOx, Au/C, Pt/Al<sub>2</sub>O<sub>3</sub>, *etc.* The correction of aberration for the probe forming lenses further increases the spatial resolution and sensitivity of ADF imaging technique, allowing lighter atoms to be captured under this imaging mode. With the latest instrumentation, as shown above, light atoms such as B, C, and N, in some ideal cases, can be clearly imaged one-by-one with STEM-ADF imaging<sup>39</sup>. The ability to image both heavy and light elements opens up new possibilities to study the surface structure of a wide range of heterogeneous supported catalysts. A common situation in many practical catalyst systems is the *co-existence* of different supported structures. The high resolving power and single atom sensitivity of HAADF imaging can ensure that all the fine structural information can be clearly captured. This can potentially help to deduce meaningful structure-activity relationship existing in these catalyst systems, especially for the identification of optimum domain/particle size for high catalytic performance.

Figure 16 near here.

One representative example is the study of supported Au catalysts. Long known as a chemically inert metal, Au was unexpectedly discovered by Haruta *et al.*<sup>82</sup> to be an excellent catalyst when it is made into nano-size particles. Since then, many investigations have been conducted to explore the catalytic performance of supported Au catalysts prepared using different methods and dispersed on various support materials for a wide range of chemical reactions. Most of the early studies employed TEM-BF imaging or HRTEM imaging to

characterize the Au particle size distribution (PSD) over a series of Au catalysts with different catalytic activity, and concluded by correlating the PSD to the catalytic performance that Au nanoparticles of specific size are much more active than others. Using aberration-corrected HAADF-STEM imaging, however, Herzing *et al.* found that there are numerous Au-containing species smaller than 1 nm in the supported Au/FeO<sub>x</sub> catalysts coexisting with larger Au nanoparticles<sup>70</sup>. The direct observation of these smaller surface Au species, as shown in Fig. 16, ranging from single Au atoms to sub-nm Au clusters, was surprising as they generate very little contrast in TEM images and have long been missed or neglected by other 'averaging' characterization techniques. Being able to visualize all the surface Au species down to single atoms, thus, enables the generation of more complete statistical picture of the different Au species present by analyzing a large number of images obtained from samples with different catalytic performance. By comparing the Au species in a highly active catalyst to those in a totally inactive catalyst, Herzing *et al.* found that the main difference is that bi-layer and monolayer sub-nm Au clusters are only present in the active sample. To further test if these Au clusters are responsible for the observed catalytic activity, they heat-treated the active sample to different temperatures, which substantially decreases the population of small Au surface species due to sintering. By correlating the population distribution of different Au species with the catalytic performance of a systematic set of Au/FeO<sub>x</sub> catalysts obtained from the heat-treatment experiment, Herzing *et al.* proposed that sub-nm bi-layer Au clusters are the most catalytically active species for low temperature CO oxidation<sup>70</sup>. The PSD can then be converted to metal dispersion and surface area for comparison with macroscopic values obtained from chemisorption measurements. The full PSD can also help to estimate the weight fraction of the proposed active structures and allow a more accurate calculation of turnover frequencies (TOFs) for the catalytic active site. As shown by Herzing *et al.*, the active sub-nm bi-layer Au clusters in their best Au/FeO<sub>x</sub> catalyst only constituted 0.6 atomic% of the total Au loading, and the "true" TOF value for these active clusters is calculated to be 3.5 s<sup>-1</sup> at the high flow rate conditions, close to the value of 3.7 s<sup>-1</sup> obtained from model Au/TiO<sub>2</sub> catalyst<sup>83</sup>, as compared to the apparent TOF of 0.027 s<sup>-1</sup> when all Au loading is counted. It should be noted that the catalytically active site is reaction specific, and depends on the support material and/or reaction conditions. In other words, the active structure in Au/TiO<sub>2</sub> might be different from that in Au/FeO<sub>x</sub>, and different reaction temperature/pressure might activate different structures. Nevertheless, aberration-corrected HAADF-STEM imaging provides the possibility to capture all the surface structures present in supported metal catalysts, and help to avoid potential oversight of small but significant active structures.

In the field of heterogeneous catalysis research there has recently been an increase in interest in the so-called single-atom catalysts<sup>79,80</sup>, where the noble metals are atomically dispersed on the support surface and serve as catalytically active sites. As mentioned before, when the feature size of interest approaches single atoms, conventional TEM imaging techniques are challenged to visualize such small species. In this respect, HAADF-STEM imaging is considered to be the most important characterization method that provides direct imaging of the single noble metal atoms on the surface and, when combined with complementary techniques such as X-ray absorption spectroscopy and/or optical spectroscopy, allows for a better structure-performance correlation. This has been demonstrated by several groups on different catalyst systems. Figure 17 shows a few examples where HAADF-STEM imaging is applied to study the dispersion and locations of single metal atoms on the support surface.

Figure 17 near here.

The examples discussed above all fall into the category of supported metal catalysts, where heavy metal nanostructures are dispersed onto light support materials, such as Al<sub>2</sub>O<sub>3</sub>, FeO<sub>x</sub>,

TiO<sub>x</sub> and carbon, etc. These systems are ideal for HAADF-STEM imaging since the heavy metal atoms can generate good Z-contrast against the lighter backgrounds from the support. The application of HAADF imaging to supported oxide-on-oxide catalysts is more challenging, however, because; i) it is difficult to image oxygen atoms on the oxide support surface; ii) the active oxide tends to form a highly dispersed overlayer on the support surface due to strong wetting interaction between oxides<sup>71</sup>; and iii) many oxide-on-oxide catalysts have a relatively small Z-difference between the two components, generating very low image contrast. In some cases where there is a large Z-difference between the two oxide components and the surface species are relatively stable under the electron beam, HAADF imaging can still help to identify the catalytically active structure.

Figure 18 near here.

One such example is the supported WO<sub>3</sub>/ZrO<sub>2</sub> catalyst, which is a promising solid acid catalyst for the isomerization of light alkanes (C<sub>4</sub> to C<sub>8</sub>) at low temperature. Extensive optical and X-ray spectroscopy studies since the 1980s have suggested that the catalytic activity depends on the precise nanostructure of the surface WO<sub>x</sub> species present, including mono-tungstate, poly-tungstate, WO<sub>x</sub> clusters, and 'bulk' WO<sub>3</sub> crystals<sup>72,73,84</sup>. Confirming the presence of these various surface species and identification of the precise nature of the most catalytically active site, however, was only recently realized when the HAADF technique was introduced into their study<sup>72,73</sup>. Using aberration corrected HAADF-STEM imaging, Zhou *et al.* obtained the first direct imaging of all the surface WO<sub>x</sub> entities on the ZrO<sub>2</sub> support, which allowed for the identification of the key catalytic active site and provided new insights into the structure-activity relationships for this catalyst system<sup>73</sup>. The key results are depicted in Figure 18. Similar to many catalysis studies, HAADF imaging was performed on a systematic set of supported WO<sub>3</sub>/ZrO<sub>2</sub> catalysts having different surface tungstate loadings and catalytic activities. As revealed by the HAADF images, atomically dispersed mono-tungstate (isolating WO<sub>x</sub> units) and poly-tungstate species, having single atomic-layer thickness, are dominant in the low activity samples (Figure 18A), while additional disordered surface oxide clusters ~0.8-1.0 nm in size (Figure 18B) were found to *co-exist* with the mono- and poly-tungstate species in the high activity samples. Even though oxygen atoms are not visible in the HAADF images, these different WO<sub>x</sub> species can be distinguished by analyzing the inter-atomic spacing and intensity directly from the images. The mono-tungstates contain isolated WO<sub>x</sub> units that are more than 3.5 Å apart. The poly-tungstate species typically has 2-6 W atoms linked by oxygen bridging bonds, with inter-atomic spacing between 2.5-3.5 Å, which falls within the theoretical range of the length of the W-O-W bridging bonds<sup>73</sup>. The surface oxide clusters, in contrast, usually contain 10-20 WO<sub>x</sub> units stacking in three dimensions, as can be observed by the higher image intensity and overlapping of the atomic positions. By analyzing the relative population of all of the surface tungstate species present in a systematic set of samples displaying a variety of catalytic activity, Zhou *et al.* were able to draw a direct correlation between the surface tungstate structure and the catalytic performance, *i.e.* the ~1 nm disordered surface oxide clusters represent the most catalytic active species in the supported WO<sub>3</sub>/ZrO<sub>2</sub> catalyst system<sup>73</sup>. Furthermore, the Z-contrast information containing in the HAADF images further helped to identify these active surface oxide clusters as Zr-WO<sub>x</sub> mixed-oxide clusters that contain both WO<sub>x</sub> and ZrO<sub>x</sub> species (Figure 18C)<sup>71,73</sup>. These HAADF results are in good agreement with combined catalysis and optical spectroscopy data<sup>84</sup>, and help to draw a consistent picture of the correlation among the sample preparation, structure, and catalytic performance. Importantly, Zhou *et al.* further showed that the performance of the catalyst can be increased by more than two orders of magnitude when a considerable amount of Zr-WO<sub>x</sub> mixed-oxide clusters are deliberately introduced into a poor catalyst via catalyst design<sup>73</sup>. This serves as an excellent example where fundamental structural information derived from HAADF study

can lead to a new direction for the rational design of advanced catalysts with enhanced performance.

In addition to the capability to image ultra-small surface species, HAADF-STEM also provides better visualization of large particles and thus more accurate size measurement, (in the range of 1-10 nm) as compared with conventional BF-TEM or HRTEM imaging. This benefit has been known for some time, and was recently discussed by Su *et al.*<sup>65</sup>. Basically, without aberration correction, HRTEM imaging suffers from a delocalization effect and, even after correction, often generates low contrast between the support materials and the supported particles. Both of these features limit the accuracy of the size measurements from HRTEM images. For HAADF imaging, when the electron probe is properly tuned and the image is well focused, high contrast with a sharp boundary between the supported particles and the support materials can be expected. This enables automatic size distribution measurements with high accuracy to be performed using image processing software by setting the proper image contrast threshold.

#### Chemical analysis and atom counting via HAADF-STEM imaging

Chemical analysis on a TEM/STEM is usually performed via X-ray energy dispersive spectroscopy (XEDS) or electron energy loss spectroscopy (EELS). Both techniques can be used to identify the elements present and their spatial distribution in two dimensional projections via spectrum imaging. In order to collect an elemental map with reasonable signal-to-noise ratio, however, a much higher electron probe current and prolonged acquisition time are required. A spectrum image with, for example, 60x60 pixels, would take from a few minutes to an hour depending on the signal level. In contrast, a HAADF image with 1024x1024 pixels typically takes no more than 30s. Thus, the atomic number contrast information delivered via HAADF imaging provides an alternative and quick way of performing chemical analysis in STEM.

One idealized scenario for such an application is to map out the core-shell structure in bimetallic nanoparticles with a large Z difference between the two components. Examples from Au-Pd bimetallic nanoparticles are shown in Figure 19. Since Au is much heavier than Pd, Au-rich layers generate much higher HAADF image contrast than Pd-rich layers. Thus, the distinctive intensity variation across the particles provides a direct indication of the spatial distribution of Au and Pd in the bimetallic nanoparticles, assuming there is no other element present in the particles. It is, however, highly desirable to perform simultaneous XEDS or EELS analysis to further confirm the qualitative elemental distribution information derived from HAADF image and provide quantitative compositional information.

Figure 19 near here.

One major benefit from aberration correction is the significant improvement in signal-to-noise ratio in ADF images, which allows for atom-by-atom chemical analysis in some simple cases based on quantitative image analysis<sup>39</sup>. Figure 20A shows the dependency of ADF image intensity on atomic number for light elements under specific experimental settings, following a  $Z^{1.64}$  relationship. (See above for discussion of the origins of this power law behavior.) It should be noted that the exact relationship depends on the ADF collector settings and the way image intensity is quantified (see supplementary of Reference<sup>39</sup> for details). Based on this dependency, Krivanek *et al.* were able to identify every atom in an h-BN monolayer containing C and O impurities via quantitative image analysis as shown in Figure 20B<sup>39</sup>. This method has also been applied to identify single impurities in graphene and carbon nanotubes<sup>64</sup> that are catalysis-related. The atom-by-atom chemical analysis via ADF imaging would become an easier practice when given some pre-knowledge about the samples. For example, in MoS<sub>2</sub>

catalysts, it is important to know the edge termination of the MoS<sub>2</sub> layers since the edges are believed to be the active sites for many catalysis reactions<sup>86</sup>. There could be three types of basic edge terminations, Mo-termination, S<sub>2</sub>-termination, and mono-S-termination, showing distinct levels of ADF image intensity. The image in Figure 20C shows that the atoms on the MoS<sub>2</sub> edge display image intensity about half of the regular S<sub>2</sub> sites, suggesting that this particular MoS<sub>2</sub> platelet has its Mo edge capped with single sulfur atoms. Similarly, for the supported (Pt,Ru)/Al<sub>2</sub>O<sub>3</sub> catalyst shown in Figure 20D, it is reasonable to assign the atoms with higher image intensity as Pt and those with lower intensity as Ru, assuming there are not many impurities in the sample. Even though single atom chemical analysis has been demonstrated using both EDS and EELS<sup>56,87</sup>, such atom-by-atom chemical mapping is almost impossible using conventional STEM-EELS or STEM-XEDS analysis due to the high mobility of the atoms on the free surface and the low signal from individual atoms. In this aspect, the chemical information obtained from quantitative ADF imaging, especially combined with image simulation, is highly valuable for practical catalyst characterization.

Figure 20 near here.

The HAADF image intensity not only depends on the atomic number but also on the number of atoms in the image column. This provides a feasible way to count the number of atoms in a catalyst nanoparticle and estimate its three dimensional shape. Using size-selected and soft-landed Au nanoclusters, Li *et al.* demonstrated that the integrated HAADF image intensity, after proper background subtraction, is proportional to the number of Au atoms within the imaged cluster as shown in Figure 21A<sup>88</sup>. This linear dependency is valid for small nanoparticles containing up to a few thousand heavy metal atoms. By counting the number of atoms based on HAADF image intensity (using a calibration curve such as the one shown in Figure 21A, obtained from standard samples) and measuring the diameter of the clusters directly from the image, it is then possible to estimate the three-dimensional shape of the clusters using simplified hemispherical or spherical particle models<sup>89</sup>. Such information would be important for understanding the contact interface between the metal particles and the support materials. The atom counting approach can be pushed one step further with aberration corrected STEM. LeBeau *et al.* showed that by carefully measuring the experimental parameters combined with image simulation, column-by-column atom counting can be achieved (Figure 21B) for samples with thickness smaller than the depth of focus, without the need for a calibration standard<sup>90</sup>.

Figure 21 near here.

It should be mentioned that the situation in real catalyst samples (*e.g.* bimetallic nanoparticles) is usually much more complicated with both atomic number contrast and mass-thickness contrast mixed in the same HAADF image. Combining quantitative image intensity analysis with image simulation, thus, becomes important for figuring out the full structure of nanoparticles. A beautiful demonstration is given by Ortalan *et al.* in a study of bimetallic (Rh, Ir) catalysts supported on MgO support<sup>68</sup>. The distribution and three-dimensional configuration of metal atoms on the oxide support surface obtained from HAADF imaging can serve as useful structural input for density-functional theory (DFT) calculations. Such DFT calculations can in turn help to verify the structural models proposed from image analysis, and to understand the surface structures, the metal-support interactions, and the origins of catalytic performance of different structures.

Three-dimensional characterization via STEM depth-sectioning or tilt-tomography

As discussed above, another important benefit from aberration correction is that the depth of focus ( $\Delta z$ ) of the STEM probe can be dramatically reduced because a much larger probe forming aperture can now be used. The depth of focus in STEM mode follows a  $\Delta z \approx \lambda/\theta^2$  dependency, where  $\theta$  is the illumination semi-angle as defined by the probe forming aperture. (See Fig. 12.) Typical aberration corrected instruments have a convergence semi-angle around 30 mrad, which brings the depth of focus (without considering aberrations) down to ~6 nm for 60 kV, ~3 nm for 200 kV and ~2 nm for 300 kV. This means different parts of the sample in the depth direction can be imaged under optimum focus separately, providing a way to obtain the three-dimensional structural information via through-focal HAADF image series (or depth sectioning).

Figure 22 near here.

An example through-focal HAADF image series is shown in Figure 22A, acquired from a Au/FeO<sub>x</sub> catalyst originally prepared by coprecipitation (which means Au can be trapped inside the FeO<sub>x</sub> lattice or on the internal surface of voids inside the FeO<sub>x</sub> support particles). The sample was subsequently leached to remove Au particles from the outside surface. The HAADF images from the leached sample, however, still show the presence of many Au particles, presumably contained within the bulk of the FeO<sub>x</sub> supports. In order to test the catalytic activity of Au particles (by comparing the performance of the parent catalyst and the leached catalyst), it is important to determine the depth position of these residual Au particles. During depth-sectioning, it can be seen from Figure 23A that different structural features, including the edges of the voids and Au particles, come into optimum focus at different defocus values. These data helped to conclude that the remaining Au particles after leaching are trapped on the internal surface of voids inside the FeO<sub>x</sub> particles<sup>69</sup>. Similarly, STEM depth sectioning can be applied to identify the depth position of individual metal atoms on/inside the support particles<sup>66</sup>. It should be noted that even though 3D structural information can be retrieved from through-focal series, 3D reconstruction of nano-objects via depth sectioning suffers significant elongation artifact due to the missing-cone problem<sup>91</sup>. As illustrated in Figure 22B, the nm-sized Pd-Au nanoparticles appear elongated in the depth direction after depth-sectioning reconstruction.

The elongation problem described in Figure 22B can be partially overcome by tilt-series HAADF-STEM tomography<sup>92</sup>, which provides a robust way for 3D imaging and presently offers depth and transverse resolution at the nm scale. For this purpose, the incoherent HAADF signal is much preferred, as compared to bright field signals, since they are less affected by diffraction contrast and satisfy the projection requirement for tomography<sup>92</sup>. In terms of applications in catalyst study, there are two most important aspects of the 3D structural information that can be extracted from HAADF-STEM tilt-tomography: i) the 3D spatial distribution and correlation of catalyst particles on the support surface, and ii) the contact interface between the catalyst particles and the support materials.

As shown in Figure 23A, using HAADF-STEM tilt-tomography, the 3D distribution of Pt-Co particles on a light-weight carbon support, (a promising fuel cell cathode catalyst for oxygen reduction reaction) can be reconstructed. One major task in the study of this catalyst system is to understand the coarsening mechanisms of the Pt<sub>3</sub>Co catalyst particles during chemical aging, one of the two major barriers for the commercialization of proton exchange membrane fuel cells. In order to probe this, Yu *et al.*<sup>93</sup> first mapped out the Pt-Co particle distribution prior to the electrochemical experiments. The sample on an index TEM grid was then loaded into an electrochemical cell for aging. The use of the index TEM grid made it possible to locate the same region of the catalyst material for tomography study before and after electrochemical aging. By combining the 3D reconstructions of the same catalyst aggregate into the same

reconstructed model, one-to-one correspondence of the Pt-Co particles before and after aging can be obtained and clearly visualized, as shown in Figure 23A. This allows the tracking of particle coalescence and migration for every single nanoparticle on the surface. Yu *et al.*<sup>93</sup> found that coalescence, instead of Ostwald ripening, is the major mechanism for the growth of Pt-Co particles during electrochemical aging, which further suggests that minimizing the particle movement on the surface could potentially help to slow down the degradation of the catalyst<sup>93</sup>.

Figure 23 near here.

3D tomography reconstruction can also help to identify the surface crystallography of the support materials and the contact interface between the catalyst particles and the support materials. Figure 23B shows a reconstruction of Au particles dispersed on the surface of  $\text{Ce}_{0.5}\text{Tb}_{0.12}\text{Zr}_{0.38}\text{O}_{2-x}$  mixed oxide support. The angles between the exposed facets of the support materials were measured to be  $\sim 110^\circ$  from the reconstruction, a characteristic interplanar angle between  $\{111\}$  planes of a cubic crystal. Moreover, it can be seen that most of the Au particles tend to segregate at the  $\{111\}$  facet vertices or stepped sites<sup>94</sup>. Such valley sites between two  $\{111\}$  facets help to increase the contact interface area between the Au particles and the support, which lowers the total energy. This type of information can help to understand the stability and catalytic behavior of the catalysts.

#### Challenges and new opportunities in the application of HAADF-STEM to catalytic materials

As briefly reviewed above, aberration-corrected HAADF-STEM imaging can provide useful structural information about heterogeneous catalysts down to the single-atom level, and help to establish correlations between the catalyst structure and performance. One should also recognize the limitations and challenges that accompany the strengths of STEM techniques. For the study of catalysts, one should always ask the question: are we seeing the true structure?

The answer to this question is related to the possibility that structural modifications occur during sample handling/preparation, under realistic catalytic reaction conditions, from electron-beam-induced structure damage etc. Insufficient sampling can also bias the perceived distribution of features. Most of the results discussed in this section are considered to be from *ex-situ* experiments, *i.e.* the catalysts are removed from their working environment, prepared into electron-transparent TEM samples, and studied under room-temperature and high vacuum inside the microscope. TEM sample preparation for catalyst samples is usually made by crushing, which does not introduce damage as does the ion milling used for crystalline samples. One must make sure that the sample contains the representative structural features of the bulk catalyst, however, and that the structure does not change during handling. For example, exposing the sample to moisture and air could sometimes cause oxidation to catalysts containing transition metal nanoparticles<sup>95</sup> or changing the surface structure of bulk oxides<sup>96</sup>. For such sensitive samples, one should prepare, store and transport them in dry containers preferably protected with inert gas if possible.

It is also important to keep in mind that the key structural parameters of heterogeneous catalysts, including size, shape, and composition of the active species, can change under reaction conditions, which usually involve elevated temperature and a reactive gaseous environment<sup>97</sup>. *In-situ* characterization under conditions similar to the working environment of the catalysts could potentially help to reveal the “true” structure of the catalysts under reaction. Heating capability and a reaction gas environment are usually required for performing such *in-situ* microscopy studies, which could be achieved using two different approaches. The first approach is via the use of a dedicated environmental (S)TEM, in which a low gas pressure up to 50 mbar (5 kPa) can be maintained around the sample stage and isolated from the rest of the high-vacuum microscope column using a set of specially designed objective polepieces and a differential pumping system<sup>97</sup>. A more popular and “low-cost” approach uses various MEMS-

based *in-situ* sample holders that can be fitted into most regular (S)TEM instruments. These *in-situ* holders usually use two electron-transparent ceramic membranes to support the catalyst particles and to isolate an ultra-thin gas (or liquid) layer into a mini reaction cell. The heating capability can be achieved by electrical resistance heating of the ceramic membranes. Using this approach, a gas pressure up to one atmosphere and heating temperature exceeding 1000 °C can be achieved with extremely fast heating/cooling rate ( $\sim 10^6$  °C per second)<sup>98</sup>. More importantly, using the second approach, the electron beam only needs to go through an additional thin layer of gas (a few  $\mu\text{m}$  to a few tens of  $\mu\text{m}$  thick) and two thin ceramic films ( $< 50$  nm). Therefore, there is little degradation of the spatial resolution. In fact, Allard *et al.* recently demonstrated atomic resolution HAADF and STEM-BF imaging of noble metal nanoparticles at elevated temperatures and atmosphere gas pressure<sup>98</sup>. Direct imaging of single metal atoms under atmosphere pressure and elevated temperature has not been demonstrated, however, we expect that this could be achieved in the near future with optimized experimental settings combining the latest aberration-corrected STEM technology with an improved *in-situ* cell design. The *in-situ* techniques mentioned here are under active development, and could have a significant impact on catalysis research. The dynamic structural evolution during catalyst synthesis, catalytic reaction, and catalyst regeneration, obtained via *in-situ* characterization, could bring new insights into the induction and degradation mechanisms. This new information can ultimately lead to a better understanding of the structure-activity relationships and help us to design better catalysts.

Electron-beam-induced damage is an important issue for all electron microscopy studies. Catalyst samples are more prone to e-beam damage due to the small clusters/particles and surface species involved. Sequential imaging technique provides a quick way to evaluate the beam damage effect and the reliability of the structural information obtained and for the selection of experimental conditions. Generally speaking, low accelerating voltage could help to reduce damage to metal nanoparticles, while oxide catalysts could benefit from the use of high electron beam energy. Low-dose settings usually help to reduce beam damage, and are essential for some e-beam sensitive oxide systems, *e.g.* zeolitic materials. A general discussion of e-beam damage and strategies to minimize beam damage can be found in many TEM textbooks. It should be also noted that for most supported catalyst materials, some degree of surface diffusion of surface atoms cannot be avoided during STEM imaging. As long as the structures shown in sequential images are statistically the same, they can be considered as a “true” representation of the real structure in the material.

Last but not least, the sampling issue. Since catalysts are usually structurally inhomogeneous, we must make sure that the local structural information obtained from STEM imaging of nm-size areas is representative, *i.e.* random sampling of a large number of areas is essential. Moreover, it is desirable that the STEM results be compared to and combined with information from other “averaged” techniques, including optical spectroscopy analysis (Raman, IR and UV-vis), low energy ion scattering (LEIS) from the outermost surface layer and conventional X-ray and TEM/SEM characterization, which provide information from a larger volume of the sample. Such comparison can help to verify the structural information obtained from STEM is consistent with other characterization results, and combining all information together could potentially provide a full view of the catalyst structure down to the atomic scale.

#### **Nanocrystal optical properties:**

As anticipated by Feynman<sup>99</sup>, tremendous advances in the science of the nano-scale have accompanied the development of atomic-resolution microscopy. As perhaps the quintessential example, the study of nanocrystals has provided fertile ground for the application of HAADF-STEM.

The key features of nano-scale matter are; the onset of quantum effects with decreasing physical size and the dominance of surface atoms over those in the bulk<sup>100</sup>. The first of these key features, quantum size effects, is manifest in nanocrystals where their smallness causes quantum confinement<sup>101</sup>. This can be understood by analogy to the classic elementary quantum mechanics model of the 'infinite square well'. The smaller the nanocrystal the more confined the electron wavefunctions become and the higher the energies of the energy bands. Furthermore, because the lifting of the bands by quantum confinement is nonlinear with respect to energy, increasing higher energy levels more than lower energy levels, quantum confinement increases the band gaps of semiconductors. By controlling their size one can tune the width of their band gaps, making them of major interest for a wide range of applications from lighting and solar cell applications to an alternative to fluorescent dyes in biological imaging<sup>102-107</sup>.

Nanocrystals composed of CdSe are among the most studied as it is possible to tune their band gaps across the visual range. This allows one to produce nanocrystals that emit monochromatic light from red to blue with very high quantum efficiencies. This control is illustrated in Figure 24 which shows vials of CdSe nanocrystals of different sizes in suspension, emitting under the stimulation of ultraviolet light. Imaging samples of the CdSe nanocrystals with aberration corrected STEM shows that they possess the same wurtzite crystal structure as bulk CdSe but are only a small number of unit cells wide<sup>102,108,109</sup>. Representative Z-contrast STEM images of CdSe nanocrystals from samples tuned to approximately 7 nm, 5 nm and 3 nm in diameter are shown in Figure 25 alongside optical spectra taken from the same samples. The 7 nm nanocrystals emit red light, the 5 nm nanocrystals emit orange light and the 3 nm nanocrystals emit green light. The images highlight the significant scale of the unit cell in comparison to the whole nanocrystal for those which quantum confinement has a significant effect.

Figure 24 near here.

Figure 25 near here.

In the effort to create ever smaller CdSe nanocrystals it was discovered that when made even smaller than those emitting blue light, instead of emitting monochromatically in the ultraviolet range as one would expect from further confinement, they emit a broad spectrum spanning the visual range and appearing white to the eye<sup>110-112</sup> as shown in Figure 26. Although the absorption edge onset continued to increase in energy as the size was decreased below 2 nm, the emission spectra remained the same for all diameters below 2 nm<sup>113,114</sup>. These white light emitting nanocrystals were synthesized with the same surfactant mixture of dodecylphosphonic acid, hexadecylamine and tri-n-octylphosphine oxide as the larger monochromatic CdSe nanocrystals, the reaction was merely stopped earlier to keep them at a size of 2 nm or less. TEM and STEM confirmed the ultrasmall sizes of the white light emitting samples, meaning that a blend of colors coming from different sizes of nanocrystals could be ruled out as the cause<sup>102,115</sup>. Furthermore, by producing samples with a high dispersion of the white light emitting nanocrystals it was possible to perform optical spectroscopy on single nanocrystals that showed that individual particles emit across the visual range<sup>111</sup>. Optical spectra from four individual ultrasmall CdSe nanoparticles are shown in Fig. 27 alongside the average of 216 such single nanocluster spectra. The ultrasmall CdSe nanoclusters emit spectra with different fine structure features, but each one emits a broad spectrum spanning the visual range. This is also true when using different ligands in the synthesis of the ultrasmall CdSe nanocrystals<sup>114</sup>. As shown in Figure 28, using different ligands changed the relative heights of the peaks seen in the optical emission spectra, but the emission still spans the visual range. By using a mixture of the ligands one can tint or balance the emission as desired.

Figure 26 near here.

Figure 27 near here.

Figure 28 near here.

Light emitting diodes (LEDs) offer extremely high efficiency for monochromatic light sources. The development of the blue LED<sup>116,117</sup> has revolutionized lighting by allowing white light to be produced with a mixture of red green and blue LEDs, albeit at high cost. An alternative approach is to use phosphors, however, this significantly reduces the total device efficiency due to self absorption. As absorption by ultrasmall CdSe mostly occurs very near or in the ultraviolet range, with very little overlap with their white light emission, they would therefore seem to make an ideal phosphor for use in conjunction with an ultraviolet LED. The quantum efficiency of the ultrasmall CdSe was initially only about 3%<sup>112</sup>, however, far lower than the near 100% efficiencies achieved with larger monochromatic CdSe based core shell nanocrystals, prompting research into the origin of the broad emission.

The first theories on the origin of the white light centered around surface defect trap states in the band gap<sup>112-115</sup>, but such states cannot explain the sudden appearance of a continuous spectrum of transition energies spanning the visual range when the diameter is reduced below 2 nm, particularly in spectra acquired from single nanoparticles. Dynamic STEM observations revealed that the ultrasmall white light emitting particles behave quite differently under the electron beam than the larger monochromatic CdSe nanocrystals<sup>102</sup>. By recording atomic resolution images in very quick succession, it became apparent that the monochromatic nanocrystals had stable crystal cores surrounded by a disordered layer of atoms which continuously rearrange themselves. The fluctuating surface layer is difficult to see in the images of the 5 and 7 nm nanocrystals shown in Fig. 24 due to the contrast being optimized for the crystal cores in the middle, which have higher intensities due to their greater thickness. The image of the 3 nm green light emitting nanocrystal however clearly shows a region of diffuse intensity surrounding the crystal core due to the motion blurring of the atoms near the surface. Figure 29 shows frames from a movie of an ultrasmall CdSe nanocluster. The ultrasmall nanoclusters were found to be entirely fluxional. It is as if the fluxional surface seen around the larger monochromatic nanocrystals consumes the entirety of the ultrasmall CdSe nanoclusters. All the ultrasmall CdSe particles behaved this way regardless of the accelerating voltage (60–300 kV).

Figure 29 near here.

Although the motions observed by dynamic STEM were likely driven by the energy from the fast electron beam, the ultraviolet photons used to pump the nanoclusters also provide significant thermal energy and could produce similar behaviors. Almost all of the photons emitted by the nanoclusters have energies significantly less than 3 eV so most of the excited electrons transfer considerable amounts of energy into phonons before emitting a photon. As the lower bound of the white light spectrum is about 1.7 eV, up to 1.3 eV of energy is transferred to heat by each excitation event. As they are composed of so few atoms, for ultrasmall nanoclusters this represents a substantial amount of energy per atom. For instance, if one assumes that the number of atoms per unit volume is the same as in bulk wurtzite CdSe, a perfectly spherical 2 nm diameter nanocrystal would contain 150 atoms and the number of atoms decreases rapidly

as the radius is made smaller. A spherical 54 atom wurtzite cluster would have a diameter of 1.4 nm. Simple equipartition gives the energy per atom as  $(3/2)kT$  where  $k$  is the Boltzmann constant and  $T$  is the temperature. Using this relation one finds that 1.3 eV shared among 54 atoms, 24 meV per atom, corresponds to an effective temperature of 186 K. When added to room temperature (300 K), this gives an effective temperature of around 500 K.

Density functional theory has been used to explore the effects of such thermal energy on ultrasmall CdSe nanoclusters with quantum mechanical molecular dynamics (MD) simulations<sup>102</sup>. The simulations showed that the energy transferred to phonons can induce structural fluxionality that in turn leads to a fluctuating band gap. The 54 atom CdSe ultrasmall nanocluster used in the simulations was initially formed in the wurtzite crystal structure, but soon lost its crystallinity. Furthermore, it was found that the disordered structure produced by MD is energetically preferable to the wurtzite structure, suggesting the ultrasmall CdSe clusters are inherently disordered.

Figure 30 shows the structure of the nanocluster evolving during the simulations performed at 500 K. The structural changes may seem subtle, but the range of energies through which the band gap fluctuated in the simulations was of a very similar width to the experimental white light spectrum. The changes that occurred in the densities of states (DOS) as a function of time are illustrated in Fig. 31. The DOS were calculated at intervals of 40 fs during the simulation, and are colored according to the lowest energy gap appearing in each, including a rigid shift of 1.2 eV to account for the well known underestimation of the band gap by DFT, which is particularly severe for CdTe. As can be seen in the figure, the band gap energy fluctuates, taking on energies corresponding to all the colors of the rainbow, from red to blue. As white light is composed of the combination of all the colors, this suggests that the fluctuating band gap resulting from the structural fluxionality results in a white time averaged emission spectrum.

Figure 30 near here.

Figure 31 near here.

In fact if one places a Gaussian at each possible emission energy appearing in a set such subsequent DOS, it is possible to simulate the time averaged emission spectrum of the ultrasmall nanocluster. Figure 32 shows such a simulated emission spectrum created by summing 0.2 eV full width half maximum Gaussians at each possible emission energy seen from a set of 20 DOS calculated at intervals of 40 fs during the MD simulation. The resemblance of the simulated emission spectrum to the experimental white light spectrum shown in the same figure on the same energy scale is remarkable. A perfect match to experiment is not to be expected as the fine features of the experimental spectrum are determined by the ligands<sup>113,114</sup> which are absent in the simulation. The extra atoms and larger supercells required to include ligands in the simulations make extended simulations with ligands impractical, however limited simulations with ligands showed similar levels of fluxionality. Furthermore, whatever ligands are used in the experiments, the emission spectrum of the ultrasmall CdSe remains similarly broad and continuous<sup>113,114</sup>, features that the simulations show can be explained through structural fluxionality. Therefore it seems most likely that the underlying cause of the white light emission is the fluxionality while the ligands tint the perceived color of emission by causing certain structural configurations to be favored over others if the mixture of ligands is not balanced. In addition other nanoclusters that possess size-tunable monochromatic emission when small exhibit broad spectra when made ultrasmall<sup>118-123</sup>, suggesting fluxionality may have implications beyond CdSe.

Figure 32 near here.

If one examines the charge densities of the states participating in the transitions across the band gap, the highest occupied and lowest unoccupied states of the nanocluster, one finds that they do not exist simply at the surface. Rather, as shown in Fig. 33 the states nearest the band gap all extend through large portions of the nanocluster, with some enveloping the entire cluster<sup>102</sup>. It is therefore not possible to describe them as either surface or core states. Other simulations of ultrasmall semiconductor nanoparticles also show the states nearest the band gaps distributed through much or all of the nanoparticles<sup>124-126</sup>.

Figure 33 near here.

At this ultrasmall size the second key feature of nano-scale matter appears; the majority of the atoms are adjacent to the surface and all are very close to the surface. The fluxional surface layer seen around the larger monochromatic CdSe nanocrystals is about a nanometer thick for all the nanocrystal sizes observed. The fact that the transition from monochromatic to white light emission occurs at a diameter twice the thickness of the fluxional surface seen around the larger nanocrystals seems unlikely to be a coincidence. Rather it seems likely that 1 nm is the distance needed between the surface and the internal atoms before they no longer “see” the surface and form into a crystalline core. In other words, ultrasmall nanoclusters can be thought of as composed entirely of surface, and distinguishing between surface and core states is no longer possible. While small is different, ultrasmall is different yet again.

#### Conclusions:

Aberration-corrected HAADF-STEM imaging has evolved from the very first hints of imaging individual uranium atoms on a thin carbon substrate<sup>8</sup> to become a very powerful tool to study the physical chemistry of materials at the atomic scale. Subsequent developments have enhanced its capability with simultaneous real-space imaging and elemental identification by using electron energy loss spectroscopy (EELS), 3-dimensional (3D) mapping by depth sectioning and monitoring of surface diffusion by time-sequencing of images.

Herein we have reviewed some recent developments in the application of HAADF-STEM for heterogeneous catalyst research, and to the study of semiconducting nanoparticles. The rapid development of new instrumentation and *in-situ* techniques promises to further open up exciting opportunities to probe catalyst structure under realistic working conditions. Further advances of HAADF-STEM in combination with other characterization techniques and atomistic simulations will continue to advance the field of nanoscience, where the onset of quantum properties and the dominance of surface atoms over those in the bulk happen at a size scale that is perfectly matched to the capabilities of this technique.

#### Acknowledgements:

KS thanks Andrew Lupini for discussions of aberration correction in electron lensing. WZ thanks Chris Kiely and Qian He for useful discussions on catalyst characterization and funding from Wigner Fellowship through the Laboratory Directed Research and Development Program of Oak Ridge National Laboratory, managed by UT-Battelle, LLC, for the U. S. DOE. The authors collectively would like to thank their collaborators Sokrates T. Pantelides, Sandra J. Rosenthal, James R. McBride, Andrew Lupini, Maria Varela, Albina Y. Borisevich, Nigel D. Browning, Matthew F. Chisholm, Peter D. Nellist, Eiji, Abe, Gerd Duscher, Wu Zhou, Junjie Guo, Ondrej Krivanek, Niklas Dellby.

Figure captions:

Figure 1. Schematic of HAADF-STEM, with simultaneous EELS on electrons scattered to low angles, reproduced from Ref. <sup>127</sup>.

Figure 2. STEM images taken with annular detectors capturing electrons scattered into different ranges of angles. Note that contrast from thermal vibration is stronger in the image taken with a medium-angle detector than in the image taken in the high-angle detector. Adapted from Ref<sup>128</sup>.

Figure 3. (a) First atomic-resolution image of Pt/alumina, reproduced from Ref. <sup>15</sup>. (b) a more recent and higher-resolution image, reproduced from Ref. <sup>16</sup>.

Figure 4. (a) HAADF-STEM images of Rh/alumina catalytic. (b) closeup of indicated regions of (a). (c) simulated image based on Rh<sub>2</sub>O<sub>3</sub>-II/γ-alumina (100). Reproduced from Ref. <sup>23</sup>.

Figure 5. Bulk structure of the high-pressure Rh<sub>2</sub>O<sub>3</sub>-II phase of rhodia, reproduced from Ref. <sup>23</sup>.

Figure 6. Z-STEM images of single-layer boron nitride. (a) As recorded, (b) rotated and corrected for distortion, and Fourier-filtered to reduce noise and probe tails. (c) Line profiles through the locations marked in (b), normalized to one for a single B atom. Inset at top right in (a) shows the Fourier transform of an image area away from the thicker regions. The two arrows point to (11-20) and (20-20) reflections of the hexagonal BN that correspond to recorded spacings of 1.26 and 1.09 Å. Taken with a Nion UltraSTEM operating at 60 kV, reproduced from Ref. <sup>39</sup>.

Figure 7. Schematic energy level diagram (LHS) showing the origin of an EELS spectrum with corresponding hypothetical EELS spectrum (RHS).

Figure 8. Spatially resolved EELS showing a dramatic decrease in Co L-edge intensity between the cobalt silicide and silicon sides of a CoSi<sub>2</sub>-Si interface. Reproduced from Ref. <sup>49</sup>.

Figure 9. Real-space HAADF-STEM image of a SrTiO<sub>3</sub>/ Y<sub>2</sub>O<sub>3</sub>-ZrO<sub>2</sub> / SrTiO<sub>3</sub> heterostructure together with EELS images taken at the Ti-L and O-K spectral edges, along with a composite of the latter two, reproduced from Ref. <sup>52</sup>. The image reveals direct evidence of the oxygen disorder in the Y<sub>2</sub>O<sub>3</sub>-ZrO<sub>2</sub> region where the oxygen positions are not resolved due to the increased disorder.

Figure 10. HAADF-STEM image of a CaTiO<sub>3</sub> thin film (a). The highlighted columns were then probed with EELS, (b) revealing the presence of a single La impurity. Reproduced from Ref. <sup>55</sup>.

Figure 11. STEM-EEL spectrum imaging of monolayer graphene with dopant atoms. (A) Low-pass filtered ADF survey image showing the specific area that was used for spectrum imaging (same area as Figure 5B). (B) ADF signal collected simultaneously during spectrum imaging. Sub-pixel scanning was not applied during data acquisition. (C-E) Si-L-, C-K-, and N-K-edge maps extracted from the STEM-EEL spectrum image. The blue and green squares indicate the positions of the substitutional Si and N atoms respectively. B-E are raw data. Scale bars: 0.2nm. Adapted from Ref. <sup>129</sup>.

Figure 12. Cartoon showing how increasing the beam convergence angle results in a decrease in the total depth over which the beam is confined to a given cross sectional area.

Figure 13. A series of HAADF-STEM images for a sample of La/TiO<sub>2</sub> approximately 6nm thick, reproduced from Ref. <sup>58</sup>. The focus depth was varied from 0, (the "top" of the specimen) to -10 nm. Note that there are two different focus depths at which the contrast is sharp. These correspond to dopant La atoms located on the top and bottom surfaces of the flake. This conclusion is given numerical support in the accompanying graph, which plots the mean image intensity (arbitrary units) versus focus depth.

Figure 14. Heavy Au atom clusters decorating the exterior of a Si nanostructure, reproduced from Ref. <sup>60</sup>.

Figure 15. Time sequence of images showing the diffusion of a Si atom along a graphene edge.

Figure 16. Identification of active Au cluster using HAADF-STEM imaging. (A and B) Representative HAADF images of (A) an inactive and (B) an active Au/FeO<sub>x</sub> catalyst for low temperature CO oxidation. White circles: isolated Au atoms; black circles: sub-nm Au clusters. (C) Relative populations of different supported Au species as a function of catalyst calcination temperature and measured CO conversion (listed as percentage in brackets). The population of bilayer Au clusters decreases with decreasing CO conversion. Reprinted from Ref. <sup>70</sup> with permission from AAAS.

Figure 17. HAADF-STEM imaging of several single atom catalysts. (A) Single Pt atoms dispersed on FeO<sub>x</sub> support for CO oxidation, reproduced from Ref. <sup>67</sup>. (B) Single Nb atoms incorporated in onion-like graphitic carbon support for oxygen reduction reaction, reproduced from Ref. <sup>65</sup>. (C) Ir atoms dispersed on Zeolite HSSZ-53 for ethylene hydrogenation, reproduced from Ref. <sup>76</sup>. The bright features on the HAADF images are the isolated single metal atoms with some of them circled for emphasis.

Figure 18. Identification of active Zr-WO<sub>x</sub> cluster in supported WO<sub>x</sub>/ZrO<sub>2</sub> catalysts using HAADF-STEM imaging. Representative HAADF images of supported WO<sub>3</sub>/ZrO<sub>2</sub> catalysts with low (A) and high (B, C) activities. Blue circles: surface mono-tungstate species; green circles: surface poly-tungstate species; red circles: highly active Zr-WO<sub>x</sub> mixed oxide clusters, ~1 nm in diameter. The presence of Zr atoms in the Zr-WO<sub>x</sub> cluster induces distinct contrast variations at neighboring atomic positions as highlighted in Figure C. Figures A and B reprinted from Ref. <sup>73</sup> with permission. Figure C reprinted from Ref. <sup>71</sup> with permission.

Figure 19. HAADF-STEM images of core-shell nanoparticles. (A) Pd-Au-Pd three layer nanoparticles with Pd core, Au-rich inner shell, and Pd-rich outer shell, reproduced from Ref. <sup>130</sup>. (B) Au-Pd particle with Au-rich core and Pd-rich shell, reproduced from Ref. <sup>71</sup>. *Inserts*: Intensity line profile as indicated on the image.

Figure 20. Atom-by-atom chemical analysis via STEM-ADF imaging. (A) ADF image intensity as a function of atomic number under given experimental conditions, reproduced from Ref. <sup>39</sup>. (B) ADF image of monolayer h-BN with C and O impurities. Structural model obtained from image analysis is overlaid. Green: N; red: B, Yellow: C; Blue: O, reproduced from Ref. <sup>39</sup>. (C) ADF image of MoS<sub>2</sub> catalyst revealing the Mo edge is terminated by single sulfur atoms, reproduced from Ref. <sup>131</sup> (D) HAADF image from Pt-Ru/γ-Al<sub>2</sub>O<sub>3</sub>, reproduced from Ref. <sup>132</sup>.

Figure 21. Atom counting based on HAADF image intensity quantification. (A) Integrated HAADF intensity of size-selected Au clusters on amorphous carbon film as a function of the number of Au atoms, showing a linear relationship. Inset shows the image intensity distribution for Au<sub>309</sub> clusters, reproduced from Ref. <sup>88</sup> (B) HAADF image of a wedge-shaped gold film along [110] direction. The number of atoms contained in each atomic column is indicated next to the atomic columns, reproduced from Ref. <sup>90</sup>.

Figure 22. 3D particle distribution obtained via STEM depth-sectioning. (A) Through-focus HAADF image series of a supported Au/FeO<sub>x</sub> catalyst. Voids (V1,2) and Au particles (P1,2) inside the support material come into optimum focus at different defocus values, providing the relative depth positions for these structural features, reproduced from Ref. <sup>69</sup>. (B) A reconstruction of the 3D structure of Pt-Au particles dispersed on TiO<sub>2</sub> support, obtained via STEM depth-sectioning, showing significant elongation artifact of the Pt-Au particles in the depth direction, reproduced from Ref. <sup>57</sup>.

Figure 23. 3D reconstruction of nanoparticles dispersed on support surface, obtained via HAADF-STEM tilt tomography. (A) A reconstruction of Pt-Co nanoparticles on the carbon support before (gold) and after (red) electrochemical aging, showing the coalescence and migration of catalyst particles during aging, reproduced from Ref. <sup>93</sup>. (B) Surface-rendered reconstruction showing the distribution of Au nanoparticles on a metal oxide support. Dashed lines indicate the vertices of {111} facets, reproduced from Ref. <sup>94</sup>.

Figure 24. Suspensions of CdSe nanocrystals of various sizes emitting under the stimulation of ultraviolet light, reproduced from Ref. <sup>133</sup>.

Figure 25. High resolution Z-contrast STEM images and optical spectra from samples of 7 nm, 5 nm and 3 nm CdSe nanocrystals emitting monochromatic red light (a and b), orange light (c and d) and green light (e and f) respectively. Scale bars indicate the size of 1 nm. Adapted from Ref. <sup>102</sup>.

Figure 26. White light emission from ultrasmall sub-2-nm CdSe nanoclusters. (a) Photograph of a vial of ultrasmall CdSe nanoclusters in suspension emitting white light under the stimulation of ultraviolet light. (b) Optical spectrum of the white light emission. Adapted from Refs. <sup>111</sup> and <sup>102</sup>.

Figure 27. (a) Optical emission spectra from individual ultrasmall CdSe nanoclusters. (b) The average of 216 spectra taken from individual ultrasmall CdSe nanoclusters. Reproduced from Ref. <sup>111</sup>.

Figure 28. Emission spectra from 1.6 nm ultrasmall nanoclusters coated in octylphosphonic acid (blue), dodecanthiol (red), oleic acid (black), and pyridine (green). Reproduced from Ref. <sup>114</sup>.

Figure 29. Successive frames from an atomic resolution Z-contrast STEM movie of an ultrasmall CdSe nanocluster. The scale bar indicates the size of 1 nm. Adapted from Ref. <sup>102</sup>.

Figure 30. Structural fluxionality seen in an ultrasmall Cd<sub>27</sub>Se<sub>27</sub> nanocluster during quantum mechanical molecular dynamics simulations performed at 500 K. Adapted from Ref. <sup>102</sup>.

Figure 31. Densities of states of the fluctuating ultrasmall CdSe nanocluster calculated at 40 fs intervals during MD simulation at 500 K. The colors correspond to the color of the lowest energy transitions on the shifted energy scale for each time point. Adapted from Ref. <sup>102</sup>.

Figure 32. Comparison of the experimental optical emission spectra of ultrasmall CdSe nanoclusters (a) and the simulated emission spectrum resulting from the time average of the fluctuating band gaps (b). Adapted from Ref. <sup>102</sup>.

Figure 33. The distribution of the states immediately below (a-c) and above (d-f) the bandgap of the ultrasmall  $\text{Cd}_{27}\text{Se}_{27}$  nanocluster for one of the configurations which occurred during the 500 K molecular dynamics simulations. The charge density isosurfaces are plotted at 1% of their maximum. Reproduced from Ref. <sup>102</sup>.

## References:

- 1 Pennycook, S.J. & Jesson, D.E., High-resolution Z-contrast imaging of crystals. *Ultramicroscopy* **37** (1-4), 14-38 (1991). [http://dx.doi.org/http://dx.doi.org/10.1016/0304-3991\(91\)90004-P](http://dx.doi.org/http://dx.doi.org/10.1016/0304-3991(91)90004-P)
- 2 Steinfeld, J.I., Francisco, J.S., & Hase, W.L., *Chemical Kinetics and Dynamics*. (Prentice Hall, Englewood Cliffs, NJ, 1989).
- 3 Ng, A., Poplawsky, J.D., Li, C., Pennycook, S.J., & Rosenthal, S.J., Direct Electronic Property Imaging of a Nanocrystal-Based Photovoltaic Device by Electron Beam-Induced Current via Scanning Electron Microscopy. *The Journal of Physical Chemistry Letters* **5** (5), 856-860 (2014). <http://dx.doi.org/10.1021/jz402752k>
- 4 Loos, J., Sourty, E., Lu, K., de With, G., & v. Bavel, S., Imaging Polymer Systems with High-Angle Annular Dark Field Scanning Transmission Electron Microscopy (HAADF-STEM). *Macromolecules* **42** (7), 2581-2586 (2009). <http://dx.doi.org/10.1021/ma8026589>
- 5 de Jonge, N., Sougrat, R., Northan, B.M., & Pennycook, S.J., Three-Dimensional Scanning Transmission Electron Microscopy of Biological Specimens. *Microscopy and Microanalysis* **16** (01), 54-63 (2010). <http://dx.doi.org/doi:10.1017/S1431927609991280>
- 6 Gustafsson, M.G.L., Nonlinear structured-illumination microscopy: Wide-field fluorescence imaging with theoretically unlimited resolution. *Proceedings of the National Academy of Sciences of the United States of America* **102** (37), 13081-13086 (2005). <http://dx.doi.org/10.1073/pnas.0406877102>
- 7 Klar, T.A., Jakobs, S., Dyba, M., Egner, A., & Hell, S.W., Fluorescence microscopy with diffraction resolution barrier broken by stimulated emission. *Proceedings of the National Academy of Sciences* **97** (15), 8206-8210 (2000). <http://dx.doi.org/10.1073/pnas.97.15.8206>
- 8 Crewe, A.V., Wall, J., & Langmore, J., Visibility of Single Atoms. *Science* **168** (3937), 1338-1340 (1970). <http://dx.doi.org/10.1126/science.168.3937.1338>
- 9 Wall, J., Langmore, J., Isaacson, M., & Crewe, A.V., Scanning-Transmission Electron-Microscopy at High-Resolution. *Proceedings Of The National Academy Of Sciences Of The United States Of America* **71**, 1-5 (1974)
- 10 Pennycook, S.J., Z-contrast STEM for materials science. *Ultramicroscopy* **30** (1-2), 58-69 (1989). [http://dx.doi.org/http://dx.doi.org/10.1016/0304-3991\(89\)90173-3](http://dx.doi.org/http://dx.doi.org/10.1016/0304-3991(89)90173-3)
- 11 Howie, A., Marks, L.D., & Pennycook, S.J., New imaging methods for catalyst particles. *Ultramicroscopy* **8** (1-2), 163-174 (1982). [http://dx.doi.org/http://dx.doi.org/10.1016/0304-3991\(82\)90285-6](http://dx.doi.org/http://dx.doi.org/10.1016/0304-3991(82)90285-6)
- 12 Pennycook, S.J., Howie, A., Shannon, M.D., & Whyman, R., Characterization of supported catalysts by high-resolution STEM. *J. Molec. Catal. A* **20**, 345 (1983)
- 13 Bradley, S.A., Cohn, M.J., & Pennycook, S.J., Z-contrast imaging of supported Pt and Pd clusters. *Microscopy Research and Technique* **28** (5), 427-429 (1994). <http://dx.doi.org/10.1002/jemt.1070280509>
- 14 Vonharrach, H.S., Nicholls, A.W., Jesson, D.E., & Pennycook, S.J., First results of a 300 kV high-resolution field-emission STEM in *Electron Microscopy and Analysis 1993*, edited by A. J. Craven (IOP Publishing Ltd, Bristol, 1993), pp. 499-502.
- 15 Nellist, P.D. & Pennycook, S.J., Direct imaging of the atomic configuration of ultradispersed catalysts. *Science* **274**, 413 (1996)
- 16 Sohlberg, K., Rashkeev, S., Borisevich, A.Y., Pennycook, S.J., & Pantelides, S.T., Origin of anomalous Pt-Pt distances in the Pt/alumina catalytic system. *Chem. Phys. Chem.* **5**, 1893-1897 (2004)

- 17 Cheng, D., Huang, S., & Wang, W., Structures of small Pd-Pt bimetallic clusters by Monte Carlo simulation. *Chemical Physics* **330** (3), 423-430 (2006). <http://dx.doi.org/http://dx.doi.org/10.1016/j.chemphys.2006.09.015>
- 18 Nasluzov, V.A., Rivanenkov, V.V., Shor, A.M., Neyman, K.M., & Rosch, N., Pd<sub>3</sub> and Pt<sub>3</sub> species on the  $\alpha$ -alumina(0001) surface: cluster modes embedded in an elastic polarizable environment. *Chem. Phys. Lett.* **374**, 487-495 (2003)
- 19 Yates, D.J.C., Murrell, L.L., & Prestridge, E.B., Ultradispersed rhodium rafts: Their existence and topology. *Journal of Catalysis* **57** (1), 41-63 (1979). [http://dx.doi.org/http://dx.doi.org/10.1016/0021-9517\(79\)90042-3](http://dx.doi.org/http://dx.doi.org/10.1016/0021-9517(79)90042-3)
- 20 Zhuo, S. & Sohlberg, K., Origin of stability of the high-temperature, low-pressure Rh<sub>2</sub>O<sub>3</sub> III form of rhodium sesquioxide. *Journal of Solid State Chemistry* **179** (7), 2126-2132 (2006)
- 21 Campbell, C.T., Transition Metal Oxides: Extra Thermodynamic Stability as Thin Films. *Phys. Rev. Lett.* **96**, 066106 (2006)
- 22 Zhuo, S. & Sohlberg, K., Platinum dioxide phases: relative thermodynamic stability and kinetics of inter-conversion from first-principles. *Physica B* **381**, 12-19 (2006)
- 23 Sohlberg, K., Zhuo, S., Nellist, P., Peng, Y., & Pennycook, S., Evidence of High-Pressure Rhodium Sesquioxide in the Rhodium/gamma-Alumina Catalytic System. *J. Phys. Chem. C.* **112** (31), 11831-11834 (2008). <http://dx.doi.org/10.1021/jp801089j>
- 24 Nellist, P.D. & Pennycook, S.J., Subangstrom Resolution by Underfocused Incoherent Transmission Electron Microscopy. *Physical Review Letters* **81** (19), 4156-4159 (1998)
- 25 Scherzer, O., Sparische und chromatische Korrektur von Elektronen-Linsen. *Optik* **2**, 114-132 (1947)
- 26 Rose, H., History of aberration correction in *Advances in Imaging and Electron Physics: Aberration corrected electron microscopy* (Academic Press, Amsterdam, 2008), Vol. 153.
- 27 Deltrap, J.H.M., *Correction of Spherical Aberration of Electron Lenses*. (Cambridge University Press., Cambridge, 1964).
- 28 Crewe, A.V., Some Chicago Aberrations. *Microsc. Microanal.* **10**, 414-419 (2004). <http://dx.doi.org/10.1017/S1431927604040085>
- 29 Rose, H.H., Historical aspects of aberration correction. *Journal of Electron Microscopy* (2009). <http://dx.doi.org/10.1093/jmicro/dfp012>
- 30 Dalglish, R.L., Winchester, T., & Smith, A.M., A new concept for improved ion and electron lenses - Aberration corrected systems of planar electrostatic deflection elements. *Nuclear Instruments and Methods in Physics Research* **218** (1-3), 7-10 (1983). [http://dx.doi.org/http://dx.doi.org/10.1016/0167-5087\(83\)90945-6](http://dx.doi.org/http://dx.doi.org/10.1016/0167-5087(83)90945-6)
- 31 Dalglish, R.L., Corrected electrostatic lens systems for ion beams. *Nuclear Instruments and Methods in Physics Research* **191** (1-3), 191-198 (1981). [http://dx.doi.org/http://dx.doi.org/10.1016/0029-554X\(81\)91004-1](http://dx.doi.org/http://dx.doi.org/10.1016/0029-554X(81)91004-1)
- 32 Dalglish, R.L., Smith, A.M., & Hughes, S., Geometric aberration correction in ion lenses - the Caledonian quadruplet. *Nuclear Instruments and Methods in Physics Research* **215** (1-2), 9-15 (1983). [http://dx.doi.org/http://dx.doi.org/10.1016/0167-5087\(83\)91286-3](http://dx.doi.org/http://dx.doi.org/10.1016/0167-5087(83)91286-3)
- 33 Pennycook, S.J., Rafferty, B., & Nellist, P.D., Z-contrast imaging in an aberration-corrected scanning transmission electron microscope. *Microscopy and Microanalysis* **6** (4), 343-352 (2000)
- 34 Batson, P.E., Dellby, N., & Krivanek, O.L., Sub-angstrom resolution using aberration corrected electron optics. *Nature* **418** (6898), 617-620 (2002). <http://dx.doi.org/10.1038/nature00972>
- 35 Batson, P.D., N. & Krivanek, O.L., Sub-Angstrom Probe Size in HADF-STEM at 120KV. *Microscopy and Microanalysis* **8** (2), 14-15 (2002)

- 36 Krivanek, O.L., Dellby, N., & Lupin, A.R., Towards sub-Å electron beams. *Ultramicroscopy* **78**, 1-11 (1999)
- 37 McBride, J.R., Kippeny, T.C., Pennycook, S.J., & Rosenthal, S.J., Aberration-corrected Z-contrast scanning transmission electron microscopy of CdSe nanocrystals. *Nano Letters* **4** (7), 1279-1283 (2004). <http://dx.doi.org/10.1021/nl04906q>
- 38 Varela, M., Lupini, A.R., van Benthem, K., Borisevich, A.Y., Chisholm, M.F., Shibata, N., Abe, E., & Pennycook, S.J., Materials characterization in the aberration-corrected scanning transmission electron microscope in *Annual Review of Materials Research* (Annual Reviews, Palo Alto, 2005), Vol. 35, pp. 539-569.
- 39 Krivanek, O.L., Chisholm, M.F., Nicolosi, V., Pennycook, T.J., Corbin, G.J., Dellby, N., Murfitt, M.F., Own, C.S., Szilagyi, Z.S., Oxley, M.P., Pantelides, S.T., & Pennycook, S.J., Atom-by-atom structural and chemical analysis by annular dark-field electron microscopy. *Nature* **464** (7288), 571-574 (2010). <http://dx.doi.org/10.1038/nature08879>
- 40 Jin, C., Lin, F., Suenaga, K., & Iijima, S., Fabrication of a Freestanding Boron Nitride Single Layer and Its Defect Assignments. *Physical Review Letters* **102** (19), 195505 (2009). <http://dx.doi.org/10.1103/PhysRevLett.102.195505>
- 41 Alem, N., Erni, R., Kisielowski, C., Rossell, M., Gannett, W., & Zettl, A., Atomically thin hexagonal boron nitride probed by ultrahigh-resolution transmission electron microscopy. *Physical Review B* **80** (15), 155425 (2009). <http://dx.doi.org/10.1103/PhysRevB.80.155425>
- 42 Meyer, J., Chuvilin, A., Algara-Siller, G., Biskupek, J., & Kaiser, U., Selective Sputtering and Atomic Resolution Imaging of Atomically Thin Boron Nitride Membranes. *Nano Letters* **9** (7), 2683-2689 (2009). <http://dx.doi.org/10.1021/nl9011497>
- 43 Crewe, A.V., Scanning Electron Microscopes: Is High Resolution Possible? *Science* **154** (3750), 729-738 (1966). <http://dx.doi.org/10.2307/1719832>
- 44 delaPena, F., Berger, M.-H., Hochepeid, J.-F., Dynys, F., Stephan, O., & Walls, M., Mapping titanium and tin oxide phases using EELS: An application of independent component analysis. *Ultramicroscopy* **111**, 169-176 (2011)
- 45 Moreno, M.S., Egerton, R.F., Rehr, J.J., & Midgley, P.A., Electronic structure of tin oxides by electron energy loss spectroscopy and real-space multiple scattering calculations. *Physical Review B* **71** (3), 035103 (2005)
- 46 Moreno, M.S., Egerton, R.F., & Midgley, P.A., Differentiation of tin oxides using electron energy-loss spectroscopy. *Physical Review B* **69** (23), 233304 (2004)
- 47 Hillier, J. & Baker, R.F., Microanalysis by Means of Electrons. *Journal of Applied Physics* **15** (9), 663-675 (1944)
- 48 Duscher, G., Browning, N.D., & Pennycook, S.J., Atomic Column Resolved Electron Energy-Loss Spectroscopy. *physica status solidi (a)* **166** (1), 327-342 (1998). [http://dx.doi.org/10.1002/\(sici\)1521-396x\(199803\)166:1<327::aid-pssa327>3.0.co;2-r](http://dx.doi.org/10.1002/(sici)1521-396x(199803)166:1<327::aid-pssa327>3.0.co;2-r)
- 49 Browning, N.D., Chisholm, M.F., & Pennycook, S.J., Atomic-resolution chemical analysis using a scanning transmission electron microscope. *Nature* **366** (6451), 143-146 (1993)
- 50 Allen, L.J., Findlay, S.D., Lupini, A.R., Oxley, M.P., & Pennycook, S.J., Atomic-Resolution Electron Energy Loss Spectroscopy Imaging in Aberration Corrected Scanning Transmission Electron Microscopy. *Physical Review Letters* **91** (10), 105503 (2003)
- 51 Pennycook, T.J., Beck, M.J., Varga, K., Varela, M., Pennycook, S.J., & Pantelides, S.T., Origin of Colossal Ionic Conductivity in Oxide Multilayers: Interface Induced Sublattice Disorder. *Physical Review Letters* **104** (11), 4. <http://dx.doi.org/115901>  
10.1103/PhysRevLett.104.115901

- 52 Pennycook, T.J., Oxley, M.P., Garcia-Barriocanal, J., Bruno, F.Y., Leon, C., Santamaria, J., Pantelides, S.T., Varela, M., & Pennycook, S.J., Seeing oxygen disorder in YSZ/SrTiO<sub>3</sub> colossal ionic conductor heterostructures using EELS. *Eur. Phys. J.-Appl. Phys* **54** (3), 11 (2011). <http://dx.doi.org/33507>  
10.1051/epjap/2011100413
- 53 Garcia-Barriocanal, J., Rivera-Calzada, A., Varela, M., Sefrioui, Z., Iborra, E., Leon, C., Pennycook, S.J., & Santamaria, J., Colossal ionic conductivity at interfaces of epitaxial ZrO<sub>2</sub>: Y<sub>2</sub>O<sub>3</sub>/SrTiO<sub>3</sub> heterostructures. *Science* **321** (5889), 676-680 (2008). <http://dx.doi.org/10.1126/science.1156393>
- 54 Varela, M., Findlay, S.D., Lupini, A.R., Christen, H.M., Borisevich, A.Y., Dellby, N., Krivanek, O.L., Nellist, P.D., Oxley, M.P., Allen, L.J., & Pennycook, S.J., Spectroscopic imaging of single atoms within a bulk solid. *Phys. Rev. Lett.* **92**, 095502 (2004)
- 55 Varela, M., Gazquez, J., & Pennycook, S.J., STEM-EELS imaging of complex oxides and interfaces. *MRS Bulletin* **37** (1), 29 (2012)
- 56 Zhou, W., Kapetanakis, M., Prange, M.P., Pantelides, S.T., Pennycook, S.J., & Idrobo, J.C., Direct determination of the chemical bonding of individual impurities in graphene. *Physical Review Letters* **109**, 206803 (2012)
- 57 Borisevich, A.Y., Lupini, A.R., & Pennycook, S.J., Depth sectioning with the aberration-corrected scanning transmission electron microscope. *Proceedings of the National Academy of Sciences of the United States of America* **103** (9), 3044-3048 (2006). <http://dx.doi.org/10.1073/pnas.0507105103>
- 58 Wang, S., Borisevich, A.Y., Rashkeev, S.N., Glazoff, M.V., Sohlberg, K., Pennycook, S.J., & Pantelides, S.T., The role of dopants in the stabilization of catalysts. *Nature Materials* **3**, 143-146 (2004)
- 59 van Benthem, K., Lupini, A.R., Kim, M., Baik, H.S., Doh, S., Lee, J.H., Oxley, M.P., Findlay, S.D., Allen, L.J., Luck, J.T., & Pennycook, S.J., Three-dimensional imaging of individual hafnium atoms inside a semiconductor device. *Applied Physics Letters* **87** (3), 3 (2005). <http://dx.doi.org/10.1063/1.1991989>
- 60 Oh, S.H., van Benthem, K., Molina, S.I., Borisevich, A.Y., Luo, W.D., Werner, P., Zakharov, N.D., Kumar, D., Pantelides, S.T., & Pennycook, S.J., Point defect configurations of supersaturated Au atoms inside Si nanowires. *Nano Letters* **8** (4), 1016-1019 (2008). <http://dx.doi.org/10.1021/nl072670>
- 61 Roberts, K.G., Varela, M., Rashkeev, S., Pantelides, S.T., Pennycook, S.J., & Krishnan, K.M., Defect-mediated ferromagnetism in insulating Co-doped anatase TiO<sub>2</sub> thin films. *Physical Review B* **78** (1), 014409 (2008). <http://dx.doi.org/10.1103/PhysRevB.78.014409>
- 62 Haruta, M. & Date, M., Advances in the catalysis of Au nanoparticles. *Applied Catalysis A-General* **222** (1-2), 427-437 (2001). [http://dx.doi.org/10.1016/s0926-860x\(01\)00847-x](http://dx.doi.org/10.1016/s0926-860x(01)00847-x)
- 63 Pennycook, S.J., Seeing the atoms more clearly: STEM imaging from the Crewe era to today. *Ultramicroscopy* **123**, 28-37 (2012). <http://dx.doi.org/10.1016/j.ultramic.2012.05.005>
- 64 Li, Y., Zhou, W., Wang, H., Xie, L., Liang, Y., Wei, F., Idrobo, J.C., Pennycook, S.J., & Dai, H., An oxygen reduction electrocatalyst based on carbon nanotube-graphene complexes. *Nature Nanotechnology* **7**, 394-400 (2012)
- 65 Zhang, X., Guo, J., Guan, P., Liu, C., Huang, H., Xue, F., Dong, X., Pennycook, S.J., & Chisholm, M.F., Catalytically active single-atom niobium in graphitic layers. *Nature Communications* **4** (2013). <http://dx.doi.org/10.1038/ncomms2929>

- 66 Wang, S., Borisevich, A.Y., Rashkeev, S.N., Glazoff, M.V., Sohlberg, K., Pennycook, S.J., & Pantelides, S.T., Dopants adsorbed as single atoms prevent degradation of catalysts. *Nature Materials* **3** (3), 143-146 (2004)
- 67 Qiao, B., Wang, A., Yang, X., Allard, L.F., Jiang, Z., Cui, Y., Liu, J., Li, J., & Zhang, T., Single-atom catalysis of CO oxidation using Pt-1/FeO<sub>x</sub>. *Nature Chemistry* **3** (8), 634-641 (2011). <http://dx.doi.org/10.1038/nchem.1095>
- 68 Ortalan, V., Uzun, A., Gates, B.C., & Browning, N.D., Towards full-structure determination of bimetallic nanoparticles with an aberration-corrected electron microscope. *Nature Nanotechnology* **5** (12), 843-847 (2010)
- 69 Allard, L.F., Flytzani-Stephanopoulos, M., & Overbury, S.H., Behavior of Au species in Au/Fe<sub>2</sub>O<sub>3</sub> catalysts characterized by novel in situ heating techniques and aberration-corrected STEM imaging. *Microscopy and Microanalysis* **16** (4), 375-385 (2010). <http://dx.doi.org/10.1017/s1431927610013486>
- 70 Herzing, A.A., Kiely, C.J., Carley, A.F., Landon, P., & Hutchings, G.J., Identification of active gold nanoclusters on iron oxide supports for CO oxidation. *Science* **321** (5894), 1331-1335 (2008)
- 71 Zhou, W., Wachs, I.E., & Kiely, C.J., Nanostructural and chemical characterization of supported metal oxide catalysts by aberration corrected analytical electron microscopy. *Current Opinion in Solid State and Materials Science* **16** (1), 10-22 (2012)
- 72 Sultaniadis, N., Zhou, W., Psarras, A.C., Gonzalez, A.J., Iliopoulou, E.F., Kiely, C.J., Wachs, I.E., & Wong, M.S., Relating pentane isomerization activity to the acidic properties and surface density of WO<sub>x</sub>/ZrO<sub>2</sub>. *Journal of the American Chemical Society* **132** (Journal Article), 13462-13471 (2010)
- 73 Zhou, W., Ross-Medgaarden, E.I., Knowles, W.V., Wong, M.S., Wachs, I.E., & Kiely, C.J., Identification of active Zr-WO<sub>x</sub> clusters on ZrO<sub>2</sub> support for solid acid catalysts. *Nature Chemistry* **1**, 722-728 (2009)
- 74 Yu, J., Woo, J., Borisevich, A., Xu, Y., & Gulians, V.V., A combined HAADF STEM and density functional theory study of tantalum and niobium locations in the Mo–V–Te–Ta(Nb)–O M1 phases. *Catalysis Communications* **29**, 68-72 (2012)
- 75 Pyrz, W.D., Blom, D.A., Sadakane, M., Kodato, K., Ueda, W., Vogt, T., & Buttrey, D.J., Atomic-scale investigation of two-component MoVO complex oxide catalysts using aberration-corrected high-angle annular dark-field imaging. *Chem. Mat.* **22**, 2033-2040 (2010)
- 76 Aydin, C., Lu, J., Liang, A.J., Chen, C.-Y., Browning, N.D., & Gates, B.C., Tracking iridium atoms with electron microscopy: First steps of metal nanocluster formation in one-dimensional Zeolite channels. *Nano Letters* **11** (12), 5537-5541 (2011). <http://dx.doi.org/10.1021/nl2034305>
- 77 Ortalan, V., Uzun, A., Gates, B.C., & Browning, N.D., Direct imaging of single metal atoms and clusters in the pores of dealuminated HY zeolite. *Nature Nanotechnology* **5** (7), 506-510 (2010)
- 78 Thomas, J.M. & Midgley, P.A., The merits of static and dynamic high-resolution electron microscopy (HREM) for the study of solid catalysts. *ChemCatChem* **2** (7), 783-798 (2010)
- 79 Yang, X.-F., Wang, A., Qiao, B., Li, J., Liu, J., & Zhang, T., Single-atom catalysts: a new frontier in heterogeneous catalysis. *Accounts Chem. Res.* **46** (8), 1740-1748 (2013). <http://dx.doi.org/10.1021/ar300361m>
- 80 Flytzani-Stephanopoulos, M. & Gates, B.C., Atomically dispersed supported metal catalysts in *Annual Review of Chemical and Biomolecular Engineering*, edited by J. M. Prausnitz (2012), Vol. 3, pp. 545-574.

- 81 Zhou, W., Oxley, M.P., Lupini, A.R., Krivanek, O.L., Pennycook, S.J., & Idrobo, J.C., Single atom microscopy. *Microscopy and Microanalysis* **18**, 1342-1354 (2012)
- 82 Haruta, M., Kobayashi, T., Sano, H., & Yamada, N., Novel gold catalysts for the oxidation of carbon-monoxide at a temperature far below 0°C. *Chemistry Letters* (2), 405-408 (1987). <http://dx.doi.org/10.1246/cl.1987.405>
- 83 Chen, M.S. & Goodman, D.W., The structure of catalytically active gold on titania. *Science* **306** (5694), 252-255 (2004)
- 84 Ross-Medgaarden, E.I., Knowles, W.V., Kim, T., Wong, M.S., Zhou, W., Kiely, C.J., & Wachs, I.E., New insights into the nature of the acidic catalytic active sites present in ZrO<sub>2</sub>-supported tungsten oxide catalysts. *Journal of Catalysis* **256** (1), 108-125 (2008)
- 85 Zhang, B., Zhang, W., & Su, D.S., Towards a more accurate particle size distribution of supported catalyst by using HAADF-STEM. *ChemCatChem* **3** (6), 965-968 (2011). <http://dx.doi.org/10.1002/cctc.201100096>
- 86 Basenbacher, F., Brorson, M., Clausen, B.S., Helveg, S., Hinnemann, B., Kibsgaard, J., Lauritsen, J.V., Moses, P.G., Norskov, J.K., & Topsoe, H., Recent STM, DFT and HAADF-STEM studies of sulfide-based hydrotreating catalysts: Insight into mechanistic, structural and particle size effects. *Catalysis Today* **130**, 86-96 (2008)
- 87 Lovejoy, T.C., Ramasse, Q.M., Falke, M., Kaepfel, A., Terborg, R., Zan, R., Dellby, N., & Krivanek, O.L., Single atom identification by energy dispersive X-ray spectroscopy. *Applied Physics Letters* **100**, 154101 (2012)
- 88 Li, Z.Y., Young, N.P., Di Vece, M., Palomba, S., Palmer, R.E., Bleloch, A.L., Curley, B.C., Johnston, R.L., Jiang, J., & Yuan, J., Three-dimensional atomic-scale structure of size-selected gold nanoclusters. *Nature* **451** (7174), 46-48 (2008)
- 89 Pearmain, D., Park, S.J., Wang, Z.W., Abdela, A., Palmer, R.E., & Li, Z.Y., Size and shape of industrial Pd catalyst particles using size-selected clusters as mass standards. *Applied Physics Letters* **102** (16) (2013). <http://dx.doi.org/10.1063/1.4801986>
- 90 LeBeau, J.M., Findlay, S.D., Allen, L.J., & Stemmer, S., Standardless atom counting in scanning transmission electron microscopy. *Nano Letters* **10** (11), 4405-4408 (2010). <http://dx.doi.org/10.1021/nl102025s>
- 91 Xin, H.L. & Muller, D.A., Aberration-corrected ADF-STEM depth sectioning and prospects for reliable 3D imaging in S/TEM. *Journal of electron microscopy* **58** (3), 157-165 (2009). <http://dx.doi.org/10.1093/jmicro/dfn029>
- 92 Midgley, P.A. & Weyland, M., 3D electron microscopy in the physical sciences: the development of Z-contrast and EFTEM tomography. *Ultramicroscopy* **96** (3-4), 413-431 (2003). [http://dx.doi.org/10.1016/s0304-3991\(03\)00105-0](http://dx.doi.org/10.1016/s0304-3991(03)00105-0)
- 93 Yu, Y., Xin, H.L., Hovden, R., Wang, D., Rus, E.D., Mundy, J.A., Muller, D.A., & Abruna, H.D., Three-dimensional tracking and visualization of hundreds of Pt-Co fuel cell nanocatalysts during electrochemical aging. *Nano Letters* **12** (9), 4417-4423 (2012). <http://dx.doi.org/10.1021/nl203920s>
- 94 Gonzalez, J.C., Hernandez, J.C., Lopez-Haro, M., del Rio, E., Delgado, J.J., Hungria, A.B., Trasobares, S., Bernal, S., Midgley, P.A., & Juan Calvino, J., 3D characterization of gold nanoparticles supported on heavy metal oxide catalysts by HAADF-STEM electron tomography. *Angew. Chem.-Int. Edit.* **48** (29), 5313-5315 (2009). <http://dx.doi.org/10.1002/anie.200901308>
- 95 Wang, H., Zhou, W., Liu, J., Si, R., Sun, G., Zhong, M., Su, H., Zhao, H., Rodriguez, J.A., Pennycook, S.J., Idrobo, J.C., Li, W., Kou, Y., & Ma, D., Platinum-modulated cobalt nanocatalysts for low-temperature aqueous-phase Fischer-Tropsch synthesis. *Journal of the American Chemical Society* **135**, 4149-4158 (2013)

- 96 Wachs, I.E., Recent conceptual advances in the catalysis science of mixed metal oxide catalytic materials. *Catalysis Today* **100** (1-2), 79-94 (2005)
- 97 Hansen, P.L., Wagner, J.B., Helveg, S., Rostrup-Nielsen, J.R., Clausen, B.S., & Topsoe, H., Atom-resolved imaging of dynamic shape changes in supported copper nanocrystals. *Science* **295** (5562), 2053-2055 (2002)
- 98 Allard, L.F., Overbury, S.H., Bigelow, W.C., Katz, M.B., Nackashi, D.P., & Damiano, J., Novel MEMS-based gas-cell/heating specimen holder provides advanced imaging capabilities for in situ reaction studies. *Microscopy and Microanalysis* **18** (4), 656-666 (2012). <http://dx.doi.org/10.1017/s1431927612001249>
- 99 Feynman, R.P., There's plenty of room at the bottom. *Eng. and Sci.* **23**, 22 (1960)
- 100 Sohlberg, K., Introducing the core concepts of nanoscience and nanotechnology: Two vignettes. *J. Chem. Ed.* **83**, 1516 (2006). <http://dx.doi.org/10.1021/ed083p1516>
- 101 Brus, L.E., Electron-electron and electron-hole interactions in small semiconductor crystallites: The size dependence of the lowest excited electronic state. *The Journal of Chemical Physics* **80** (9), 4403-4409 (1984). <http://dx.doi.org/doi:http://dx.doi.org/10.1063/1.447218>
- 102 Pennycook, T.J., McBride, J.R., Rosenthal, S.J., Pennycook, S.J., & Pantelides, S.T., Dynamic Fluctuations in Ultrasmall Nanocrystals Induce White Light Emission. *Nano Letters* **12** (6), 3038-3042. <http://dx.doi.org/10.1021/nl3008727>
- 103 Schreuder, M.A., Gosnell, J.D., Smith, N.J., Warnement, M.R., Weiss, S.M., & Rosenthal, S.J., Encapsulated white-light CdSe nanocrystals as nanophosphors for solid-state lighting. *Journal of Materials Chemistry* **18** (9), 970-975 (2008). <http://dx.doi.org/10.1039/b716803a>
- 104 Huynh, W.U., Dittmer, J.J., & Alivisatos, A.P., Hybrid Nanorod-Polymer Solar Cells. *Science* **295** (5564), 2425-2427 (2002). <http://dx.doi.org/10.1126/science.1069156>
- 105 Coe, S., Woo, W.-K., Bawendi, M., & Bulovic, V., Electroluminescence from single monolayers of nanocrystals in molecular organic devices. *Nature* **420** (6917), 800-803 (2002)
- 106 Bruchez, M., Moronne, M., Gin, P., Weiss, S., & Alivisatos, A.P., Semiconductor Nanocrystals as Fluorescent Biological Labels. *Science* **281** (5385), 2013-2016 (1998). <http://dx.doi.org/10.1126/science.281.5385.2013>
- 107 Colvin, V.L., Schlamp, M.C., & Alivisatos, A.P., Light-emitting diodes made from cadmium selenide nanocrystals and a semiconducting polymer. *Nature* **370** (6488), 354-357 (1994)
- 108 McBride, J.R., Lupini, A.R., Schreuder, M.A., Smith, N.J., Pennycook, S.J., & Rosenthal, S.J., Few-Layer Graphene as a Support Film for Transmission Electron Microscopy Imaging of Nanoparticles. *ACS Applied Materials & Interfaces* **1** (12), 2886-2892 (2009). <http://dx.doi.org/10.1021/am900608j>
- 109 Rosenthal, S.J., McBride, J., Pennycook, S.J., & Feldman, L.C., Synthesis, surface studies, composition and structural characterization of CdSe, core/shell and biologically active nanocrystals. *Surface Science Reports* **62** (4), 111-157 (2007). <http://dx.doi.org/http://dx.doi.org/10.1016/j.surfrep.2007.02.001>
- 110 Jose, R., Zhelev, Z., Bakalova, R., Baba, Y., & Ishikawa, M., White-light-emitting CdSe quantum dots synthesized at room temperature. *Applied Physics Letters* **89** (1), 013115-013115-013113 (2006). <http://dx.doi.org/10.1063/1.2219510>
- 111 Dukes, A.D., Samson, P.C., Keene, J.D., Davis, L.M., Wikswo, J.P., & Rosenthal, S.J., Single-Nanocrystal Spectroscopy of White-Light-Emitting CdSe Nanocrystals. *The Journal of Physical Chemistry A* **115** (16), 4076-4081 (2010). <http://dx.doi.org/10.1021/jp1109509>

- 112 Bowers, M.J., McBride, J.R., & Rosenthal, S.J., White-Light Emission from Magic-Sized Cadmium Selenide Nanocrystals. *Journal of the American Chemical Society* **127** (44), 15378-15379 (2005). <http://dx.doi.org/10.1021/ja055470d>
- 113 McBride, J.R., Dukes Iii, A.D., Schreuder, M.A., & Rosenthal, S.J., On ultrasmall nanocrystals. *Chemical Physics Letters* **498** (1-3), 1-9 (2010). <http://dx.doi.org/http://dx.doi.org/10.1016/j.cplett.2010.08.052>
- 114 Dukes, A.D., Schreuder, M.A., Sammons, J.A., McBride, J.R., Smith, N.J., & Rosenthal, S.J., Pinned emission from ultrasmall cadmium selenide nanocrystals. *The Journal of Chemical Physics* **129** (12), 121102 (2008). <http://dx.doi.org/doi:http://dx.doi.org/10.1063/1.2983632>
- 115 Bowers Ii, M.J., McBride, J.R., Garrett, M.D., Sammons, J.A., Dukes Iii, A.D., Schreuder, M.A., Watt, T.L., Lupini, A.R., Pennycook, S.J., & Rosenthal, S.J., Structure and Ultrafast Dynamics of White-Light-Emitting CdSe Nanocrystals. *Journal of the American Chemical Society* **131** (16), 5730-5731 (2009). <http://dx.doi.org/10.1021/ja900529h>
- 116 Shuji, N., Masayuki, S., Shin-ichi, N., Naruhito, I., Takao, Y., Toshio, M., Hiroyuki, K., & Yasunobu, S., InGaN-Based Multi-Quantum-Well-Structure Laser Diodes. *Japanese Journal of Applied Physics* **35** (1B), L74 (1996)
- 117 Isamu, A., Hiroshi, A., Shigetoshi, S., Hiromitsu, S., Toshiyuki, T., & Masayoshi, K., Stimulated Emission by Current Injection from an AlGaIn/GaN/GaInN Quantum Well Device. *Japanese Journal of Applied Physics* **34** (11B), L1517 (1995)
- 118 Devadas, M.S., Kim, J., Sinn, E., Lee, D., Goodson, T., & Ramakrishna, G., Unique Ultrafast Visible Luminescence in Monolayer-Protected Au<sub>25</sub> Clusters. *The Journal of Physical Chemistry C* **114** (51), 22417-22423 (2010). <http://dx.doi.org/10.1021/jp107033n>
- 119 Rayevska, O.E., Grodzyuk, G.Y., Dzhagan, V.M., Stroyuk, O.L., Kuchmiy, S.Y., Plyusnin, V.F., Grivin, V.P., & Valakh, M.Y., Synthesis and Characterization of White-Emitting CdS Quantum Dots Stabilized with Polyethylenimine. *The Journal of Physical Chemistry C* **114** (51), 22478-22486 (2010). <http://dx.doi.org/10.1021/jp108561u>
- 120 Dagtepe, P., Chikan, V., Jasinski, J., & Leppert, V.J., Quantized Growth of CdTe Quantum Dots; Observation of Magic-Sized CdTe Quantum Dots. *The Journal of Physical Chemistry C* **111** (41), 14977-14983 (2007). <http://dx.doi.org/10.1021/jp072516b>
- 121 Chen, X., Samia, A.C.S., Lou, Y., & Burda, C., Investigation of the Crystallization Process in 2 nm CdSe Quantum Dots. *Journal of the American Chemical Society* **127** (12), 4372-4375 (2005). <http://dx.doi.org/10.1021/ja0458219>
- 122 Soloviev, V.N., Eichhöfer, A., Fenske, D., & Banin, U., Size-Dependent Optical Spectroscopy of a Homologous Series of CdSe Cluster Molecules. *Journal of the American Chemical Society* **123** (10), 2354-2364 (2001). <http://dx.doi.org/10.1021/ja003598j>
- 123 Landes, C.F., Braun, M., & El-Sayed, M.A., On the Nanoparticle to Molecular Size Transition: Fluorescence Quenching Studies. *The Journal of Physical Chemistry B* **105** (43), 10554-10558 (2001). <http://dx.doi.org/10.1021/jp0118726>
- 124 Puzder, A., Williamson, A.J., Grossman, J.C., & Galli, G., Surface Chemistry of Silicon Nanoclusters. *Physical Review Letters* **88** (9), 097401 (2002)
- 125 Puzder, A., Williamson, A.J., Gygi, F.o., & Galli, G., Self-Healing of CdSe Nanocrystals: First-Principles Calculations. *Physical Review Letters* **92** (21), 217401 (2004)
- 126 Pennycook, T.J., Hadjisavvas, G., Idrobo, J.C., Kelires, P.C., & Pantelides, S.T., Optical gaps of free and embedded Si nanoclusters: Density functional theory calculations. *Physical Review B* **82** (12), 125310

- 127 Pennycook, S.J., Browning, N.D., McGibbon, M.M., McGibbon, A.J., Jesson, D.E., & Chisholm, M.F., Direct Determination of Interface Structure and Bonding with the Scanning Transmission Electron Microscope. *Philosophical Transactions of the Royal Society of London. Series A: Mathematical, Physical and Engineering Sciences* **354** (1719), 2619-2634 (1996). <http://dx.doi.org/10.1098/rsta.1996.0119>
- 128 Varela, M., Lupini, A.R., Benthem, K.v., Borisevich, A.Y., Chisholm, M.F., Shibata, N., Abe, E., & Pennycook, S.J., Materials Characterization in the Aberration-corrected Scanning Transmission Electron Microscope. *Annual Review of Materials Research* **35** (1), 539-569 (2005). <http://dx.doi.org/doi:10.1146/annurev.matsci.35.102103.090513>
- 129 Zhou, W., Lee, J., Nanda, J., Pantelides, S.T., Pennycook, S.J., & Idrobo, J.-C., Atomically localized plasmon enhancement in monolayer graphene. *Nat Nano* **7** (3), 161-165 (2012)
- 130 Ferrer, D., Blom, D.A., Allard, L.F., Mejia, S., Perez-Tijerina, E., & Jose-Yacaman, M., Atomic structure of three-layer Au/Pd nanoparticles revealed by aberration-corrected scanning transmission electron microscopy. *Journal of Materials Chemistry* **18** (21), 2442-2446 (2008). <http://dx.doi.org/10.1039/b801320a>
- 131 Hansen, L.P., Ramasse, Q.M., Kisielowski, C., Brorson, M., Johnson, E., Topsoe, H., & Helveg, S., Atomic-scale edge structures on industrial-style MoS<sub>2</sub> nanocatalysts. *Angew. Chem.-Int. Edit.* **50** (43), 10153-10156 (2011)
- 132 Borisevich, A.Y., Wang, S., Rashkeev, S.N., Pantelides, S.T., Sohlberg, K., & Pennycook, S.J., Single-atom sensitivity for solving catalysis problems. *Microscopy and Microanalysis* **10** (Suppl 2), 460-461 (2004)
- 133 Pennycook, T., McBride, J., Rosenthal, S., Pantelides, S., & Pennycook, S., Structure of White Light Emitting CdSe Nanocrystals. *Microscopy and Microanalysis* **17** (SupplementS2), 1636-1637 (2011). <http://dx.doi.org/doi:10.1017/S1431927611009056>

Fig. 1

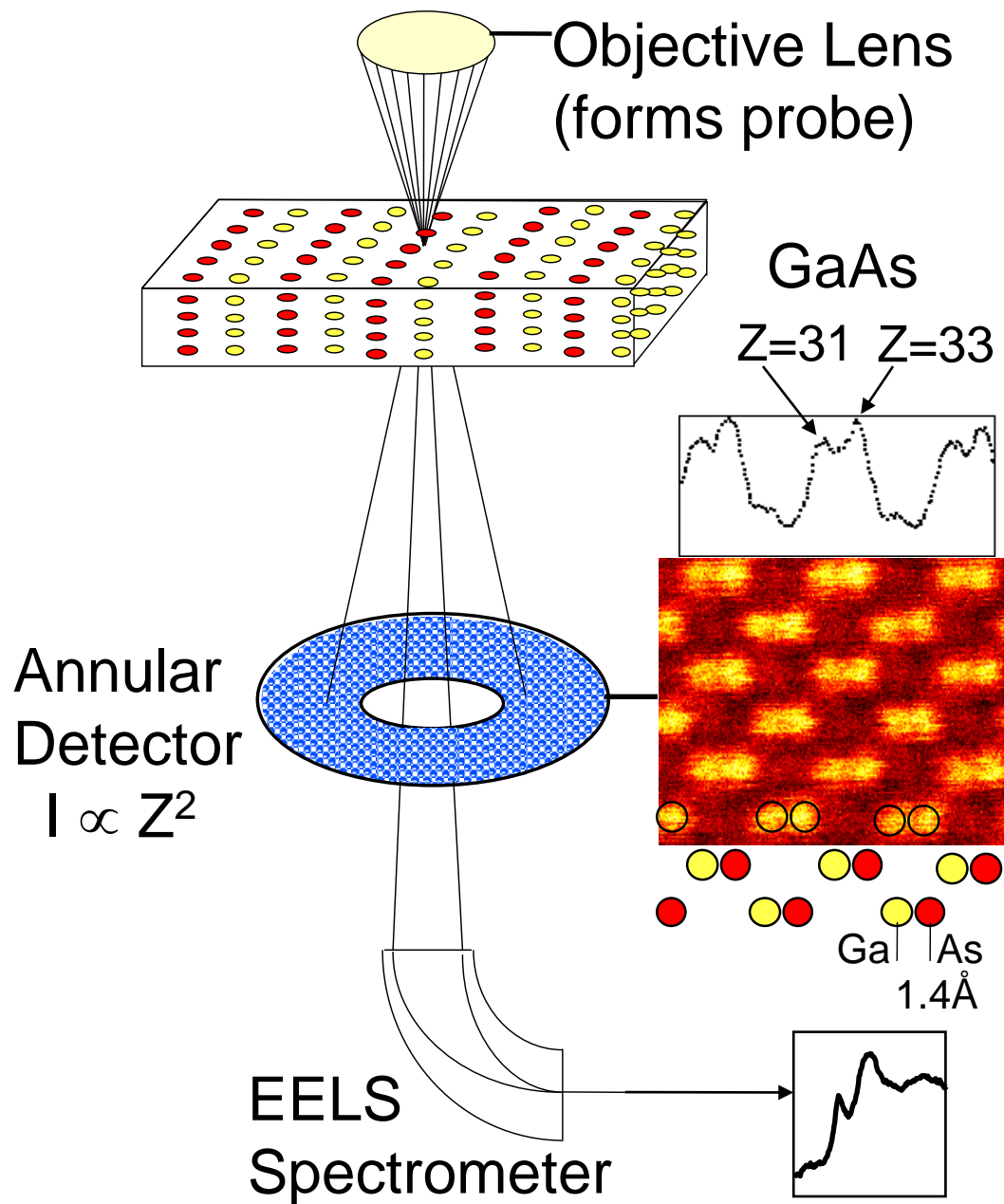
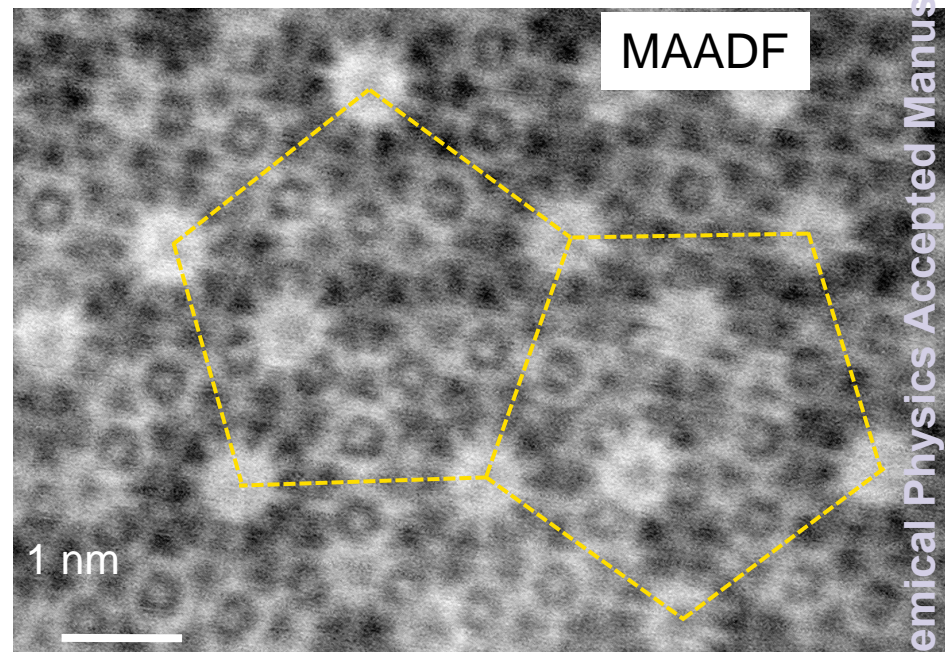
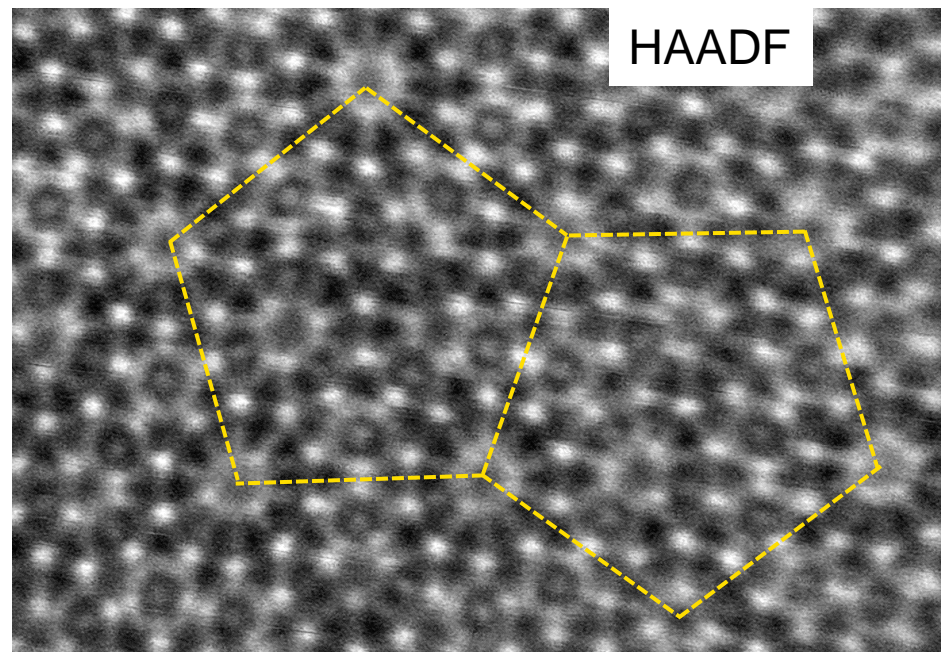
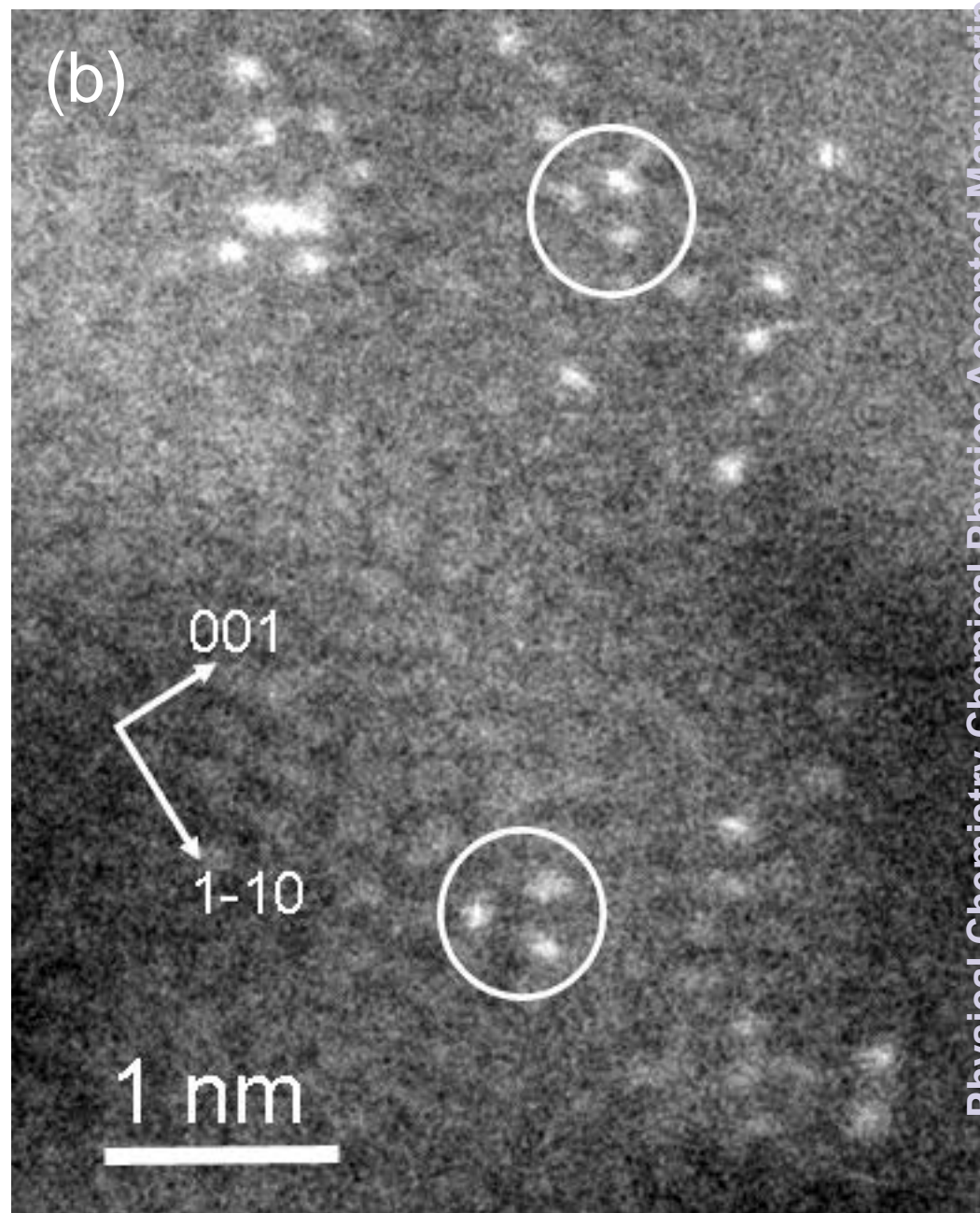
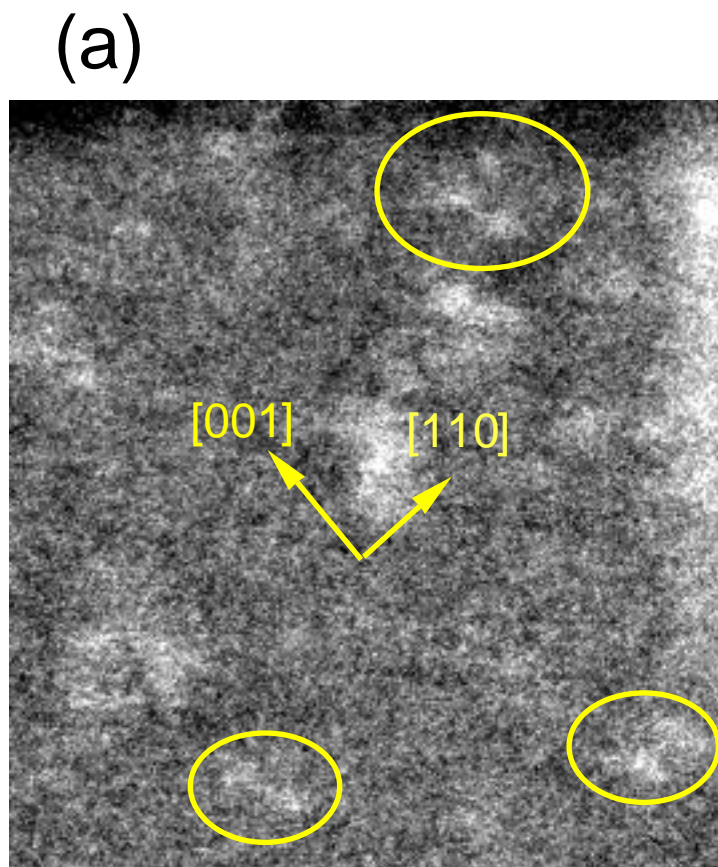


Fig. 2





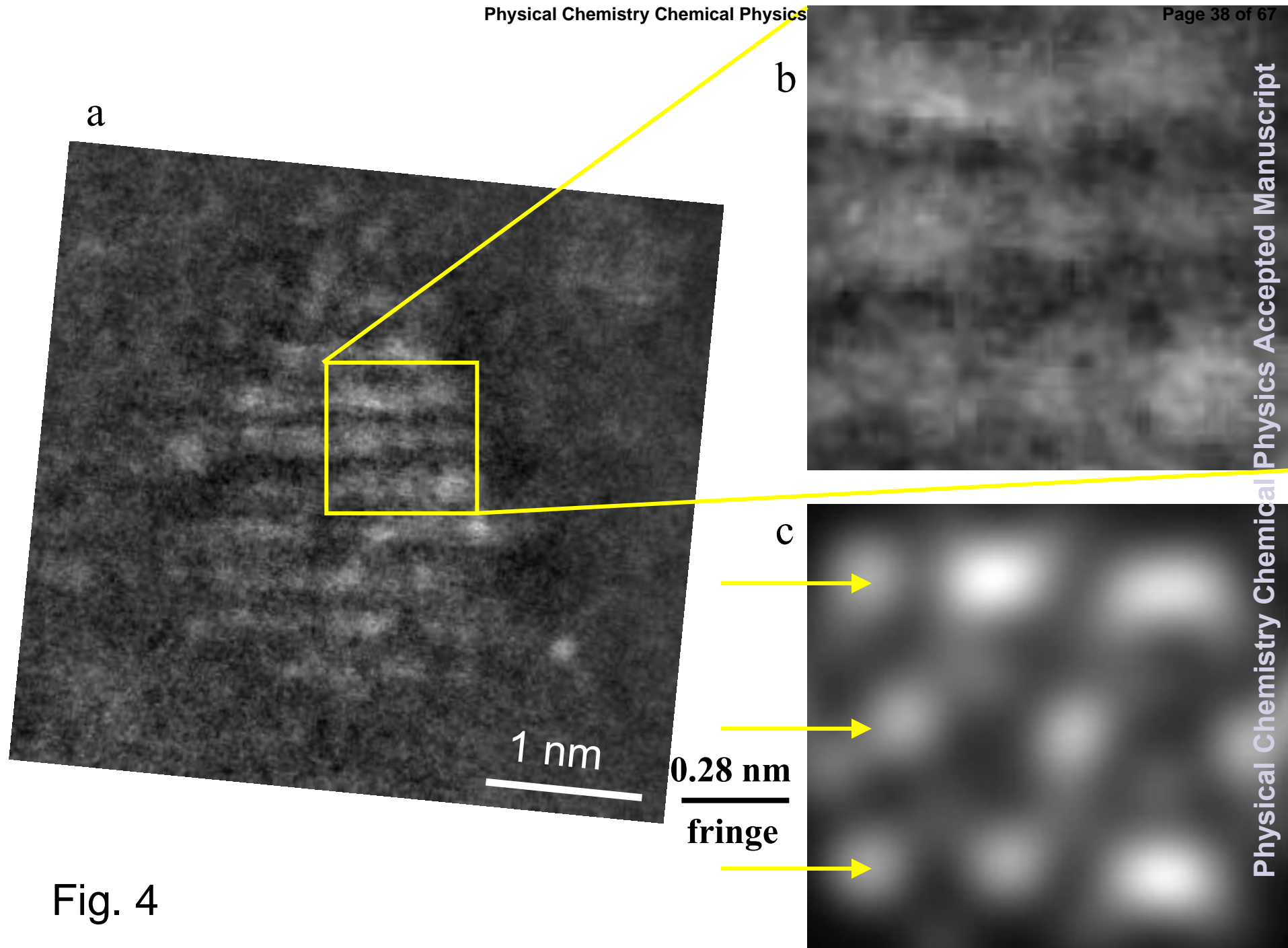
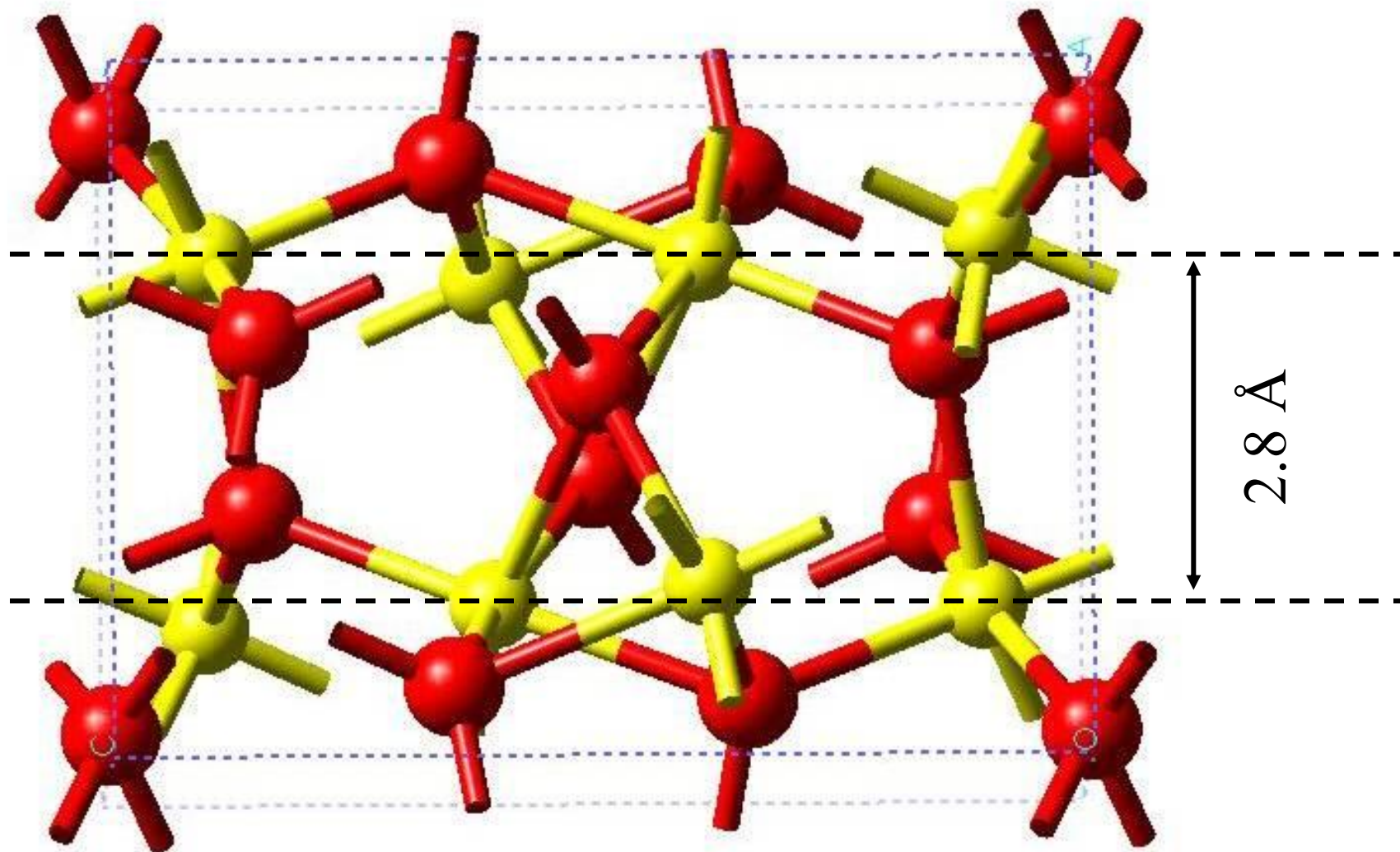
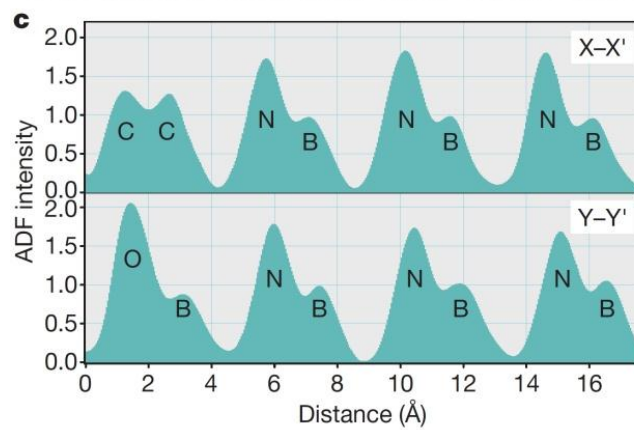
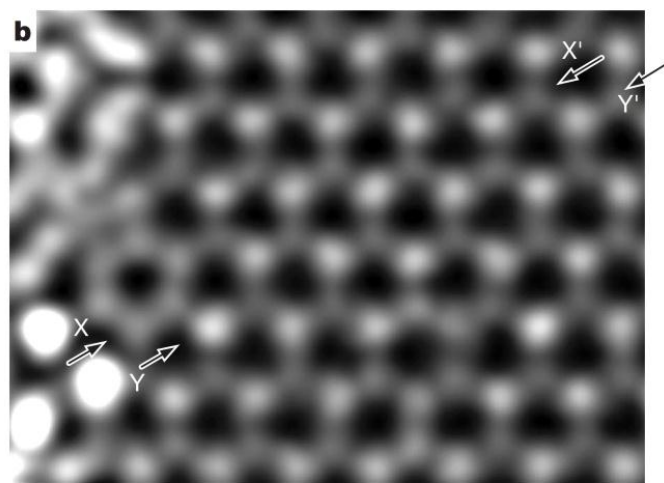
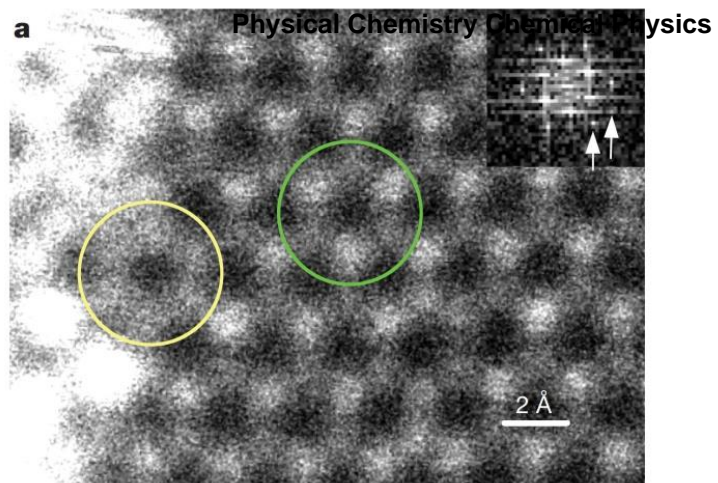
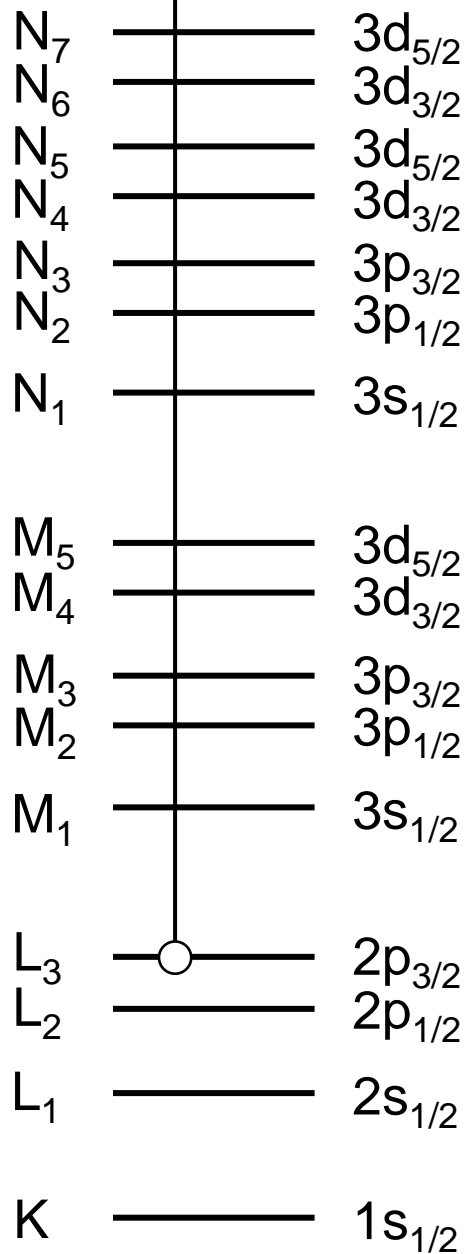


Fig. 4





Shell notation

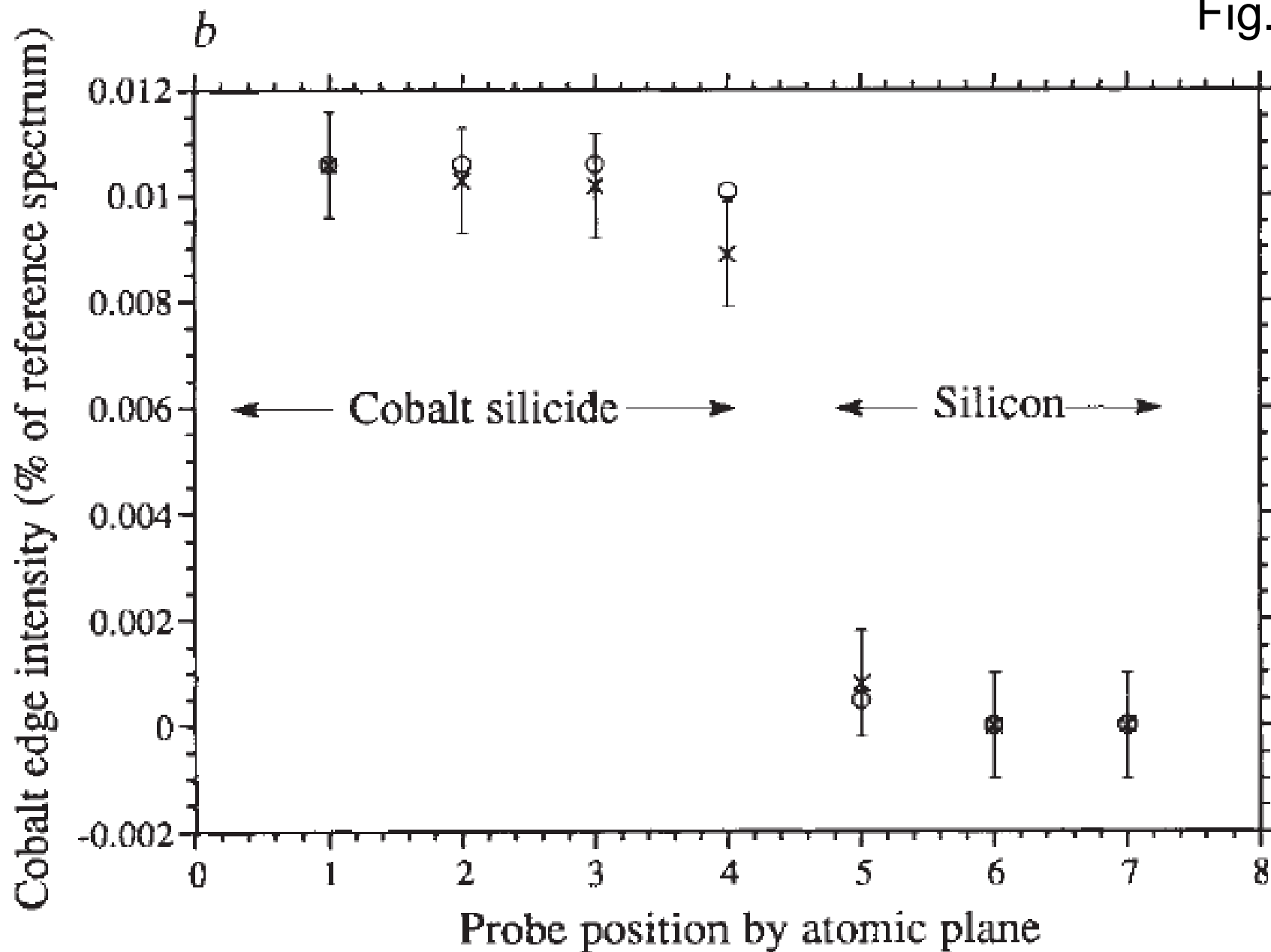


Ionization limit

L<sub>3</sub> edge

Energy loss

Fig. 8



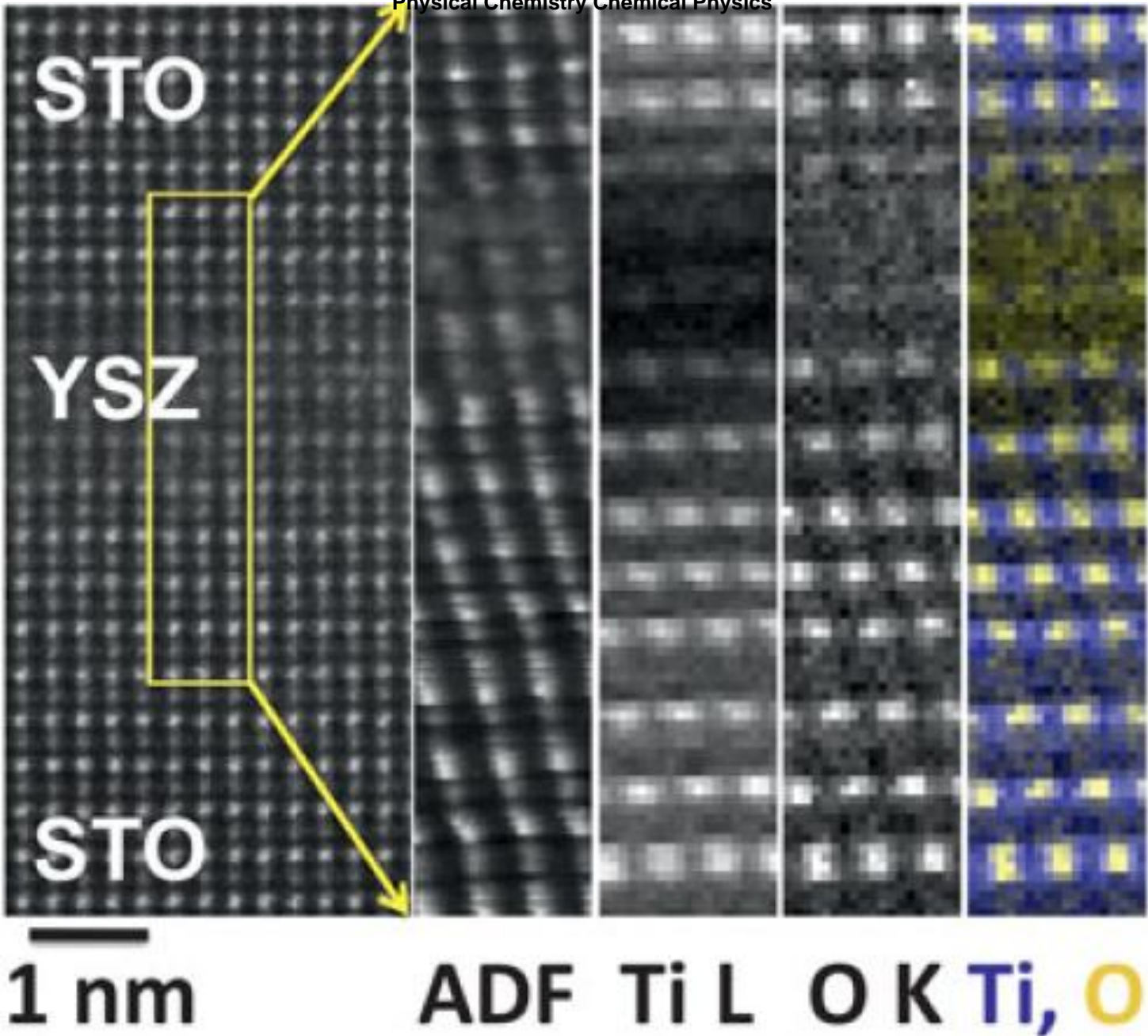
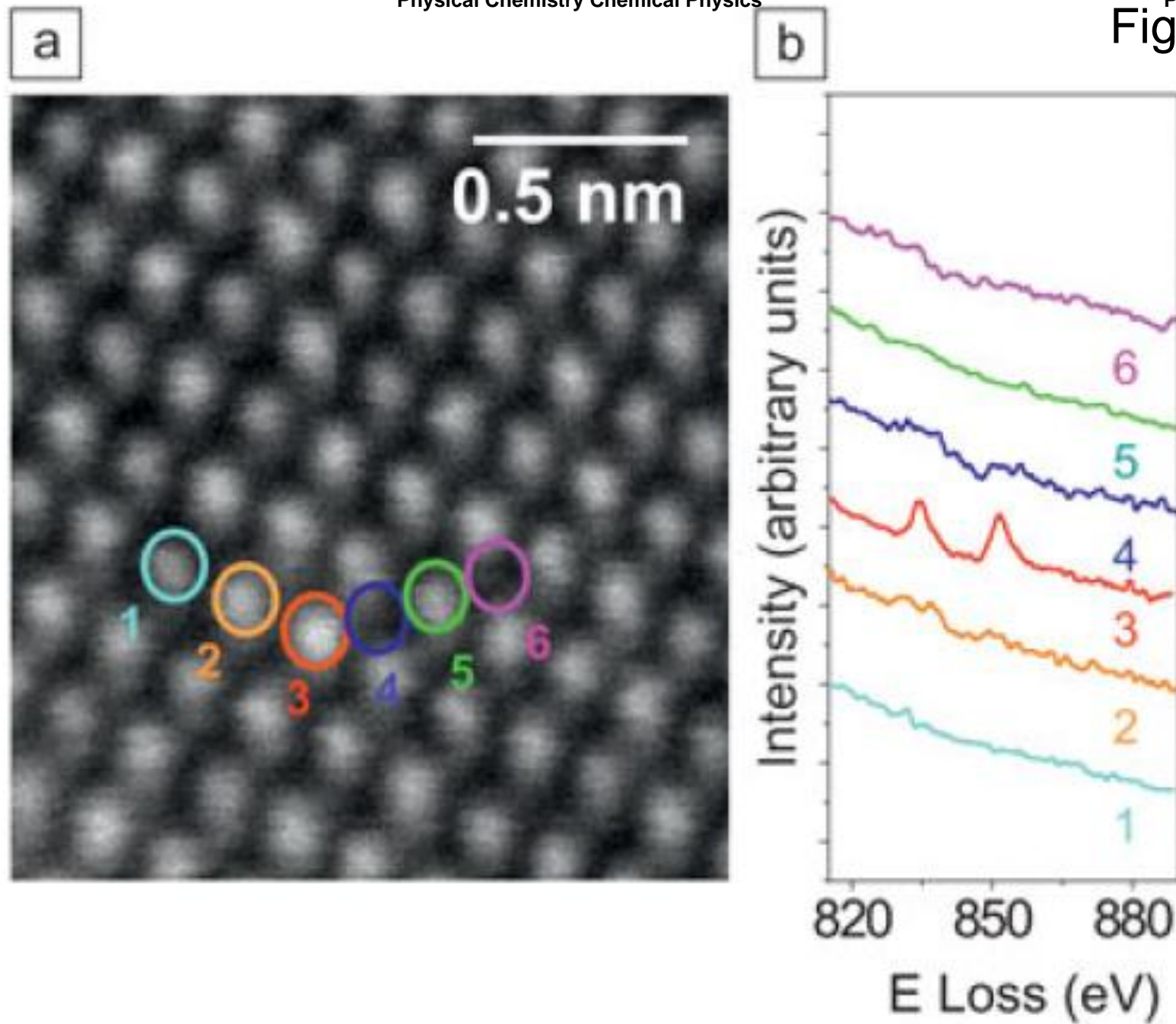


Fig. 9

Fig. 10



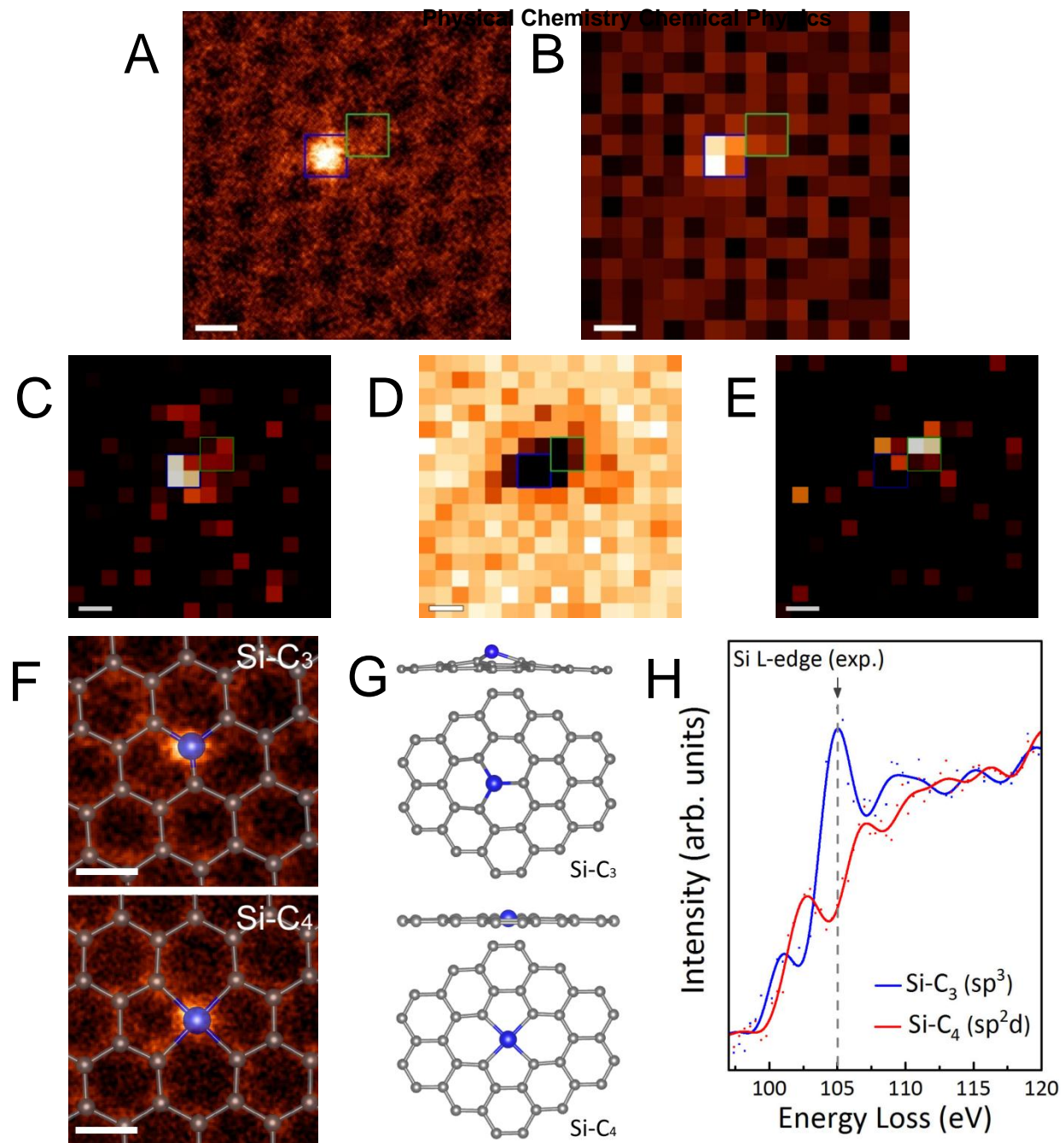
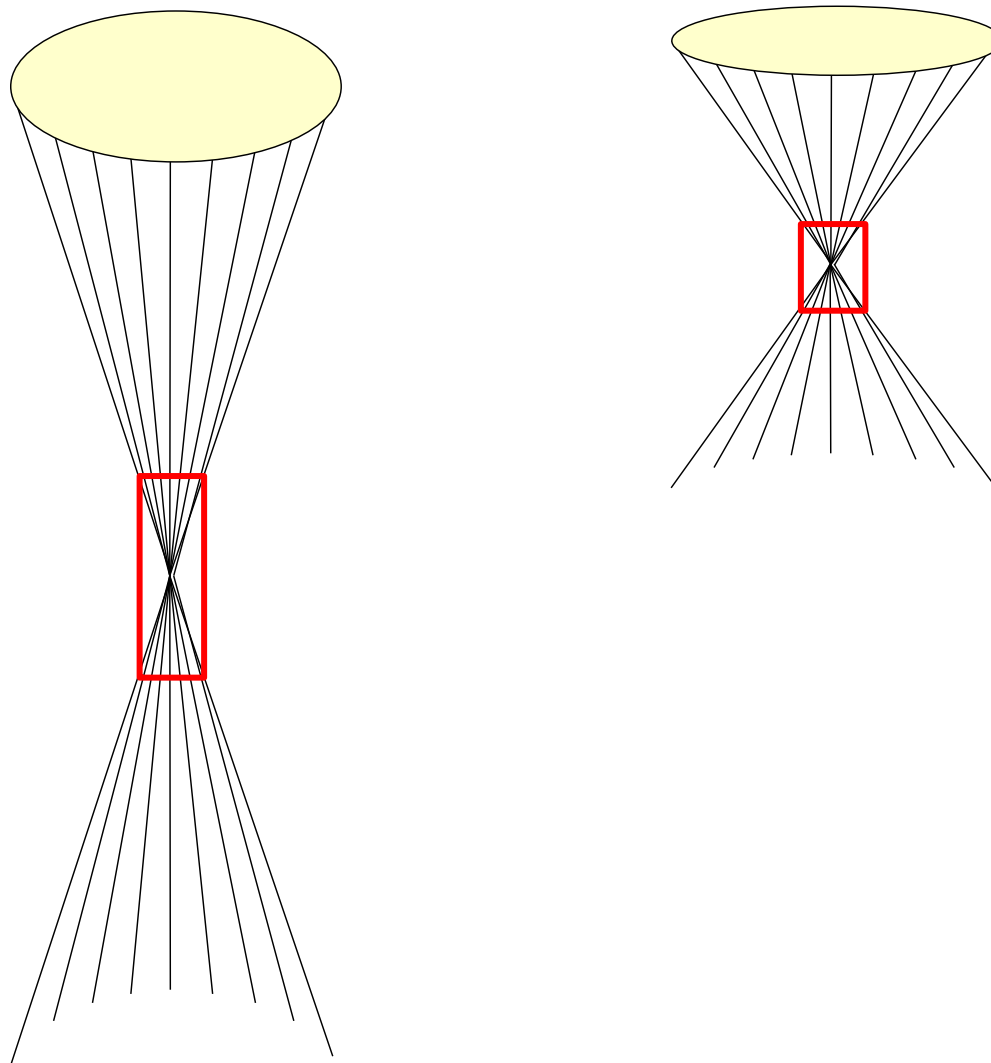
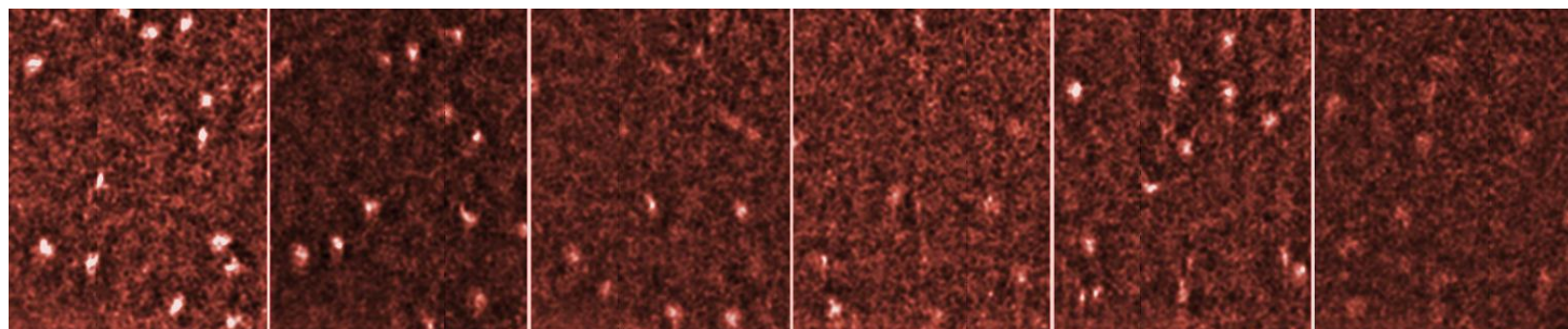
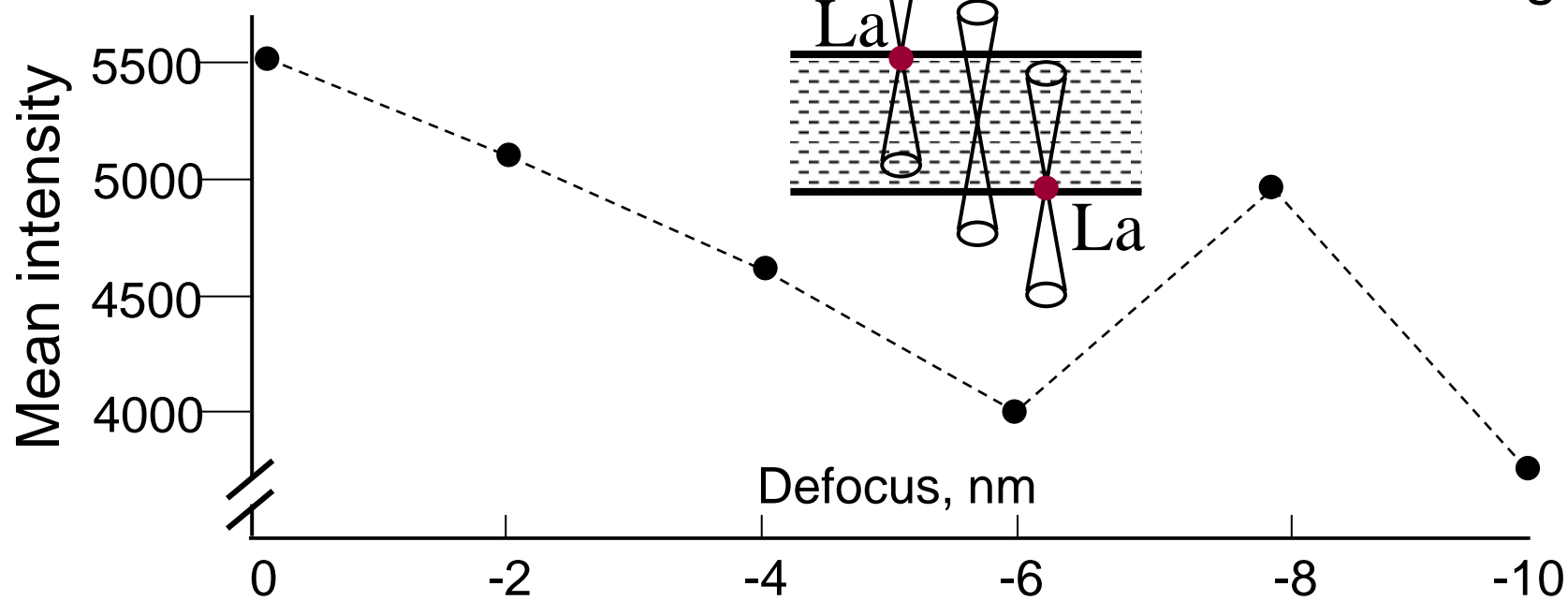


Fig. 11





"top"

"bottom"

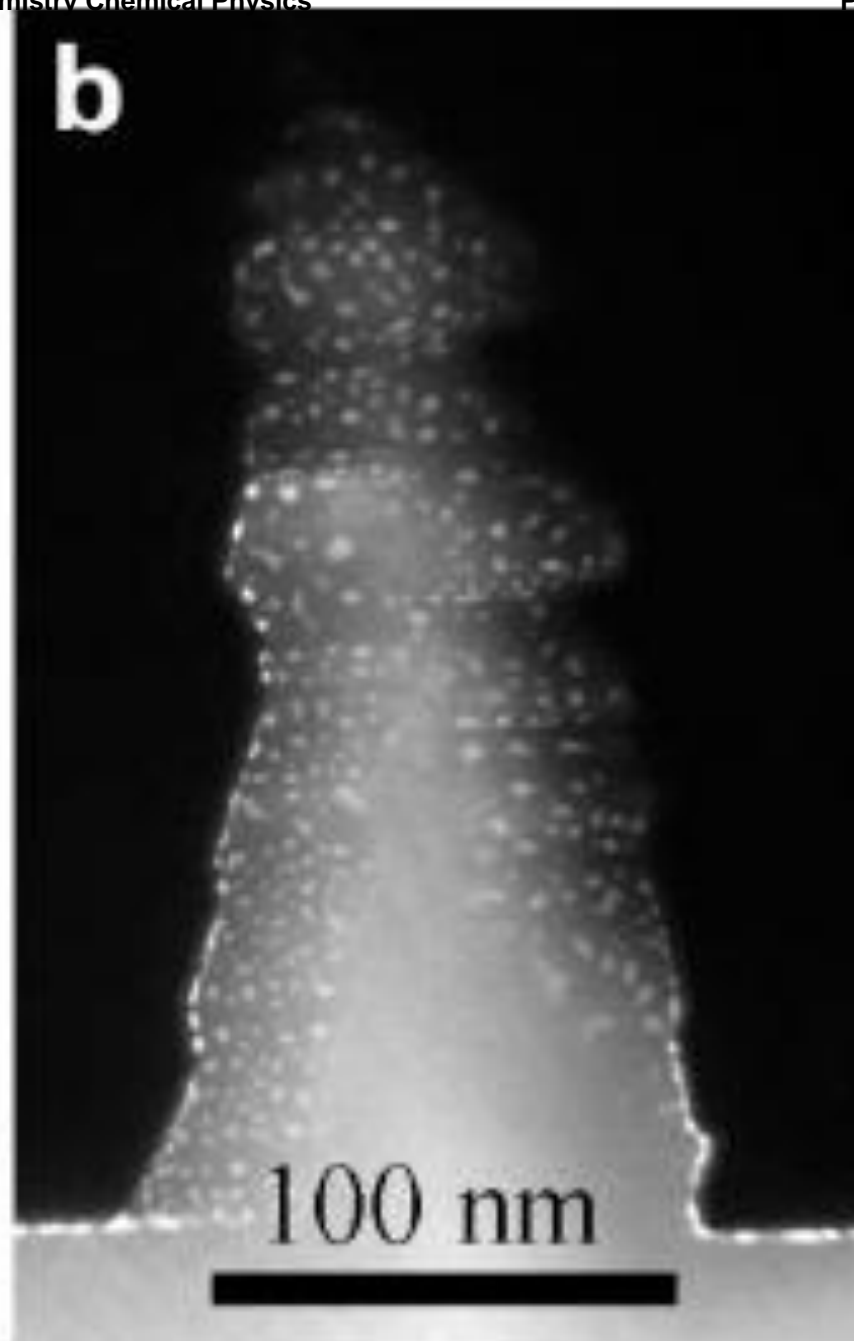
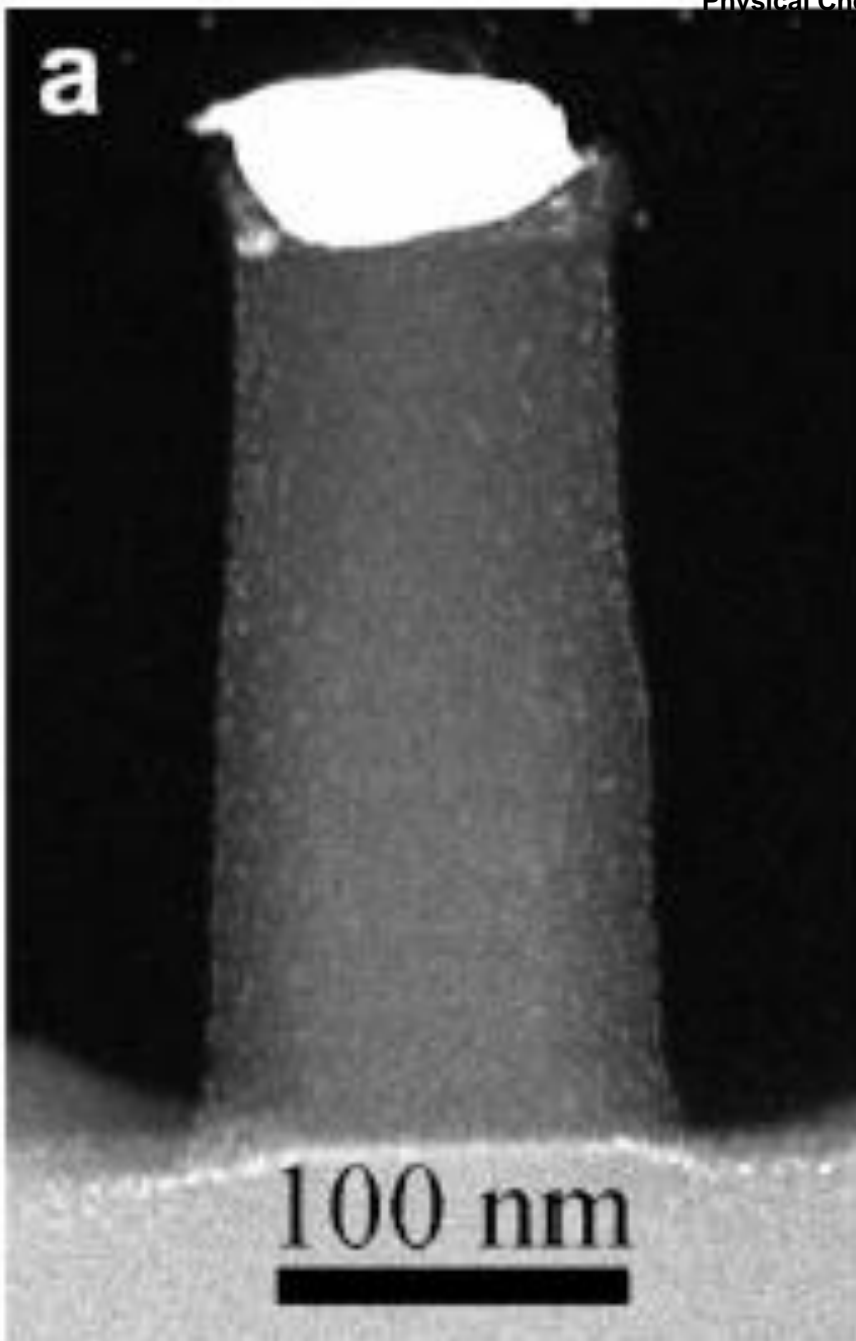


Fig. 15

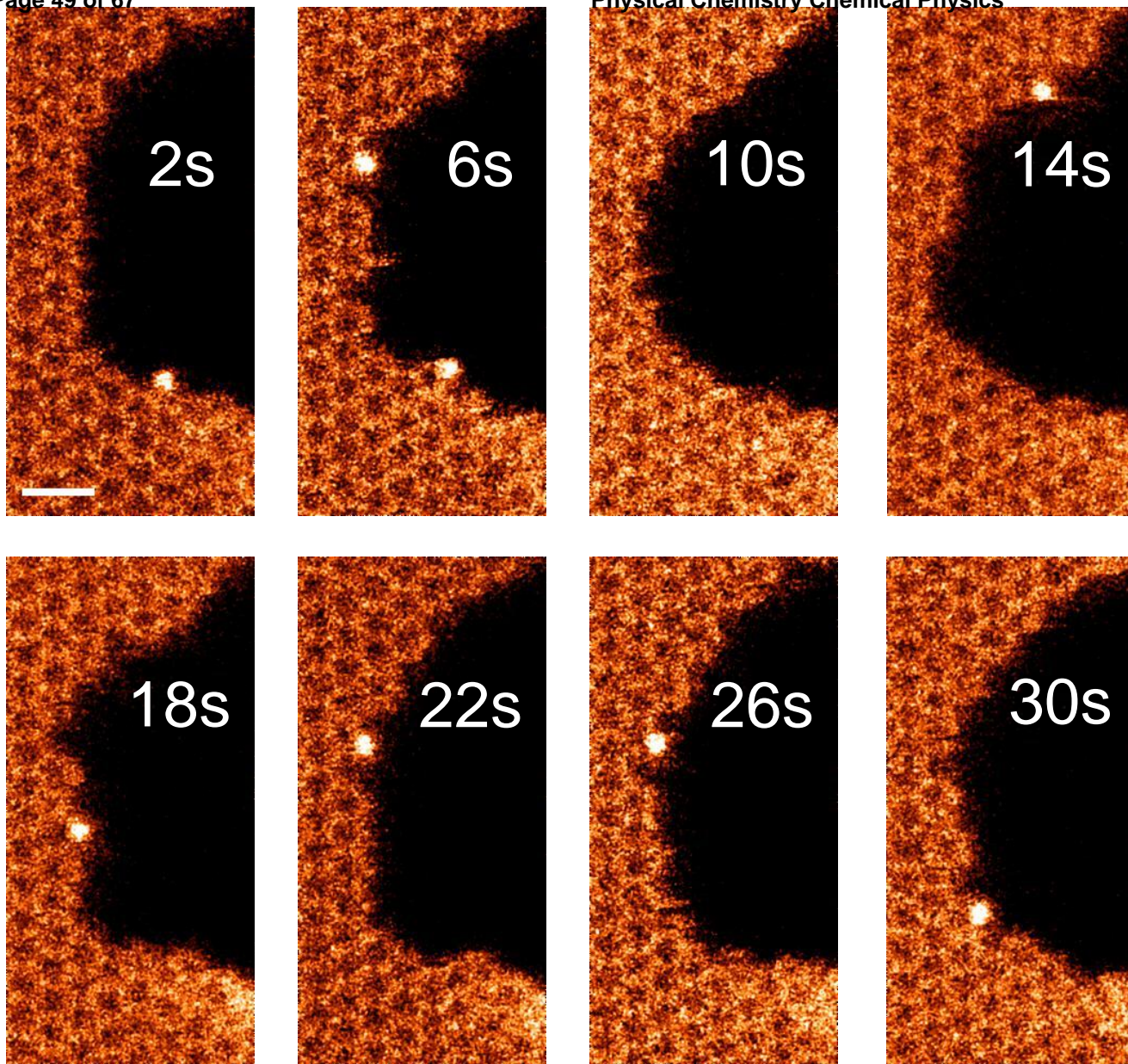
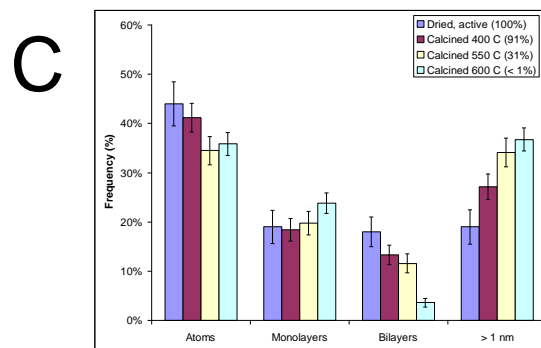
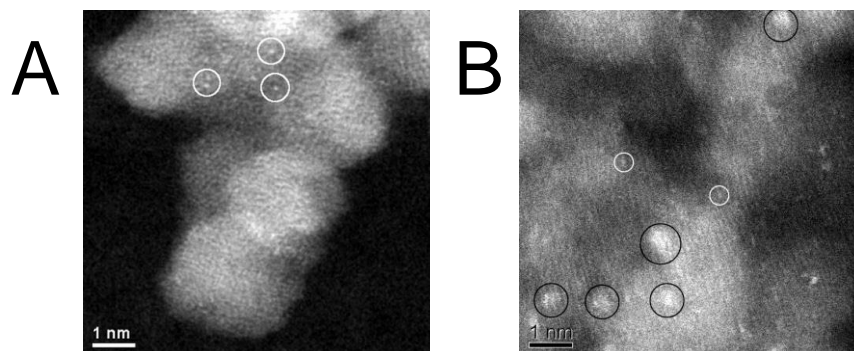


Fig 16



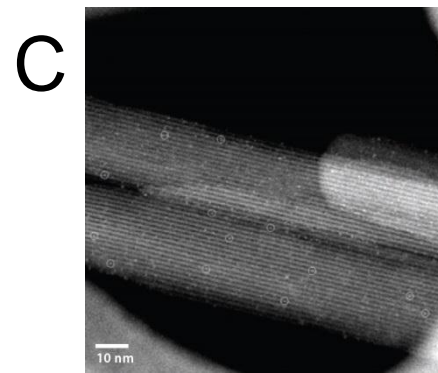
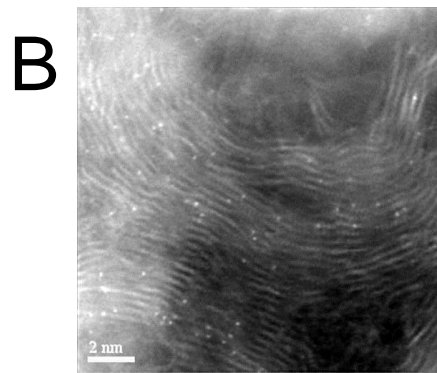
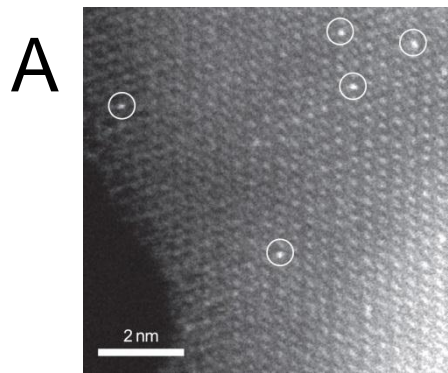
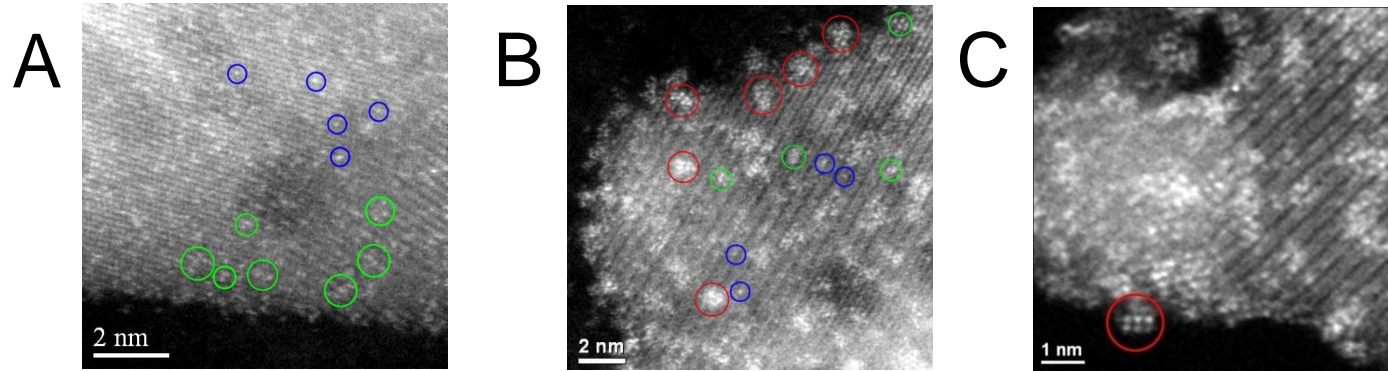


Fig 17

Fig 18



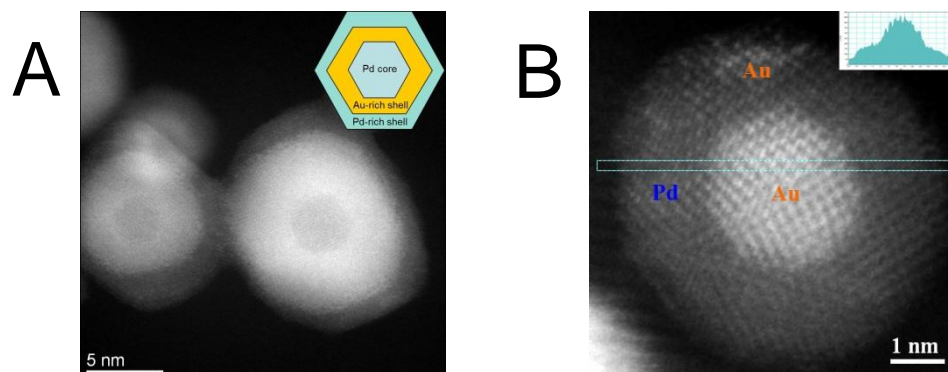
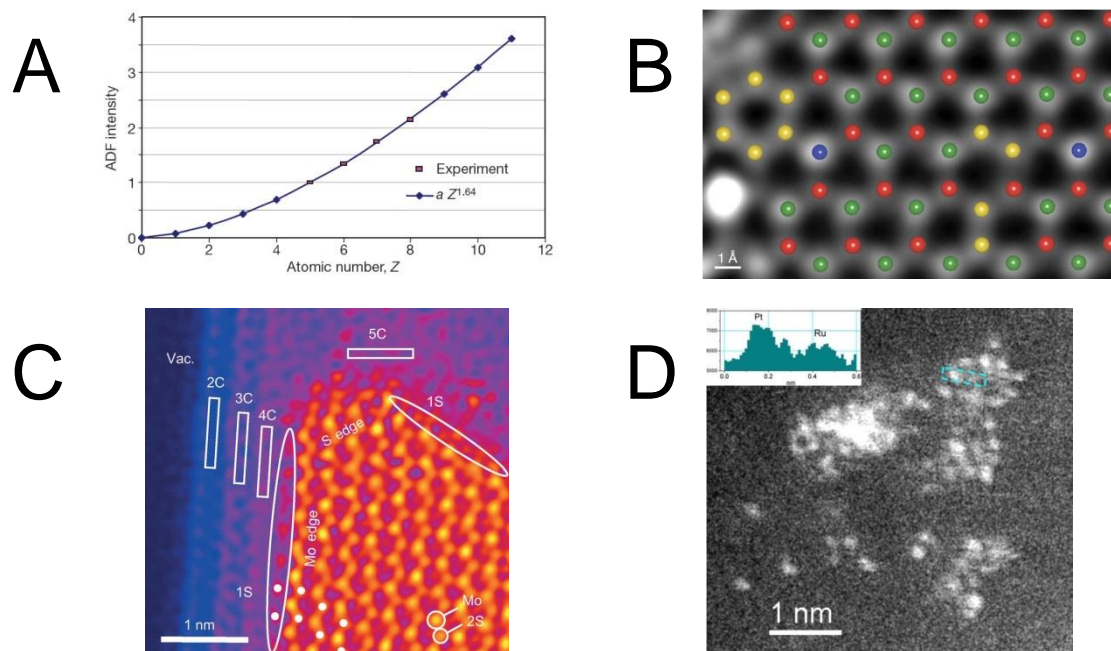


Fig 20



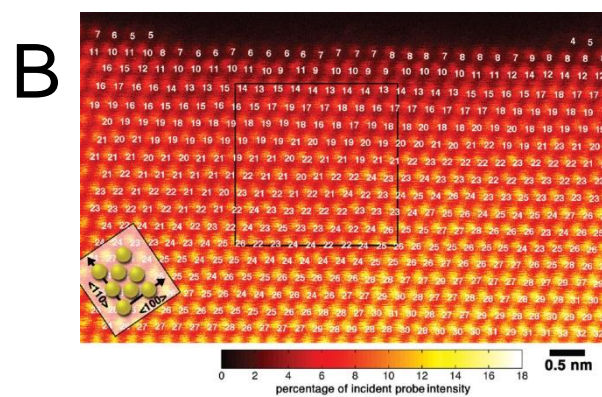
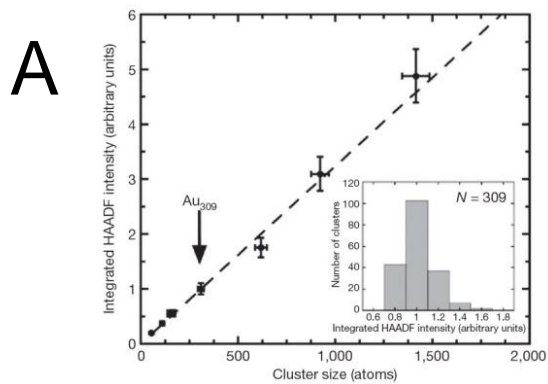
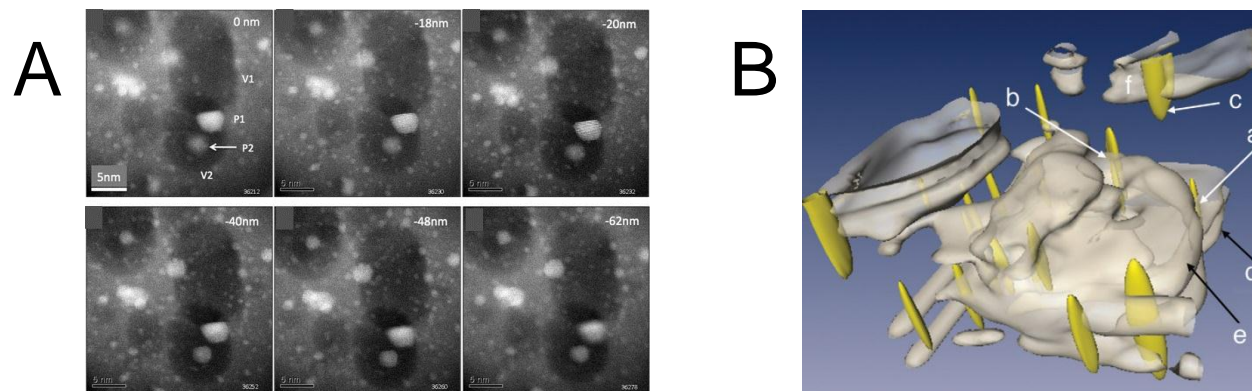


Fig 22



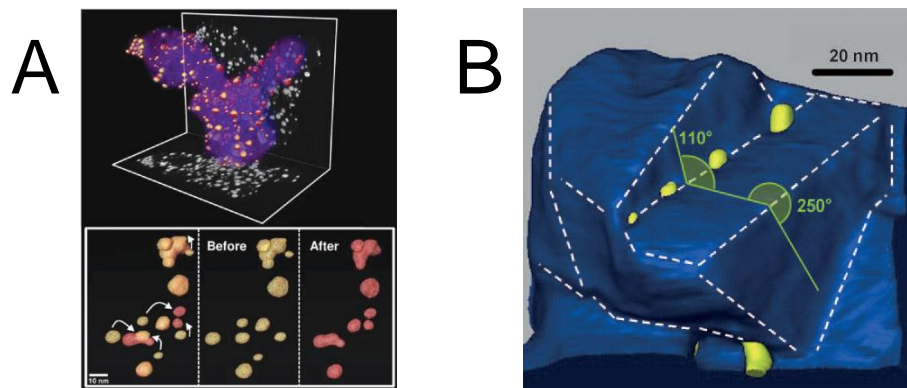


Fig 24

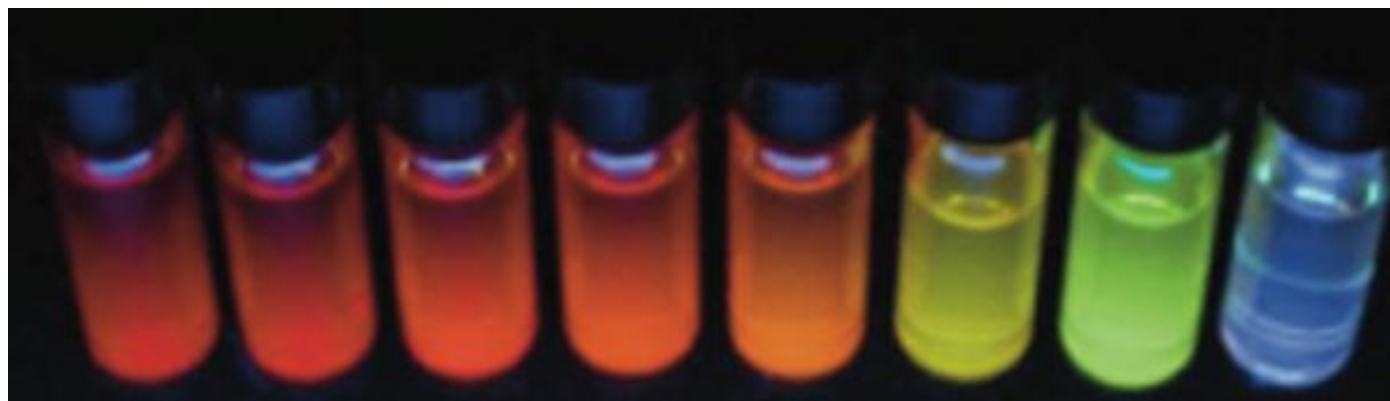


Fig 25

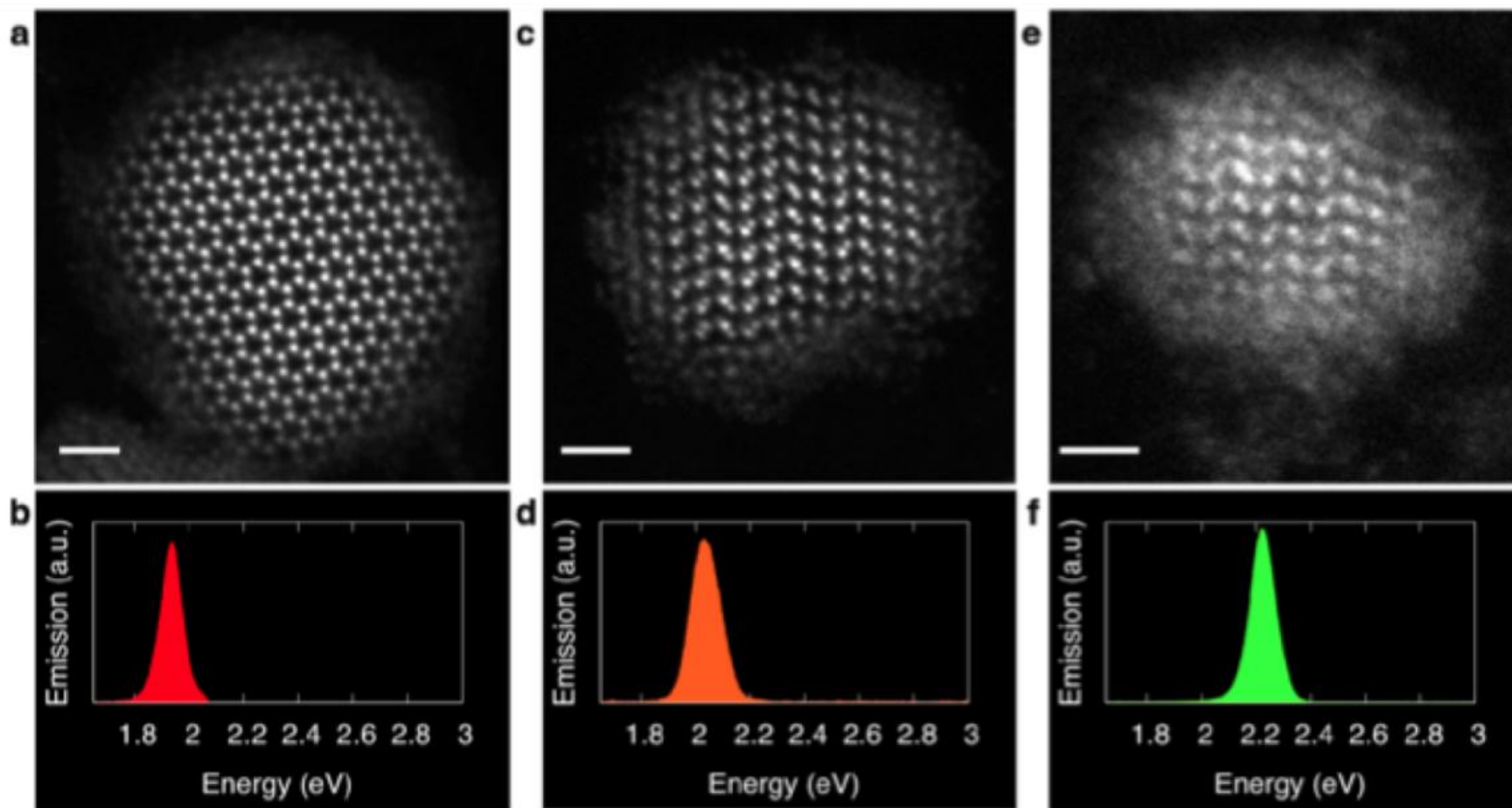


Fig 26

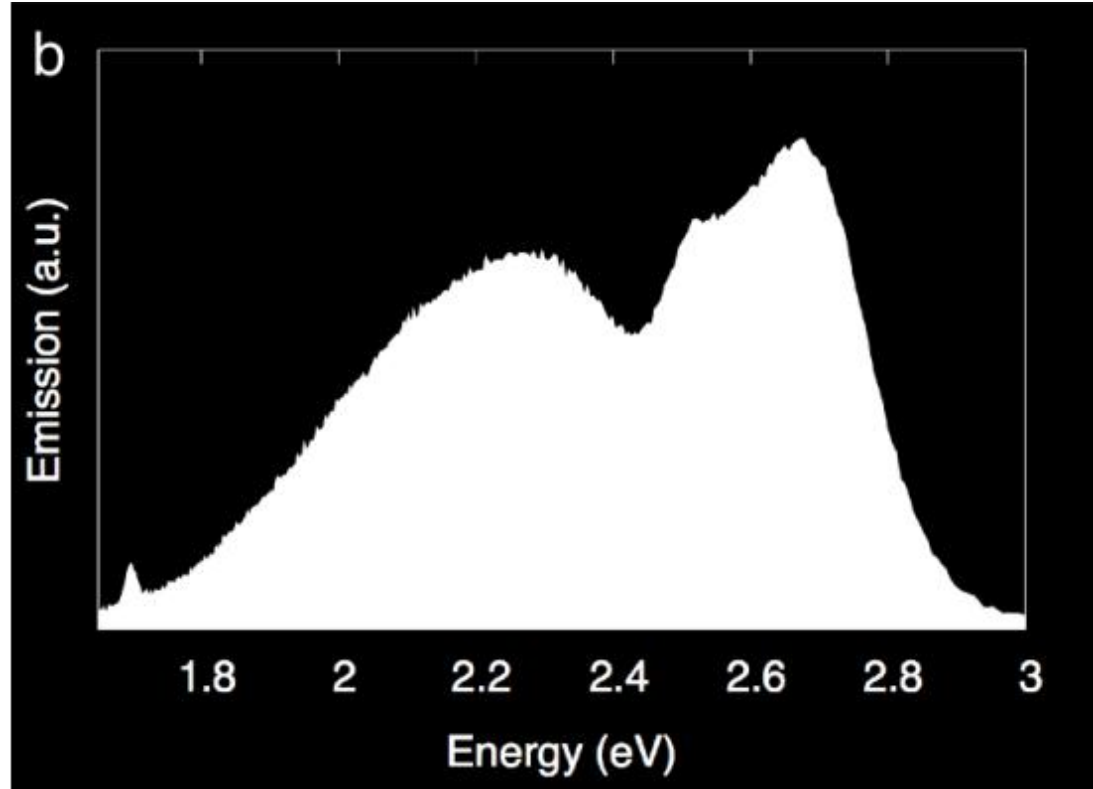


Fig 27

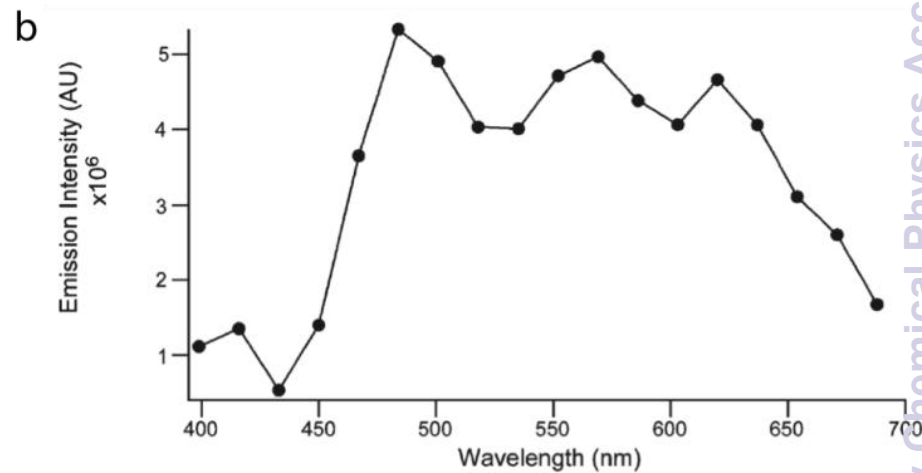
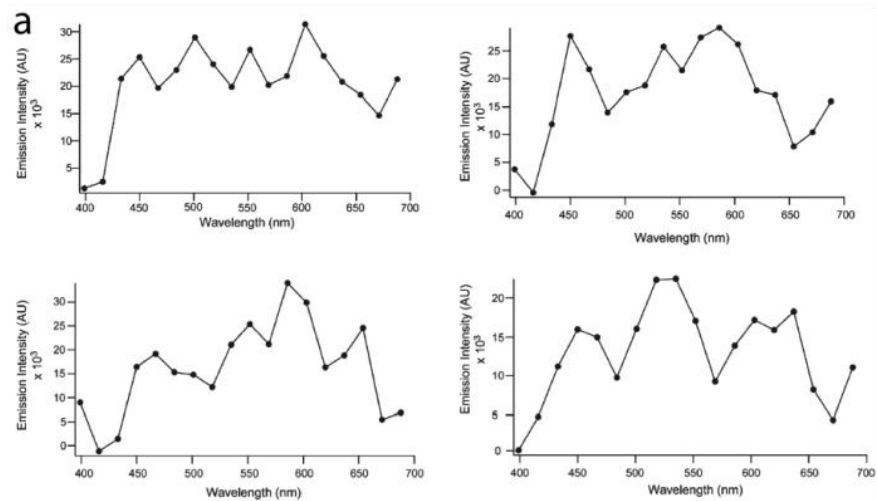


Fig 28

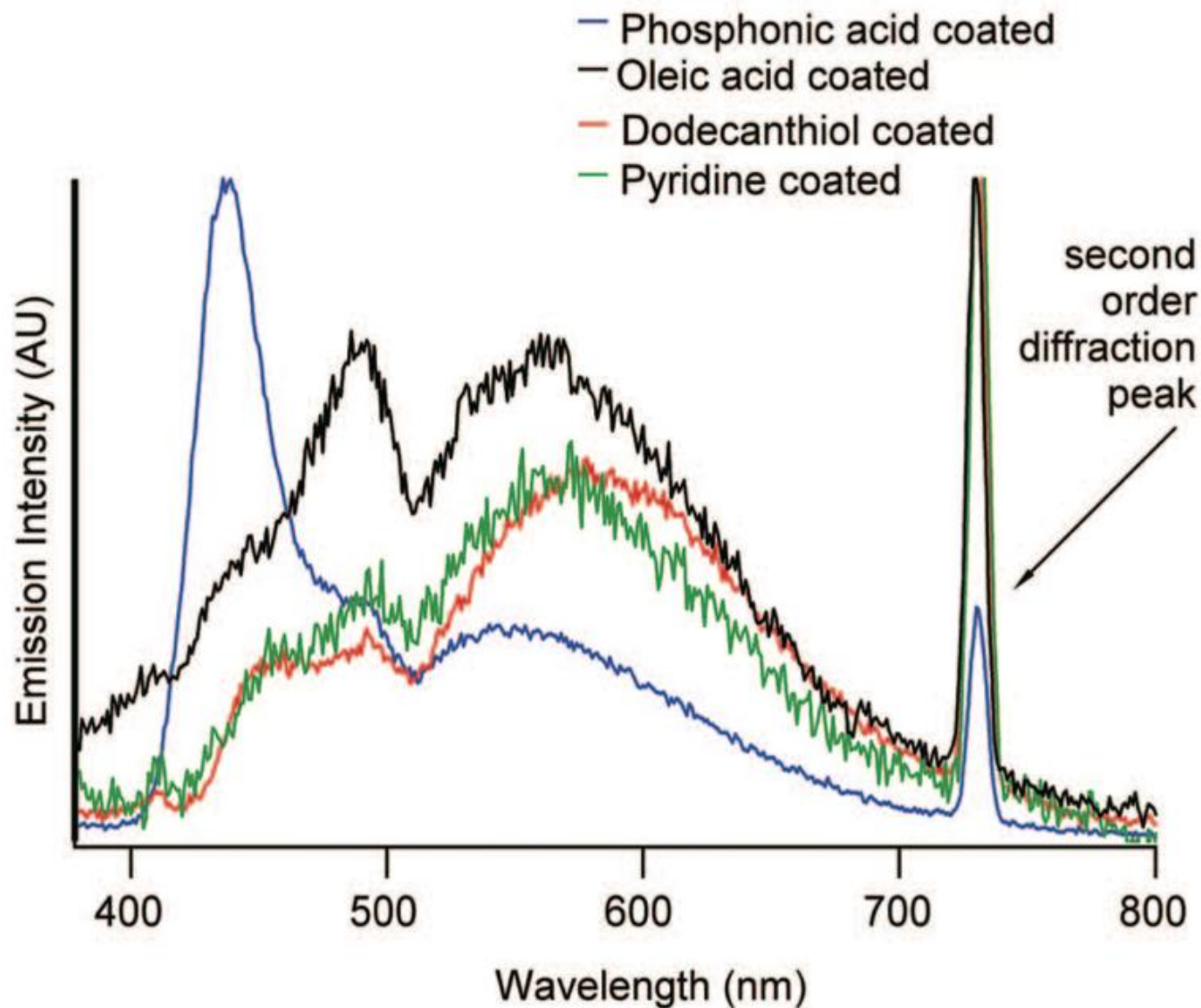


Fig 29

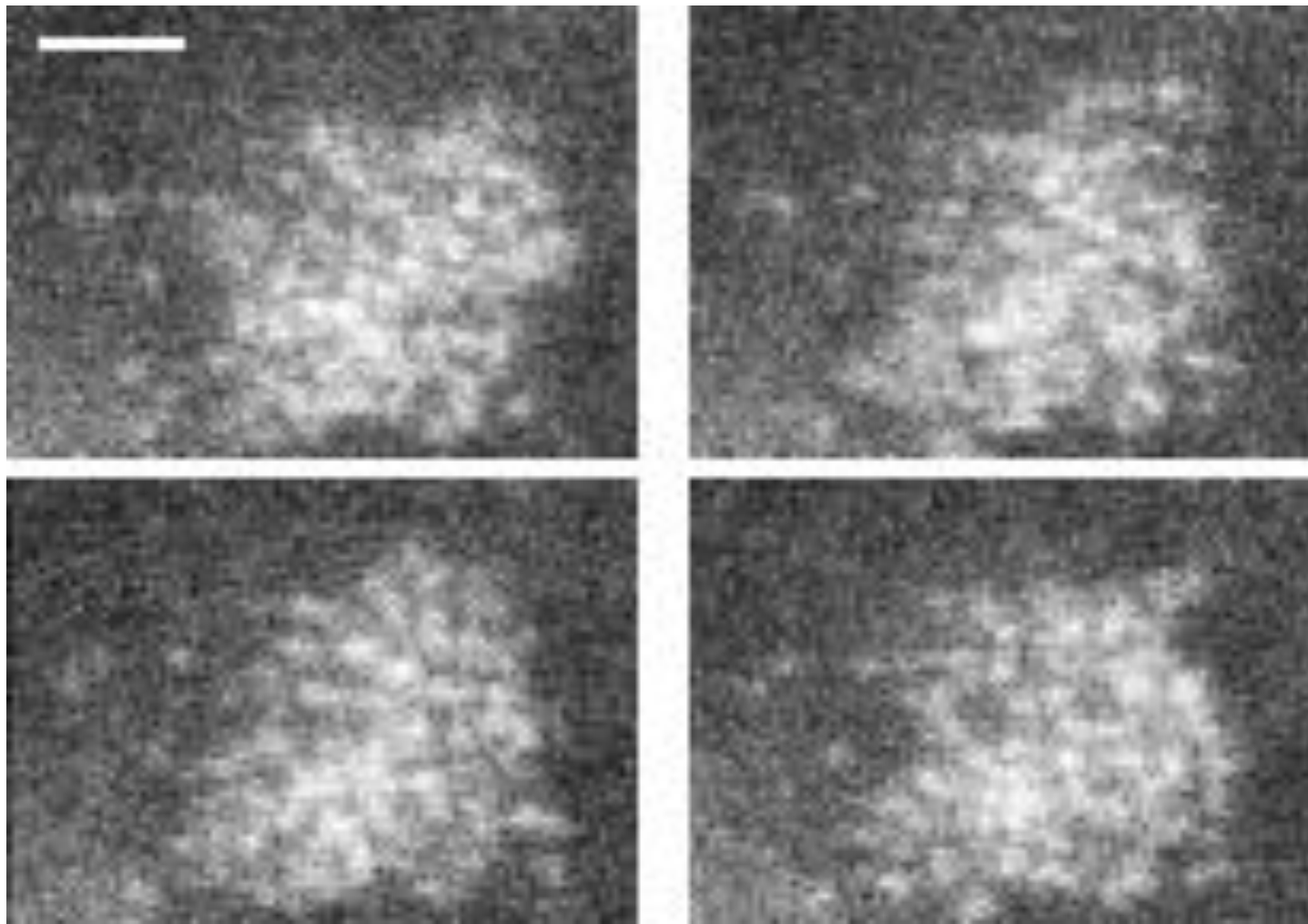


Fig 30

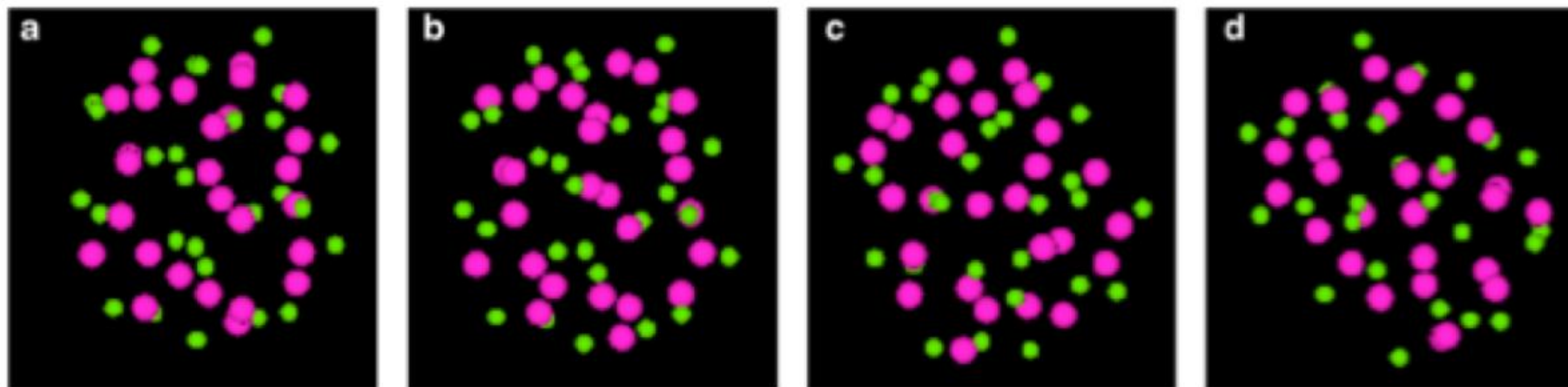


Fig 31

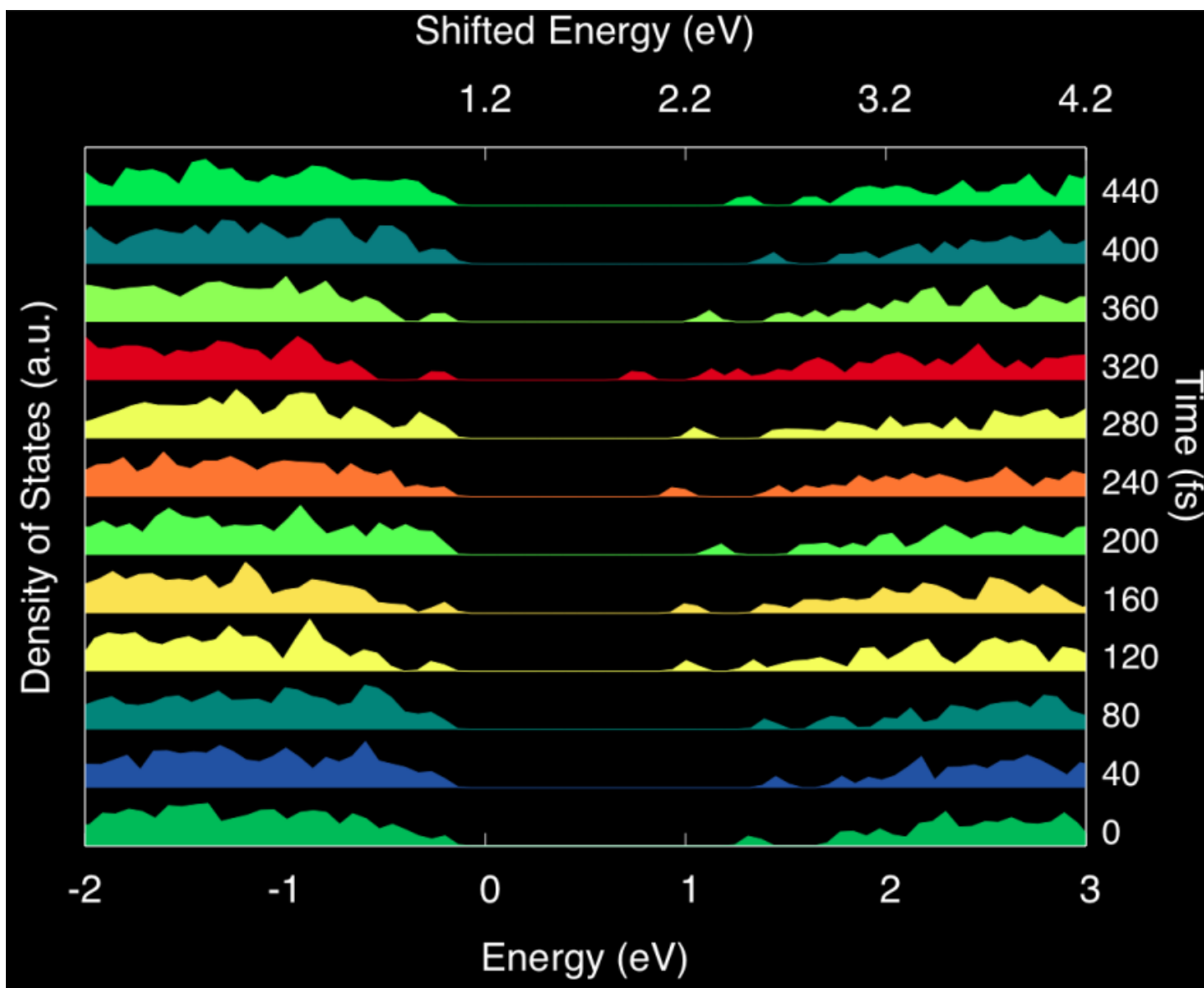


Fig 32

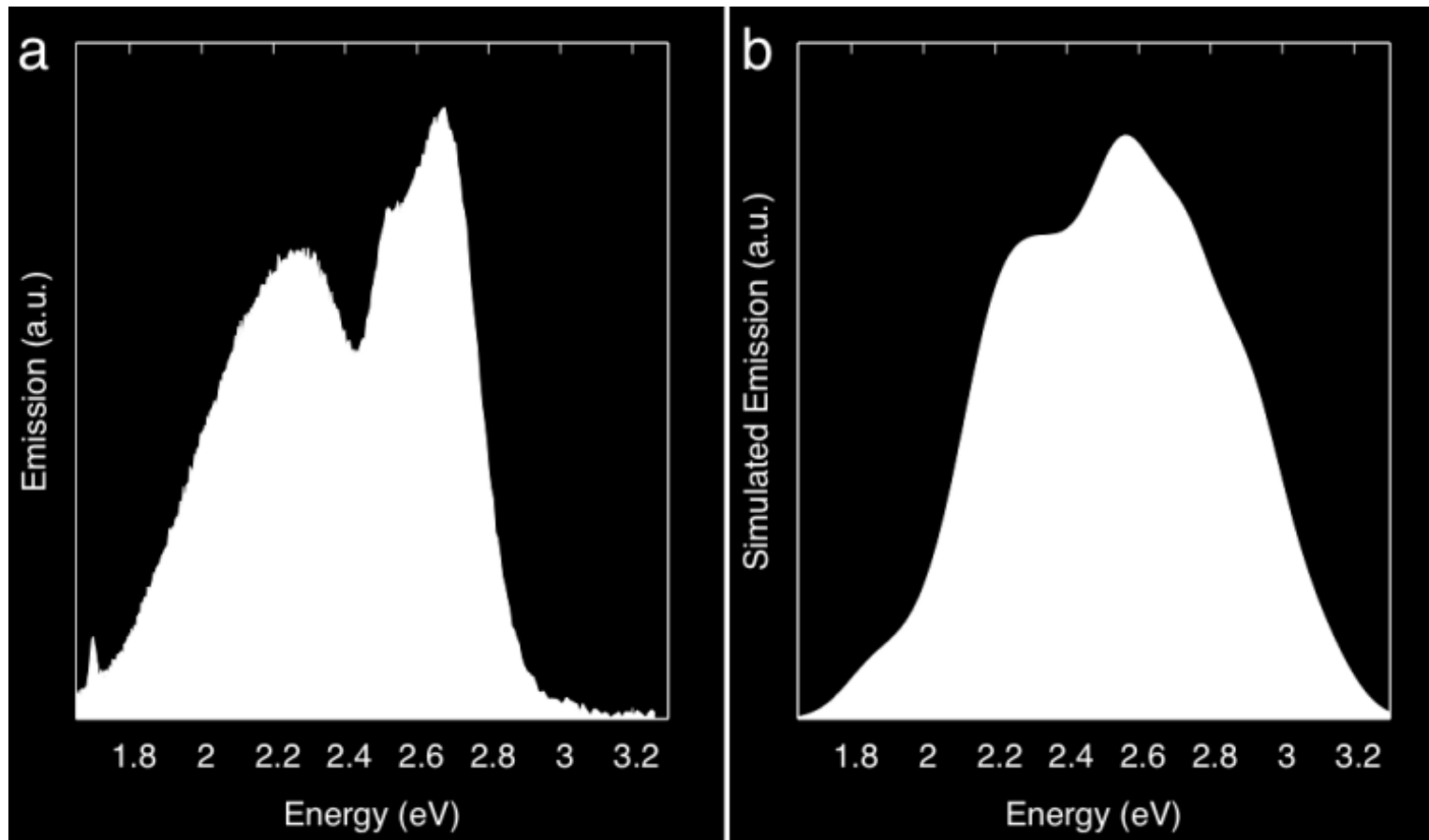


Fig 32

